Diplomarbeit

Structure and Kinematics of NGC 4414

A search for a Supermassive Black Hole

durchgeführt am

Leibniz-Institut für Astrophysik Potsdam

eingereicht an der

Universität Potsdam
Mathematisch-Naturwissenschaftliche Fakultät
Insitut für Physik und Astronomie

von

Sabine Thater

Martikelnummer: 739559
sabine.thater@tufts.edu

Gutachter: Lutz Wisotzki, Philipp Richter
Betreut durch: Davor Krajnović

20.Februar 2015

Contents

Chapter 1

Introduction

The study of supermassive black holes has never met as much attention as over the last couple of decades. Several extensive studies involving the formation and evolution of supermassive black holes and their effect on matter have been conducted. However, due to their extreme nature it took a long time for the existence of black holes to be accepted in the scientific world. The idea of massive bodies being able to influence light crossed John Michell's mind in 1783 already but was mostly ignored then. A first crucial key was contributed by the general theory of relativity. The discovery that gravity influences the light's motion made black holes particularly interesting. However, five more decades passed until the first candidate for 'black holes' was finally discovered. A term used by the Princeton theorist John Wheeler on a conference in 1967[1] While the presence of BHs was still questioned a few decades ago, the SMBH in the center of galaxies has been well-established by scientists now. Today, the question is if all galaxies harbour supermassive black holes in their cores and how are the black holes linked to their host galaxies. Therefore, different properties of host galaxies have been analysed with respect to the black hole mass.

Black holes belong amongst the most fascinating objects in the universe. They are so compact and dense, that not even light can escape their gravitational pull. Consequently, black holes appear dark making it difficult for us to detect them. However, different methods have been developed to infer the presence of black holes through their gravitational interaction with the surrounding matter. The dynamical signature induced from a black hole on the motion of the objects in its vicinity is distinctive. A Keplerian rotation and an increased velocity dispersion of stars and gas within the black hole's sphere of influence provide a strong indication for the presence of a black hole. Numerous black holes have been identified. The goal of this thesis is to analyse the dynamical imprint of the spiral galaxy NGC 4414 and infer not only the presence of a mass concentration in the galaxy's core, but also an estimate of its mass.

1.1 Supermassive Black Holes (SMBH)

1.1.1 Definition of Black Hole

The idea of very massive bodies was already discussed in the 18th century. The british scientist John Michell (1784) mused about massive bodies being able to catch even light, the famous mathematician Pierre-Simon Laplace explained dark bodies in his treatise *Exposition du systeme du Monde*(1796) based on Newtonian physics. Knowing that the escape velocity

[1] In fact Wheeler did not invent the term black hole but just adopted it from a casual mention of a person in the audience.http://www.worldwidewords.org/topicalwords/tw-bla1.htm

of an object changes with mass and radius, one notices easily that with a very small radius the escape velocity can become even larger than the speed-of-light[2].

$$r_{sh} = \frac{2GM_{BH}}{c^2} \approx 10^{-5} \left(\frac{M_{BH}}{10^8\, M_\odot} \right) \text{pc} \tag{1.1}$$

The radial threshold that is able to encapsulate even light, is commonly called Schwarzschild radius or event horizon and is still a simple theoretical approach to quantify the size of black holes (Schneider 2008). Thus, a black hole can be defined as mass concentration with a radius smaller than its Schwarzschild radius. It is a direct conclusion, that -based on photometric measurements - such objects can not be detected by any external observer therefore leading to the term 'Black Hole'.
The idea of 'dark stars' was ignored by a large fraction of the physical society in the nineteenth century, as it was not understood how a massless wave such as light could be influenced by gravity (Thorne 1994). However in 1915, this problem could be tackled with Albert Einstein's development of the general relativity which gave birth to a new era of physics. In the theory of relativity, gravity can distort the space-time continuum which influences the light's motion. Only a few months later, Karl Schwarzschild (1916) derived a solution to the Einstein field equations for the gravitational field of a point mass, a theoretical black hole.

1.1.2 Types of Black Holes

Black holes do not show any individual characteristics except their mass, charge or angular momentum. However, they can be classified based on their size and different histories of evolution.

- Stellar black holes are the final evolutionary state of stars having an initial mass of more than 10 solar masses. After exploding in a supernova at the end of their lifetime, massive stars start to collapse under gravitational force until even atomic nuclei are compressed compactly. Stellar BHs usually have a few 10 times the mass of the sun and are scattered throughout galaxies.

- Intermediate black holes accrue from the collision of stars in double or multiple systems and reach masses of about 1000 solar masses. Scientists believe that these BHs can be found in smaller stellar systems like globular clusters.

- Supermassive black holes (SMBHs) are located in the center of most galaxies, spiral galaxies as well as elliptical galaxies. Generally, they reach their immense size of approximately $10^5 - 10^{10} M_\odot$ by accumulating interstellar gas and dust. When this accreted matter falls into the SMBH, it gets heated and emits light within a bright beam.

- Primoridal black holes have formed in regions of large mass and energy density directly after the Big Bang. The universe was governed by extremely dense conditions which compromised matter into hypothetical BHs. Such BHs could have been microscopic. If they have ever existed, they have presumably been annihilated due to Hawking radiation.

The focus of this thesis will be on the analysis of an expected supermassive black hole in the center of a spiral galaxy, namely NGC 4414.

[2]The relation is only exact for black holes with neither charge nor angular momentum. For general black holes the relation can differ up to a factor of 2.

1.1.3 Structure of BHs

The structure of BHs comprises different regions. The most famous region is the BH's event horizon which defines the BH and was discussed already. The event horizon is a boundary in spacetime which allows for only one direction of passing through. Matter and light are carried inwards, but cannot escape the region inside of the event horizon. The shape of the event horizon is approximately spherical, however for rotating BHs it can deform to an oblate shape (Hawking & Ellis 1973).

Very challenging for theorists is the proposed gravitational singularity in the center of BHs. This is the region which contains all the mass of the black hole. For a non-rotating BH, the singularity is compressed into a single point, for rotating BHs it is smeared out to a ring shape (Carroll 2004). Therefore, the singularity can be thought of as a region of infinite density. Many hypothesis have been proposed about the events occurring inside of BHs, one more advantageous than the other. However, this is beyond the scope of this thesis as we are more interested in the effects of the objects outside of the BH.

In the case of rotating BHs another region called ergosphere exists. The ergosphere is an oblate spheroidal region enveloping the event horzion. As the spacetime itself rotates jointly with the BH, all objects around the BH also move in the direction of rotation. Close to the BH this effect becomes so strong, that an object would have to move faster than light in the opposite direction to just stand still. Thus, no stationary particles can exist within the ergosphere (Carroll 2004). The angular velocity of the co-rotating objects decreases in the outwards direction.
The gravitational effect of the BH on the particles surrounding it retains until the sphere of influence is reached. This will be covered in the following section.

1.1.4 Sphere of Influence

Many people expect a SMBH to have such a large gravitational field that it can influence its entire galaxy. In fact, only a small fraction of the galaxy senses the strong forces of the SMBH. This region is called sphere of influence of the SMBH.
The sphere of influence is a region around the SMBH's center within which the gravitational potential of the SMBH dominates the gravitational potential of the host galaxy. The gravitational influence radius is given by

$$r_{inf} \propto \quad \frac{GM_{BH}}{\sigma^2} \propto \quad 11.2\,\frac{M_{BH}/10^8 M_\odot}{(\sigma/\,200\,\mathrm{km\,s^{-1}})^2}\,\mathrm{pc} \tag{1.2}$$

where G is the gravitational constant, M_{BH} is the mass of the SMBH and σ is the velocity dispersion of the stellar population in the host bulge. (Peebles 1972)
Outside of a few thousand Schwarzschild radii, but still within the sphere of influence, the motion of stars and gas is prevalently driven by Keplerian force reacting on the combined gravitational potential of stars, gas and all the components contributing mass to those regions. The gravitational hold of the SMBH vanishes quickly beyond the sphere of influence (Ferrarese & Ford 2005).
Thus, in order to determine the SMBH's mass dynamically, the gravitational influence zone of the SMBH has to be resolved properly. This sets the minimal requirement on the telescopes of observational campaigns.

1.1.5 Justification of SMBH in center of galaxies

Since the first discovery of the BHs in massive galaxies, many massive dark objects have been found in the center of galaxies. Some scientists even hypothesize SMBHs in the center of every massive galaxy (King 2003). The question arises, 'How do we know that the massive objects are really SMBHs?' Several observational signatures have been proposed to demonstrate SMBH environments.

An unambiguous evidence for a SMBH can only be obtained by verifying two classical BH features: the event horizon and the intrinsic singularity. Both have not been observable yet. However, SMBHs can also be confirmed by indirect signatures of the event horizon or physical processes associated with SMBHs (Ho 1999). For instance, it could be possible to witness the 'advection of matter into the event horizon'[3](Menou et al. 1999). This method is based on advection-dominated accretion flows. When gas falls towards the BH, the gravitational energy is transformed into thermal energy and advected by the flow. Thus, a large amount of energy falls into the central object. In the case that the object possesses an event horizon, the energy cannot be detected anymore as soon as the accretion flow crosses the event horizon. In contrast, if the central massive object has a hard surface, the energy is re-radiated and can potentially be observed. The method of advection-dominated accretion flows was successfully applied to the dark massive object in Sgr A* (Menou et al. 1999, Narayan et al. 1998) and could thus unambiguously proof the central SMBH.

In some AGN and SMBH galaxy candidates spectra a high-energy power-law tail was observed. Titarchuk & Zannias (1998) describe its origin as follows. It is suspected that in SMBHs the strong gravitational potential dominates over the pressure forces close to the horizon resulting into a free fall of the accreting matter. On the other hand, this would not be the case for other dark objects as the pressure would become dominating as soon as their surface is reached. The different cases result in different observational signatures in the dark massive object's spectrum. For details of this effect, I want to refer the reader to the original paper.

Another direct proof of the existence of a SMBH is the measurement of the motion within the vicinity of the SMBH's Schwarzschild radius. Objects within the sphere of influence show a Keplerian rotation due to the existence of a central large mass. This means that stars have larger velocities when they pass closer to the central SMBH. As the galaxies are very distant and the sphere of influence very small, we are unable to resolve single stars and only observe the collective motion. However, close to the SMBH the velocity distribution rises and this means an increase in velocity dispersion towards the center. Thus a rise in velocity dispersion implies relativistic velocities within a few Schwarzschild radii (Ferrarese & Ford 2005). For the closest massive dark objects known the Schwarzschild radius does not extend more than 6×10^{-6} arcseconds (Ho 1999). This is far from the angular resolutions that are achieved today and thus relativistic motion cannot be directly tested yet.

When we depart from nearby quiescent galaxies and look at quasars whose light reaches us from larger distances more arguments for a SMBH can be found (Tremaine 2014). One argument is related to efficiency. The light that is radiated from a quasar is extremely bright. Summed up over the lifetime of the galaxy, the rest-mass energy yields about $10^8\,M_\odot$. The fusion reactions occurring in stars have an efficiency of about 0.3%, thus resulting to a total

[3]Ho 1998, section 6

mass of fuel of $3 \times 10^{10}\, M_{\odot}$ which is close to the total number of stars in our galaxy. However, the efficiency of a SMBH is about 10% and therefore much larger. The required total mass would therefore undermatch $10^{9}\, M_{\odot}$ which is much more convincing for the center of galaxies. Another argument for SMBHs in AGNs is the appearance of powerful jets of plasma. Extraordinary is that jets typically travel close to the speed of light and are very collimated.

A different strategy to confirm SMBHs is to rule out theoretical alternatives for them. One alternative would be a cluster of ordinary stars. However, measurements of colour variation throughout the galaxy show no strong radial gradients for stellar populations. Thus, the increase in M/L ratio towards the center cannot originate from a large accumulation of ordinary stars (Ho 1998).Instead, a cluster of dark stellar remnants like white dwarfs, neutron stars or stellar BHs could still generate the large mass concentration in the center of galaxies. On the other hand, Maoz (1998) annuls the stellar remnant cluster hypothesis by determining a theoretical cluster's lifetime. He concludes that a mass density like in the Milky Way would result in a cluster age much less than the age of the Milky Way.

However, unambiguous evidence of SMBHs in the core of galaxies only exists in a few close cases. Similarly, scientists were also not able yet to prove the non-existence of SMBHs in the center of galaxies. Within the thesis, I have adopted the convention to designate all central massive dark objects as SMBHs. However, the reader should bear in mind that with the current spatial resolution other hypothesizes like the dark-cluster hypothesis cannot be totally excluded yet.

1.2 SMBH-Host Galaxy Co-evolution

Empirical correlations between the masses of the central black holes and various properties of their host galaxies have been found in the last decade. The pool of host galaxy properties includes the velocity dispersion σ (Ferrarese & Merritt 2000, Gebhardt et al. 2000), the bulge stellar mass (Magorrian et al. 1998), the bulge optical luminosity (Kormendy & Richstone 1995, McConnell et al. 2011), total luminosity (Kormendy & Gebhardt 2001, Kormendy et al. 2011) or the Sersic index (Graham et al. 2001), which is related to the galaxy's morphology. Gültekin et al. (2009) and Beifiori et al. (2012) tested numerous correlations between the SMBH masses and host galaxy parameters, but the $M_{BH} - \sigma$ relation appears to be the tightest showing a very low intrinsic scatter.
It is remarkable that the correlations hold for galaxies of different Hubble types and even highly disturbed morphologies like NGC 5128. Also, different environments (from rich clusters to the field) appear to have no effect on the scaling relations (Ferrarese 2002).

The SMBH-host galaxy scaling relations give two major implications. The first one is that if these correlations exist for every galaxy (having a bulge component), then every galaxy (having a bulge) should contain its own central SMBH (Kormendy & Richstone 1995). Secondly, if every galaxy contains a SMBH , then the scaling relations implies some kind of physical coupling between the evolution of SMBHs and their host galaxy bulges.

The SMBH scaling relations are a common instrument to estimate SMBH masses of very distant galaxies which cannot be well spatially resolved. The measured quantity in these galaxies is the velocity dispersion which can be related to the SMBH mass. Thus, SMBH masses in a large number of galaxies could be inferred. It is a simple conclusion, that the derived SMBH masses become more precise with better elaboration of the scaling relations.

Furthermore, the SMBH-host relations assist to compare the SMBH masses derived by different methods.

1.2.1 The $M_{BH} - \sigma$ Correlation

The $M_{BH} - \sigma$ relation is an empirical correlation between the mass of the SMBH at a galaxy's center and the stellar velocity dispersion σ_e of the host galaxy's bulge. Measured in a galaxy, the stellar velocity dispersion tells how the velocity of a group of stars distributed around the mean velocity. Herein, the subscripted 'e' denotes, that the velocity dispersion orientated along the line of sight was measured within the galaxy's effective radius, which contains half the light of the galaxy.

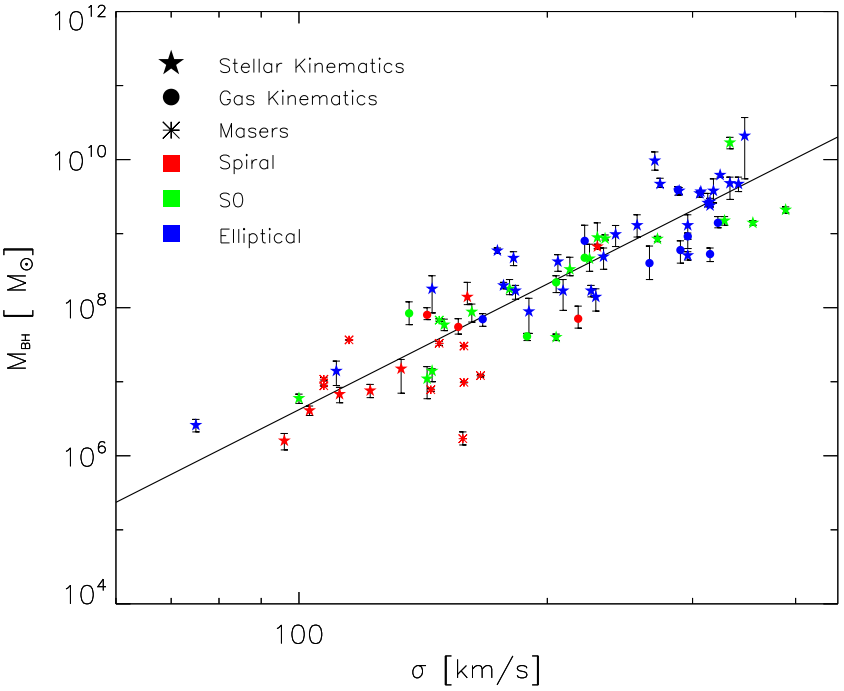

Figure 1.1: *$M_{BH} - \sigma$-relation. The data points are taken from M_{BH} catalogue provided by McConnell & Ma (2013). The symbols show the method of BH mass measurement: stellar dynamics (star), gas dynamics (circles), masers (asterisks). Different colours indicate different Hubble type. The best fit relation is $M_{BH} = 10^{8.12} M_{sun}(\sigma/200 kms^{-1})^{4.24}$.*

The $M_{BH} - \sigma$ relation appears to be the closest SMBH relation as it shows a very tight scatter in the order of '0.30 dex over almost 3 orders of magnitude' (Gebhardt et al. 2000). Interpretations of this tightness suggest a mechanical feedback between the growth of galaxy bulges and the growth of SMBHs. The trend of this relation is commonly described by a double logarithmic linear relationship

$$log(M_{BH}/M_\odot) = a + b \cdot log(\sigma/\sigma_0) \tag{1.3}$$

where the mass of the SMBH is normalized to solar masses, and the velocity dispersion to a value σ_0. σ_0 is often defined to be 220 km/s . The parameters a and b correspond to the zero point and the slope of the fit.

Since the correlation was discovered (Ferrarese & Merritt 2000, Gebhardt et al. 2000), there exists a large discrepancy about the slope and zeropoint of this relation.
The slope of the $M_{BH}-\sigma$ relation has been estimated several times and ranges from 3.75 ± 0.3 (Gebhardt et al. 2000) towards 4.86 ± 0.4 (Ferrarese & Ford 2005). McConnell & Ma (2013) have elaborately studied the relation and provide a table of parameters for different galaxy selections and cuts based on morphologies and velocity dispersions. Various studies and results are listed in table 1.1. For the variance of slopes a number of possible reasons were proposed. It is very likely that different slopes result from systematic differences in velocity dispersion measurements and fitting methods (Tremaine et al. 2002). Also, the selection of SMBHs and host galaxies has an effect on the slope.

The most recent study analysing the $M_{BH}-\sigma$ relation was published by Kormendy and Ho (2013). They use 48 SMBH masses from dynamical methods and get a fit described by

$$\frac{M_{BH}}{10^9 M_\odot} = (0.310^{+0.037}_{-0.033}) \left(\frac{\sigma}{200\,\mathrm{km\,s^{-1}}}\right)^{4.38\pm0.29} \tag{1.4}$$

However, they exclude SMBHs located in disk galaxies and pseudo bulges as well as SMBH masses with unusual behaviour, like large SMBHs in small bulges or in on-going merger processes.

b	Scatter (dex)	Reference	Notes
4.8 ± 0.5	–	Ferrarese & Merritt (2000)	
3.75 ± 0.3	0.3	Gebhardt et al. (2000)	
4.58 ± 0.5	–	Ferrarese (2002)	
4.02 ± 0.3	0.25 – 0.3	Tremaine et al. (2002)	
4.86 ± 0.4	0.34	Ferrarese & Ford (2005)	SMBHs with resolved R_{inf}
4.24 ± 0.4	0.44 ± 0.06	Gültekin et al. (2009)	Different galaxy types
3.96 ± 0.4	0.31 ± 0.06	Gültekin et al. (2009)	Elliptical galaxies
4.38 ± 0.3	0.29 ± 0.02	Kormendy & Ho (2013)	Classical bulges & elliptical galaxies

Table 1.1: *Various measurements of the $M_{BH}-\sigma$ relation. The columns show the slope b of the fit, the intrinsic scatter of the relation, references and additional notes. While the form of the fit differs significantly, the scatter retains low. Adapted from Becerra (2013).*

1.2.2 The $M_{BH}-L_{bulge}$ and $M_{BH}-M_{bulge}$ Correlations

The $M_{BH}-L_{bulge}$ relation was the first SMBH-host galaxy relation to be found. In Kormendy & Richstone (1995) the authors realized that a number of measured SMBH masses seemed to show a direct correlation with the host galaxy bulge luminosities. However, the rms scatter was found to be around 0.5 dex and therefore larger than from the $M_{BH}-\sigma$ relation which was not known then. Kormendy & Ho (2013) also provide an analysis of the $M_{BH}-L_{bulge}$ relation including only classical bulges and ellipticals. Their best fit is given by

$$\frac{M_{BH}}{10^9 M_\odot} = (0.544^{+0.067}_{-0.059} \left(\frac{L_{K,bulge}}{10^{11} L_{K,\odot}}\right)^{1.22\pm0.08} \tag{1.5}$$

Differing from previous studies, Kormendy & Ho use luminosities in the K band which suffer less from extinction and therefore provide a better estimation for the intrinsic luminosity of the host galaxy. The $M_{BH}-L_{bulge}$ correlation is shown in figure 1.2 based on the

SMBH catalogue by McConnell & Ma (2013) [4].

The $M_{BH} - M_{bulge}$ relation was first proposed by Marconi & Hunt (2003). Based on a galaxy sample with gas kinematical and stellar dynamical SMBH mass determination the authors followed a direct relation between the SMBH mass and the mass of the host galaxy bulge. An updated fit by Kormendy & Ho is given by

$$M_{BH}10^9 M_\odot = 0.49^{+0.06}_{-0.05} \left(\frac{M_{bulge}}{10^{11} M_\odot} \right)^{1.17 \pm 0.08} \tag{1.6}$$

having a similar rms scatter as the previous scaling relations.

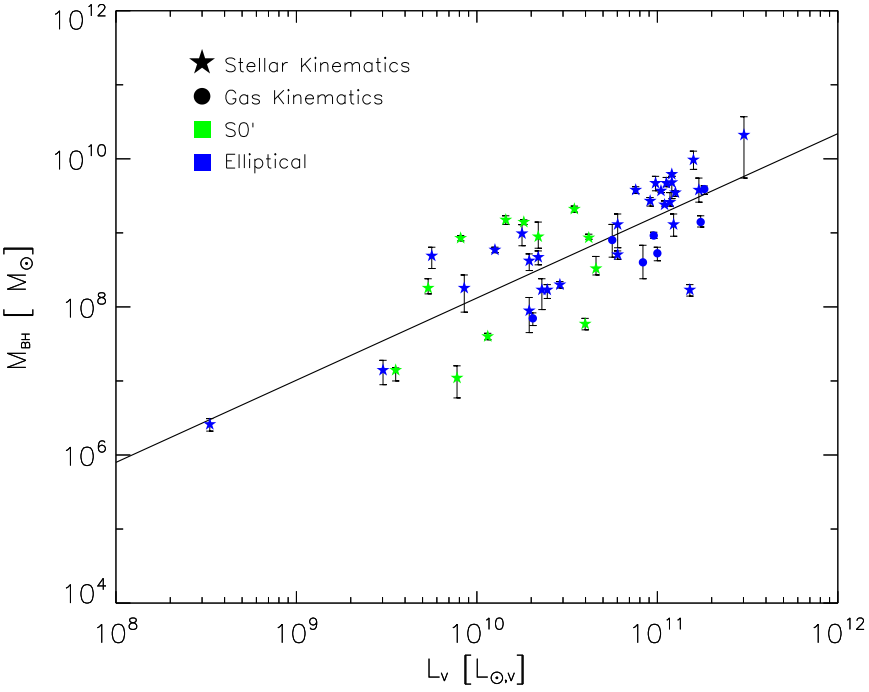

Figure 1.2: *M_{BH}-bulge luminosity relation. The data points are taken from M_{BH} catalogue provided by McConnell & Ma (2013). The symbols show the method of BH mass measurement: stellar dynamics (star), gas dynamics (circles). Different colours indicate different Hubble type. The best fit relation is $M_{BH} = 10^{8.12} M_{sun} (\sigma / 200 kms^{-1})^{4.24}$.*

1.2.3 Interrelationship between the different Correlations

The correlations mentioned above are not independent from each other given that the different quantities are intertwined by various fundamental relations. For instance, in elliptical galaxies the velocity dispersion is related to the luminosity due to the empirical Faber-Jackson relation (Faber & Jackson 1976) of the form $\sigma^\gamma \propto L$ where γ is close to 4. The Faber-Jackson relation follows directly form the virial theorem and the assumption that the galaxy's luminosity is proportional to its mass. By plugging the Faber-Jackson relation into equation 1.5 $M_{BH} \propto L^{1.22}_{bulge}$ becomes $M_{BH} \propto \sigma^{4.88}$ which is relatively close to the values being derived from observations.

[4] http://blackhole.berkeley.edu

On the other hand, the virial theorem is also beneficial by linking the bulge mass to the velocity dispersion $M_{bulge} \propto R_e \sigma_e^2$. This relation can be derived by combining the gravitational potential energy $U = -\alpha \frac{G M^2}{R}$ of a mass distribution of radius R and mass M and its kinetic energy $K = \frac{3}{2} M \sigma_e^2$. The constant α depends on the density profile of the system. In virialized systems the relation simplifies to $M_{bulge} \propto \sigma_e^4$. Thus, the $M_{BH} - M_{bulge}$ correlation can be directly transformed into the $M_{BH} - \sigma$ correlation.

1.2.4 SMBH evolution

The scaling relations mentioned above were studied extensively in the last few years. As they connect properties of entirely different scales (bulge potentials on Kiloparsec scales against SMBH potentials extending much less than a Parsec), a link between the formation an evolution of the SMBH and its host galaxy is presumed. This connection is called 'Co-evolution' and is not yet completely understood.
In order to understand the full picture, it is sufficient to look at the evolution of SMBHs which is likewise an open field of research. Observations show that quasars existed much more numerous towards larger redshift. This indicates that SMBHs formed already very early. The observation of distant luminous quasars suggests that SMBHs evolved already inside of the first massive galaxies being formed. Several hypotheses for the formation mechanisms of the progenitors of SMBHs were proposed. Figure 1.3 shows three possible scenarios which are described in Volonteri (2012). Common between the different scenarios is that they start with a dark matter halo which was formed out of cosmological density fluctuations in an early stage of the universe. Enclosed in this dark matter halo is a concentration of gas which will eventually contribute to the formation of the central SMBHs.

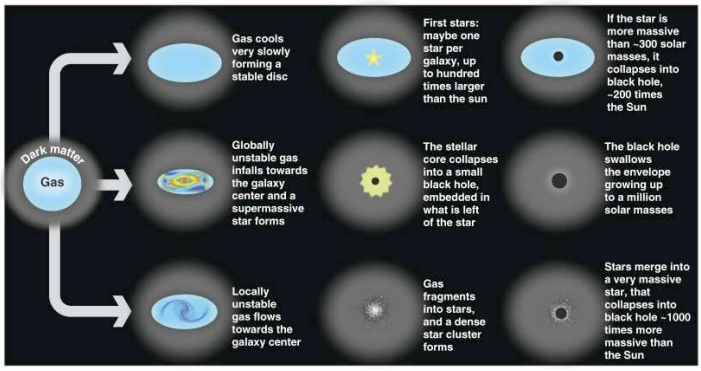

Figure 1.3: *Three possible scenarios of SMBH evolution taken from Volonteri (2012). The tracks commonly start with a primeval galaxy composed of a concentration of gas within a dark matter halo. A part of the gas is taken to form the galactic SMBH by following one of the tracks.*

The first scenario describes SMBHs as remnants of the first generation of stars. The first stars are proposed to be metal-poor and thus being predominantly able to reach masses of a few hundred $M_\odot$ (Bromm & Larson 2004). If the stars' mass exceeds $300\,M_\odot$ it collapses without leaving a remnant but for a star with around $200\,M_\odot$ a massive BH is born. Due to accretion of matter, the BH grows until it reaches contemporary masses of about a $10^6 M_\odot$ or more. However, first population stars have not been detected yet and simulations indicate that the first stars were probably much less massive than $250\,M_\odot$ (Hosokawa et al. 2011).

Hence, the first scenario is very unlikely to explain the observed SMBH population.

Another model associates SMBHs with dynamical instabilities that occur either in the gaseous or stellar component of proto-galaxies. In the general proto-galactic setting gas cools down and contracts until rotation equilibrates the contraction. This typically happens before reaching extreme densities and gas collapsing to a SMBH. However, gravitational instabilities can omit rotational support and transport additional mass into the collapsing gas. Consequently, SMBHs can be formed. Two alternative ways of SMBH formation are proposed depending on the size of the instabilities.
In the first model the large gas cloud collapses into a 'quasi-star' (Begelmann et al. 2006, Johnson et al. 2012). Global gas instabilities induce very fast gas accumulation resulting into the creation of a supermassive star of about $10^6\,M_\odot$. In order to not explode in a large supernova but collapsing instead, the gas must accumulate in less than around 2 million years which is the thermonuclear time scale). When the core of the supermassive star collapses, a BH of around $20\,M_\odot$ forms in its center. Still being enveloped from the shell of the dying star the formed BH can accrue matter very rapidly. It quickly turns into an intermediate-mass BH and potentially into a SMBH provided that the accretion-rate is not quenched at higher masses.

In the second model SMBHs form from dense stellar clusters (Spitzer 1987, Devecchi & Volonteri 2009). Local instabilities drive gas flow towards the galaxy's center forming a stellar cluster. Stellar clusters are so dense, that star-star collisions can create a massive star of a few thousand $M_\odot$. Even before heavy elements accrue, the massive star collapses into a BH having a similar mass to its progenitor. When the abundance of heavy elements increases, though, powerful stellar winds occur and carry a large fraction of the stellar mass away, before the heavy star evolves into a stellar BH. Therefore, this scenario only works in the early universe.

The different scenarios do not utterly eliminate each other. However, currently no direct observation gives evidence for a specific formation scenario. Common between the different pathways, though, is that all scenarios show a strong connection between the formation of SMBHs and their host galaxy.

1.2.5 Convergence concept

Another approach to explain the scaling relations associates 'hierarchical assembly of black hole and stellar mass through galaxy merging' (Jahnke & Macciò 2011). Instead of physical coupling the scaling relations might be the result of a statistical convergence process (Peng 2007). Peng claims that 'every arbitrary M_{BH}/M_{bulge} ratio of the early universe converges towards a linear trend' due to natural galaxy and halo merging. In that case, extreme M_{BH}/M_{bulge} ratios would be sorted out by the large number of mergers and the ensemble average.
In order to investigate Pengs theory, Jahnke & Macciò use simulations to construct dark matter halo merger trees in a feedback- and coupling-free environment. Figure 1.4 shows the result of their analysis. The blue points show an uncorrelated initial distribution of SMBH and bulge masses at a large redshift. After some time has passed a linear relationship has established between M_{BH} and M_{bulge} under any arbitrary initial condition (red points). It can be noted that the scatter is smaller for SMBHs of larger masses which undergo more merger processes.

The study shows that the SMBH-host galaxy correlations are the natural result of the

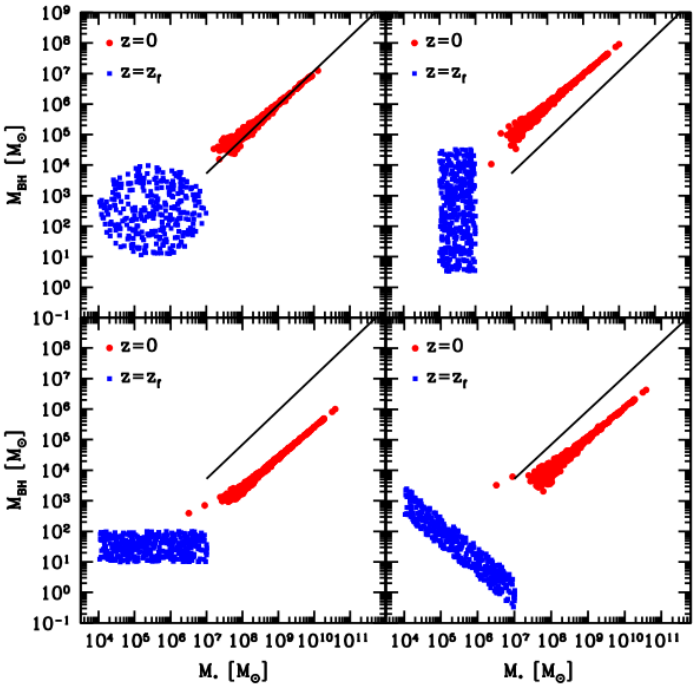

Figure 1.4: *Simulated scaling relations for four arbitrary initial conditions. At a chosen early redshift z_f, the $M_{BH}-M_{bulge}$ distribution is uncorrelated and constrained by initial conditions (blue points). At z=0 a tight correlation is generated by merger processes (red points). The black line indicates the observed $M_{BH}-M_{bulge}$ relationship. The figure was taken from Jahnke $ Macció (2011).*

galaxy merger history. Provided that the galaxies have experienced enough mergers in their past life, the scaling relations are not coupled to feedback between the SMBHs and their host galaxies.

1.3 Key aims of this work

Further research is required to understand and rate the different hypothesises of the scaling relations. It is crucial to explore the low and large mass end of the scaling relations to better constrain the scaling relations. This thesis deals with the quest of determining the presence and mass of a possible SMBH in the spiral galaxy NGC 4414. By analysing the kinematics and dynamics of NGC 4414 it is possible to search for a large central mass in the order of a few million solar masses. By combining the known velocity dispersion σ of NGC 4414 with equation 1.4, one can expected to find a SMBH in the mid to low end mass region of the scaling relations.

To investigate the presence of a SMBH the method of stellar dynamics was used. The main idea of this method is described in the following. As Newton demonstrated in his law of gravitation, the motion of objects is determined by potential fields. In very large scales gravitation is the only force that matters. Hence, by tracking the motion of stars in a galaxy their underlying gravitational potential can be inferred. The galactic gravitational potential, which is derived from the stellar motion, is composed of the gravitational potentials of various components: Primarily, the potential of the cluster of stars, a central black hole (when a black hole is present) and dark matter. In short, this model can be mathematically described as

$$\Phi_{grav} = \underbrace{\Phi_{stellar}}_{L_{stellar} \times M/L} + \Phi_{BH} + \Phi_{DM} \tag{1.7}$$

Although the gravitational potential of the black hole is not directly measurable, it can be deduced from the other components. Luckily, it is possible to quantify the remaining potentials.
The stellar potential $\Phi_{stellar}$ of NGC 4414 can be derived from its stellar luminosity combined with a M/L; the underlying potential is inferred from the galaxy's kinematics combined with a dynamical Jeans model. Observations of the kinematics are placed to the inner $3'' \times 3''$ region of NGC 4414. Hence, the dark matter component was not included in the Jeans model as it contributes only a few percentage (Vallejo et al. 2003) within the central regions.
In order to determine the central mass the dynamical Jeans model is constructed from a combination of photometric and kinematic data. Therefore, several steps have to be traversed:

1. Creating a photometric model
2. Deriving the kinematics from integral field data (Line Of Sight Velocity Distribution)
3. Determining the width and therefore the sharpness of the Point Spread Function
4. Combining the photometric and kinematic results to constrain a dynamical Jeans model using the Jeans Anisotropic MGE modelling method
5. Deriving the SMBH's mass

Chapter 2

Mass Measurement of SMBHs

2.1 Measuring methods

Method	Telescope	Scale (R_S)	M_{BH} Range ($M_\odot$)	# of SMBH Detections
Stellar Dynamics	HST,...	10^6	$10^7 - 3 \times 10^9$	17
Stellar Proper Motion	Keck, NTT, VLT	1000	4×10^6	1
Gas Dynamics	mostly HST	10^6	$7 \times 10^7 - 4 \times 10^9$	11
H_2O Megamasers	VLBI	10^4	4×10^7	2
Reverberation Mapping	Ground based Optical	600	$10^6 - 4 \times 10^8$	36

Table 2.1: *An overview of the methods used to determine SMBH masses. The table shows the given method, telescopes that are needed for the observations, the typical distance between the probed material and the center of the SMBH, the range of detected SMBHs covered and the number of detections based on the corresponding method. (Table taken from Ferrarese & Ford 2004)*

SMBHs can be detected based on i) their gravitational effect on surrounding matter or ii) the radiation of accreted matter. Measurement methods for determining the SMBH's masses can be distinguished into direct and indirect methods. In direct measurements the mass is directly derived from the dynamics of stars or gas which are accelerated by the black hole. In indirect methods the SMBH's masses can be deduced from observables that are correlated with the masses such as the velocity dispersion of bulge stars, in the $M_{BH} - \sigma$ relationship, or the bulge luminosity, in the $M_{BH} - L_{bulge}$ relationship, which where mentioned above.

In the following, I will give a brief description of several kinematical methods. Common between the different methods is that the SMBHs sphere of influence must be at least approximately resolved as was mentioned above. If the spatial resolution of the observations is much smaller, the gravitational influence region of the SMBH is not resolvable and the SMBH cannot be detected. For most galaxies the high spatial resolution is only achieved with the use of Hubble Space Telescope (HST) data, ground-based adaptive optics or VLBI.

2.1.1 Stellar Dynamics Method

The first method to describe is the stellar dynamics method. By studying the motion of stars in the center of galaxies one can get information about the presence and mass of SMBHs. As

most galaxies can be regarded as collisionless systems, the motion of the stars is essentially determined by the combined gravitational potential of the total number of stars in the galaxies and the central SMBH. In some cases dark matter also has to be considered.

Within the Milky Way, the kinematics of stars can be described with seven degrees of freedom. Their position x,y,z, their 3-dimensional motion v_x,v_y,v_z and the time t. The motion can be inferred from the stars' proper motion and their radial velocities. However, as most of the stars are located far away, their proper motion vector is very small and the stars have to be monitored for many years. Measuring supermassive black holes in more distant galaxies becomes more complicated as the orbits of individual stars, unlike in our own galaxy, cannot be resolved spatially. Instead, the collective motion of stars has to be described statistically by defining a velocity distribution function. As we can measure motions only along the line-of-sight due to Doppler shift, the velocity distribution function is defined along the line-of-sight (LOSVD). A Gaussian curve can generally parametrise the LOSVD quite well; more precise studies also include the so called Hermite polynomials to correct the shape. The LOSVD is mapped spectroscopically for different small spatial elements along a long slit, or on a 2-dimensional grid with an integral-field spectrograph. The data is then compared to a model which is constructed based on the gravitational potential of the SMBH, the galaxy's stars and sometimes dark matter. The SMBH potential is one of the free parameters and can be varied to find the best fit. The best fitting model provides the best estimate for the SMBH mass. As the method of stellar dynamics is applied in this thesis, the different steps will be further elaborated in the following chapters.
There are two main approaches to construct the stellar dynamical model. The most common approach to constrain the BH mass and mass-to-light ratio of the stars is the orbit superposition method of Schwarzschild (1979) which simultaneously optimizes the fit to the surface brightness distribution and the line-of sight kinematics of the stars within the nuclear region. A less general approach is the anisotropic Jeans modelling method (Binney et al. 1990, Cappellari 2008) which is applied in this thesis. While the orbit superposition method models a library of orbits of stars and superposes them, the Jeans modelling method matches the observed kinematics to the second moment of the Jeans equations.

With the application of the stellar dynamics technique more than 50 SMBH masses were estimated (Kormendy & Ho, 2013). However, the method is limited to relatively close galaxies due to the resolution requirement of the SMBH's sphere of influence. Furthermore, the method suffers from different problems. Dust in the center can effect the observed surface brightness distribution. The deprojection required inclination is often hardly measurable. Also, the inclusion of dark matter may be needed in the mass measurement.

2.1.2 Gas Dynamics of Nuclear Dust/Gas Disk

In some early-type galaxies one can find nuclear dust or gas disks, which can be studied to probe the center of galaxies. The procedure is very similar to the stellar dynamics method. In the gas dynamics method, nebular emission lines from the dust or gas disks are observed and analysed. Therefore, the velocities and velocity dispersions can be determined directly. For integral field spectroscopy or interferometric observations a 2-dimensional velocity field can then be constructed. The data is fitted with a line-of-sight projected model velocity field, which is calculated based on a combined gravitational potential of the stellar density, the central SMBH and the gas disk itself. The central SMBH is a free parameter and must be varied to find the best fit. An example of the SMBH determination is shown in 2.1 (which was adapted from Walsh et al. 2010). Observed data from M84 is compared to four

Keplerian fits based on different SMBH masses. The best fit is visibly not distinguishable but an approximate mass range can be specified.

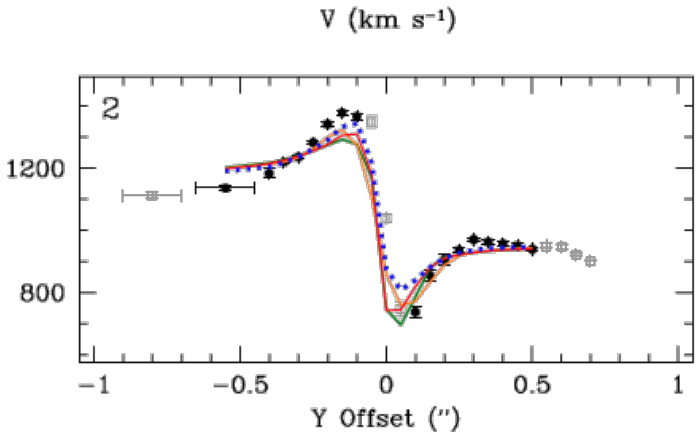

Figure 2.1: *Gas dynamical SMBH mass estimation of M84. The black stars indicate the observational data, Keplerian fits are shown in orange, blue, green and red lines corresponding to the SMBH masses 4.2, 4.3, 4.5 and* $4.7 \cdot 10^8\, M_\odot$. *The best fit is hardly identifiable with the naked eye. Figure taken from Walsh et al. (2010).*

The gas dynamics method also suffers from a number of caveats. The gas has to be ordered and mainly influenced by the SMBH's gravitational potential. However, there are many processes that can affect the gases motion like magnetic fields, turbulence or shocks. When these effects occur, the data deviates from a Keplerian profile leading to inaccurate estimates for M_{BH}.
In the last decade, gas dynamics have been studied for several elliptical and spiral galaxies. The measured SMBH masses reveal a similar range to stellar dynamics. Indeed, the stellar dynamics and the gas dynamics methods are complementary to each other. Gas disks are rare in the 'elongated, fainter ellipticals with a large surface brightness', which are the typical targets for stellar dynamics. On the other hand, the large amount of dust due to the disk makes stellar dynamics rather challenging (Ferrarese & Ford 2005). While earlier studies focussed on ionized gas kinematics, research was recently also extended towards molecular gas kinematics (Davis et al. 2013).

2.1.3 Reverberation Mapping

An alternative method that can be applied on BHs in active galactic nuclei (AGNs) is based on reverberation mapping (RM) (Blandford & McKee 1982, Peterson 2001, Peterson & Horne 2004). AGNs are the inner region of active galaxies where the central SMBH is fed with accreted matter and thus causing the vast AGN luminosity. As soon as matter cannot be accreted anymore the nucleus cannot radiate anymore, the galaxy stops being active. This is the case for most galaxies in the local universe (e.g Sgr A*, M31*). However, this method can be used to determine masses of BHs in distant galaxies, where the small angular diameter of galaxies renders kinematical methods impossible.

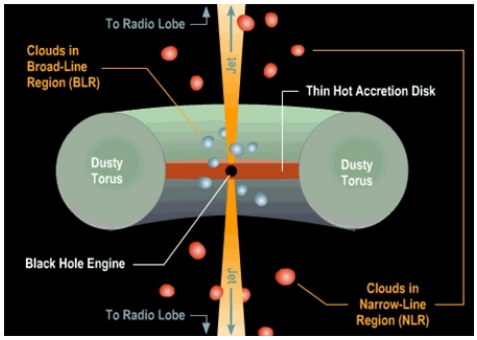

Figure 2.2: *The structure of AGNs. The SMBH and its thin accretion disk are surrounded by a thick and dusty torus. Perpendicular to the accretion disk a jet emerges the SMBH.*

In order to explain the RM method it is helpful to get a glance at the composition of AGNs. Figure 2.2 shows the different components of AGNs. In the core regions, AGNs consist of a SMBH which is surrounded by an accretion disk of accreted matter. The accretion disk has a radial dependent characteristic temperature. Therefore, the thermal emission of the accretion disk results into a broad continuum emission. Perpendicular to the accretion disk a concentrated jet of outflowing plasma emerges the SMBH. The jet is collimated by the twisting of magnetic fields in the accretion disk.
Directly above the accretion disk the so-called Broad-Line-Region (BLR) can be observed. BLRs are strongly ionized clouds emitting characteristic broad emission lines in the optical and ultraviolet giving this region its name. The broad emission lines arise from the fast movement of the clouds smearing the spectral lines due to Doppler shift. BLR clouds can gain velocities of around 1000 to 10.000 km/s.
A dust torus shields the inner regions. Corresponding to the orientation of the AGN towards us, the torus can hide the BLR from our view.
Beyond the dust torus another region of clouds moving with smaller velocity of around 100 km/s can be found. The emitted emission lines are less Doppler broadened and thus are called Narrow-Line-Region (NLR).

The basic idea behind RM is to achieve the structure and kinematics of the BLR by observing the response of the BLR to flux changes in the continuum.
Conveniently, the BLR is emitting light because its nuclear gas is heated and ionized by the high-energetic radiation of its environment. Primarily the radiation originates from the continuum radiation of the accretion disk. As the high-energetic accretion disk continuum flux is time-variable, it is expected that the broad emission-line fluxes also vary over time. Declining continuum flux results into a smaller emission-line flux. Indeed, the BLR variation response is observed time-delayed due to the finite extend of the BLR. The time-delay Δt can be directly identified with the light-travel time $\Delta t \approx r/c$ and thus with the geometry of the BLR.
Hence, RM provides the size-scale and the velocity (from the Doppler broadening) of the BLR gas close to the BH. The central mass can be deduced from these quantities via the Virial theorem (Müller 2007)

$$GM_{BH} = fR_{BLR}(\sigma_{BLR})^2 \tag{2.1}$$

where σ_{BLR} is the velocity dispersion of the gas in the BLR moving close to the BH, R_{BLR} is the radius of the BLR, G is the gravitational constant and f is a scaling or projection factor that depends on the shape of the BLR.

RM is a very powerful tool as it provides BH measurements beyond the galactic neighbourhood. Using the RM method, mass estimates for around 50 SMBHs in the large mass region could be measured. However, systematic uncertainties remain due to the unknown geometry and dynamics of the gas. These uncertainties are integrated in the scaling factor f. An empirical calibration for the scaling factor was established by comparing the measured masses with the tight correlations between the SMBH mass and the bulge velocity dispersion that was found in quiescent galaxies. It is a crucial fact, that a basic assumption is that AGNs and quiescent galaxies fulfil the same correlation.

Therefore, RM measurements have to be calibrated by other methods and as such rely strictly on dynamical measurements based on kinematics.

2.1.4 Maser Dynamics Method of Molecular Gas

Another kinematic method that is based on molecular gas dynamics requires maser line emission close to the SMBH. A maser ('microwave amplification by stimulated emission of radiation') produces coherent electromagnetic waves based on the principle of stimulated emission and can be imagined similar to an ordinary laser working in the microwave regime. Water masers (seen at the 22 GHz line of the ortho H_2O state of gaseous water) can generally be found in a molecular gas torus in AGNs. The material that generates the masers is orbiting the central SMBH. Therefore, by tracing the masing material the gravitational BH potential can be determined. This leads us to the mass of the SMBH.

Before giving a more elaborate description of the BH determination, I would like to refer to the question: 'How were these water masers generated?' Neufeld, Maloney and Conger (1994) give a sophisticated explanation by analysing the physical and chemical conditions of the circumnuclear gas torus. Hereby, circumnuclear describes that the gas is situated around the SMBH nucleus.
Neufeld et al. state that the masing region - a circumnuclear molecular cloud of gas and dust - is illuminated and heated by X-ray radiation coming from the central SMBH. The inner edge of the cloud is directly irradiated by the X-ray flux, the upper and lower surface of the cloud are only illuminated by scattered X-ray radiation. This can be imagined as a sandwich structure (Ferrarese & Ford 2005). Having a high water portion the molecular cloud generates collisionally pumped $H_2\,O$ radiation.
However, to achieve a strong signal an adequate long path-length through the disk has to be traversed by the radiation. Therefore, it is understandable that all water maser candidates were found in Seyfert 2 and Liner galaxies possessing a disk which is orientated almost edge-on towards us. Water masers are useful to determine SMBH masses as the microwave emitting molecular gas is orbiting around the SMBH. The Keplerian motion of gas clouds can be measured. Not many maser measurements have been conducted yet for reasons related to it's complex nature. Maser Dynamics are a powerful tool as they combine two particular advantages i) dust which surrounds the circumnuclear maser regions can be mapped ii) Maser dynamical measurements reach an unprecedent angular resolution of a few milli arcseconds

Unfortunately water masers are not very common (Ferrarese & Ford 2005). In different surveys targeting different AGN types only a few H_2O Masers could be found: 13 among 354 galaxies within 10 Mpc by Braatz, Wilson & Henkel (1994,1996), 1 among 26 AGNs by Greenhill et al. (1997), 1 among 131 AGNs observed with the Parkes Observatory (Greenhill et al. 2002). In addition, H_2O mass measurements can be very critical and unreliable. Either the disk cannot be spatially resolved, the disk inclination is not known or the rotation is not

Keplerian shaped (Schulze 2011).
In the last few years, more successful measurements could be conducted using VLBI observations. The Seyfert galaxy NGC 4258 harbours a SMBH mass of around $3.78 \times 10^7\ M_\odot$ within 0.14 pc (Kormendy & Ho 2013) and in NGC 3079 a SMBH of around $2 \times 10^6{}_\odot$ within 0.4 pc (Kondratko et al. 2004) could be measured. VLBI provides a spatial resolution which is about two orders of magnitude higher than with HST and with it a deep insight into the core of galaxies. This allows the detection and measurement of lower mass SMBHs.

Water masers are not only valuable to determine SMBH masses, but can also be used as direct distance measurement to a galaxy which is independent from the cosmic distance ladder (Herrnstein et al. 1999, de Grijs 2011).

2.1.5 Prospect to Potential Future Determination Methods

SMBHs are still a topic of immense study. Among others, questions include the search of smaller intermediate sized black holes and how black holes evolve from larger redshifts. A higher spatial resolution is needed, the limits of HST mass estimations have almost been reached. Batcheldor & Koekemoer (2009) provide an interesting outlook into the future of SMBH mass determination and show that the next James-Webb-Space Telescope will not significantly improve the measurements. Furthermore, they compare a 30 m ground-based optical-NIR observatory to an UVOIR 16 m space-based observatory and estimate that the 16 m telescope could theoretically be used to determine SMBH masses up to z=10 by using Lyα lines. The possibilities could go down to $M_{BH} \approx 10^{4.5} M_\odot$ in the Local Group and thus improve the opportunity to detect intermediate black holes. A 30 m telescope, instead, would be able to detect black holes down to $M_{BH} \approx 10^{4.2} M_\odot$ in the Local Group, but only up to $z \approx 4.8$. However, the ground-based 30 m telescope depends strongly on the AO development.

Furthermore, new methods have to be developed to study BH masses at different mass ranges. Müller (2007) introduces new methods that might become important in the future. The methods are classified as eruptive methods, obscurative methods, aberrative methods, temporal methods and gravitational wave-induced methods. Under aberrative methods, he discusses the use of gravitational lensing to determine SMBHs. Visual objects close to SMBHs appear to be distorted. Much work has been gone to the simulation of light distortion. Simulations are of particular interest as they can be used to constrain SMBH parameters. For an elaborate explanation of the different methods I would like to refer to Müller's paper.

2.2 Observational evidence

The year 1963 can be considered as the starting point of SMBH research. That was when Schmidt discovered the radio source 3C 273, later categorised as the first quasar ('quasistellar object'). Shortly thereafter, the idea developed that quasars and other active galactic nuclei (AGNs) were powered by accretion onto SMBHs (Hoyle & Fowler 1963, Salpeter 1964, Zel'dovich & Novikov 1964). There was no dynamical evidence that SMBHs with the required masses of $M_{BH} \approx 10^6$-$10^9 M_\odot$ actually existed. However, the upper limit of the SMBH masses are only around 0.1 % of the stellar masses of their host galaxies. Hence, BHs are expected to dominate the local gravity and to lead to the observable dynamical consequences only inside a sphere of influence of around 1 to 100 pc. At distances between one to 20 Mpc for nearby galaxies, this corresponds to around 0.1 to 1 arcsec. Therefore, it was impossible to detect SMBHs until the mid-to-late 1980s , when better instruments and larger telescopes became

available to observers. Today more than 50 SMBH masses of different scale and distance have been estimated. Kormendy & Ho (2013) provide a list of detected SMBHs, having been estimated until 2013, in their review paper. I will present some SMBH cases in the following section.

2.2.1 Sgr A*

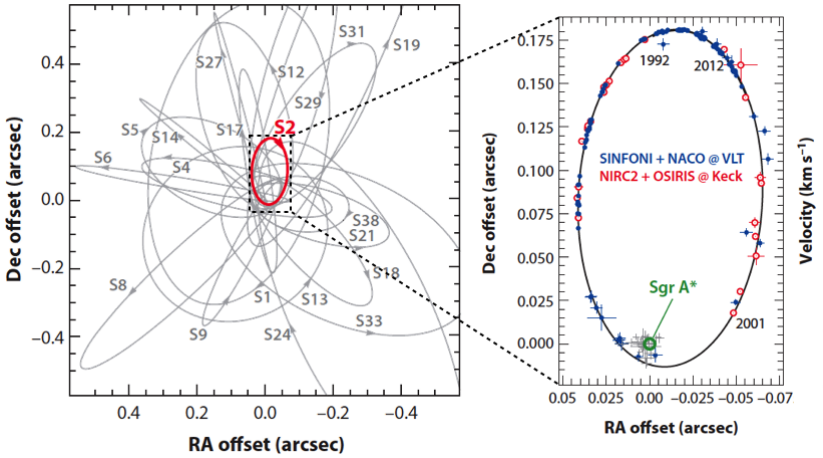

Figure 2.3: *Orbits of the stars in the Galactic Center. Panel (a) shows the orbits of almost 20 stars which are in the vicinity of the SMBH located at the position of Sgr A*. The orbits were measured by monitoring the proper motion of the stars. Images taken from Kormendy & Ho (2013).*

To find the closest SMBH, one must not look into regions far away. In fact, the closest black hole is only about 8 kpc away: Our own galaxy harbours a SMBH. Albeit its visible light is covered by a layer of dust, a bright object could still be detected from radio radiation. This object is called Sagittarius A* (Sgr A*) and is very compact ($0.25 \times 10^{-3}\,''$ at $\lambda = 0.69\,\mathrm{cm}$)(Bower et al. 2004, Doeleman et al. 2001) and very massive, as it does not show proper motion (Reid et al. 2003).
A long series of ground-based observations provides very accurate measurements of Sgr A*. The mass determinations are based on the stellar dynamics method. As the galactic center is very close ($d \approx 8.28 \pm 0.33\,\mathrm{kpc}$ (Genzel, Eisenhauser und Gillesen 2010), individual stars can be resolved and their proper motions can be measured with Speckle-methods and adaptive optics. More than 30 stars within $\approx 5''$ of Sgr A* have known proper motions and radial velocities measured over many years. Accelerated by its central SMBH, most of the stars within $0.''6$ have a proper motion larger than 1000 km/s. In the focal point of the orbits Sgr A* is located. From the observed kinematics the mass between $001\,\mathrm{pc} < r < 0.5\,\mathrm{pc}$ could be inferred as around

$$M = (4.3 \pm 0.36) \times 10^6 M_\odot \tag{2.2}$$

(Genzel, Eisenhauser, Gillesen 2010). Even before studying proper motions of the surrounding stars, the BH of the Galactc Center could be constrained with gas kinematics. Having a steep increase in the gas velocity from around 100 km/s at 1.7 pc towards 700 km/s at 0.1 implied a virial mass of around $10^6\,M_\odot$. Due to the very high resolution achieved in the Galactic center, this is by far the most accurate black hole mass measurement.

2.2.2 Other galaxies

The very first dynamical discovery of a SMBH was in the elliptical dwarf galaxy M32 in 1984 (Tonry 1984). M32 is a companion galaxy of Andromeda and belongs to the Local group. Hence, it is located very close to our own Galaxy. In his study, Tonry found a rise in the galaxy's velocity dispersion towards its center and and an unresolved jump in its rotation curve. From his results he concluded the 'presence of a central dark object of about $5 \times 10^6 M_\odot$'. The estimation of the mass of the SMBH in M32, however, was slightly overestimated due to an insufficient resolution. 10 years later the resolution had improved by a factor of four, but observations revealed a still very similar SMBH mass of about $2.1 \times 10^6 M_\odot$ (van der Marel et al. 1994). Today M32 features the most accurate M_{BH} measurement based on unresolved stellar motion. Its value has evened out to about $(2.4 \pm 1.0) \times M_\odot$ (van den Bosch & de Zeeuw 2010). Furthermore, first approaches to study M32's M_{BH} with resolved stellar populations can be found in the recent literature (Howley et al. 2012).
The history of M32 SMBH measurements is very informative to our confidence in SMBH mass determinations. Even with a resolution improvement of a factor of 30, the M_{BH} masses have remained relatively stable.

The strongest BH case next to our Galaxy is NGC 4258. NGC 4258 is an SABbc spi-

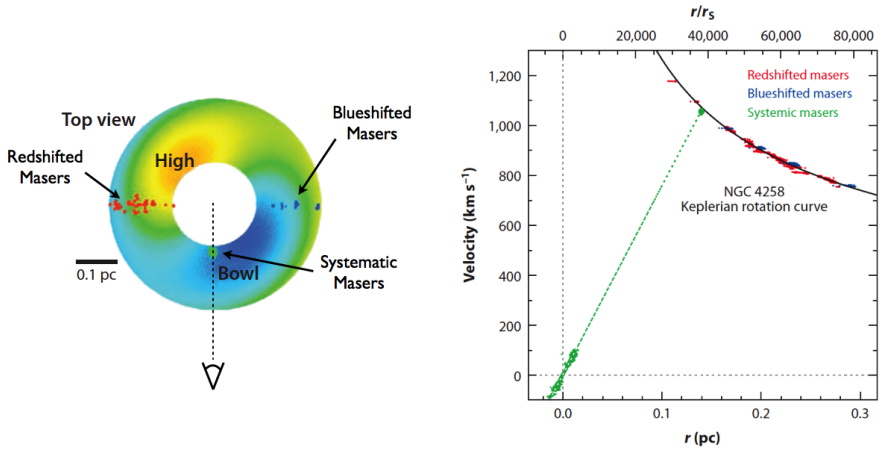

Figure 2.4: *Maser Dynamics to estimate M_{BH} in NGC 4258. The left panel illustrates the torus surrounding the central SMBH. The relative positions of non-systemic and near-systemic masers are shown in red, blue and green spots. The right panel shows the masers overplotted in rotation curve versus radius diagramme. Red and blue masers follow a Keplerian rotation curve, while the green masers follow a linear relationship through the origin. Images taken from Kormendy & Ho (2013).*

ral galaxy (between normal spiral and bulk spiral) at about 7.27 Mpc distance. Interestingly, NGC 4258 contains water megamasers which orbit in a torus surrounding its central SMBH. These water vapors give NGC 4258 its characteristic purple color. As described above, masers can be used dynamically to determine the galaxy's central mass. Maser dynamics provide two independent ways to measure SMBH masses. Firstly, non-systematic masers follow a Keplerian rotation curve $V \propto r^{-1/2}$(blue and red spots). The Keplerian motion indicates a central massive object with a mass of about $M_{BH} = V^2 R/G$. Using this method, Herrnstein et al. (2005) derive a SMBH mass of about $(3.81 \pm 0.01) \times 10^7 M_\odot$. On the other hand, drift and centripetal acceleration of near-systemic components can be used. Near systemic masers are directly in the line-of-sight between the central massive object and us. Under the

assumption that near-systemic masers have a circular motion around the center, one can use their centripetal acceleration to estimate the SMBH mass. Kormendy & Ho 2013 calculate the mass to about $(3.65 \pm 0.09) \times 10^7 M_\odot$. The two measurements are therefore very consistent with each other.

These are two interesting examples of SMBH measurements of the last three decades. In total more than 50 SMBH masses have been estimated. A relative complete list of SMBH measurements up-to-date is given in the review paper by Kormendy & Ho 2013. The determination of SMBHs was significantly improved in 1995 when the Hubble space telescope (HST) started its work. One of its goals was to confirm ground-based SMBH mass determinations at about five times better spatial resolution. Thus, mass estimates could be established with more accuracy. The next striking improvements arrived with the development of integral field spectroscopy and adaptive optics.

2.3 Necessary Observation Techniques

2.3.1 Integral Field Spectroscopy

The observations being analysed in this thesis were conducted with the Adaptive-Optics-assisted Near-Infrared Integral-Field Spectrograph (NIFS) that is mounted on the Gemini North telescope. Integral-field spectrography creates spectra in a two-dimensional field-of-view simultaneously in a single exposure. The spatial elements that contain spectra are called spaxels, which is a combination from pixel and spectrum. Using IFS it is possible to reconstruct 2-dimensional maps of the observed galaxy at arbitrary wavelengths. An integral field unit(IFU) observation results in a 'datacube', where for each spatial element (x,y) there is a spectrum, resulting in a 3D structure (a cube) defined with coordinates (x, y, λ).

Due to the simultaneity of spectra taking, IFS is a great improvement over traditional spectroscopy where the image is dispersed in a long-slit instrument. It is theoretically possible to get a similar result with slit spectroscopy by taking single exposures for many positions gridded over the galaxy. That procedure is very time-consuming, though, as the exposure time increases with size of the observed object.
Another advantage of IFS comes with its simultaneity. As the spectra are taken at the same time and position, the source coordinates and the point spread function will be the same in all images.

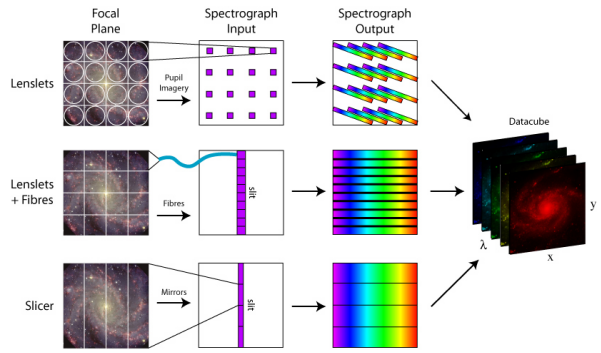

Figure 2.5: *Overview of different IFS techniques. Shown are from top to bottom the lenslet array technique, fibre bundles and image slicers. The different techniques can be combined to achieve an optimal result. Credit: M. Westmoquette.*

IFS can be distinguished into three main techniques depending on the way the input image is split: Lenslet arrays, fibre bundles and image slicers. Their concept is illustrated in figure 2.5 The lenslet array chops the input image with a microlens array. The light from each element is then concentrated into a small point and dispersed by a spectrograph. However, the disadvantage of this technique is that the CCD camera is used very inefficiently (compare figure 2.5).
A common IFS technique uses optical fibres to split the image. The input image is formed at one end of a 2-dimensional bundle of optical fibres which transfer the light to the spectrograph. As the fibres are flexible, a 2-dimensional field can be reformatted into one or more slits.
In a third approach, the image is first separated into slices. The slit is optically cut into smaller pieces and re-imaged onto the image-plane at multiple locations.
The different methods can also be combined to achieve an optimal efficiency. The NIFS instrument itself is build on a set of image slicer mirrors located at its f/256 focus. This method gives the best optical results and is often used.

2.3.2 Adaptive Optics

Adaptive Optics (AO) was developed to improve the performance of optical systems. When stellar light enters the Earth's atmosphere, the wave front can be distorted and moved due to atmospheric turbulence. Turbulence can be caused by different temperature layers or wind mixing cold and warm air and is called astronomical seeing. With naked eye this effect can be seen as twinkling of the stars. In a long exposure image taken with a telescope the observed star looks blurred out and indistinct. AO was developed to correct this perturbing seeing effects. The AO system is generally composed of three components. A wave front sensor

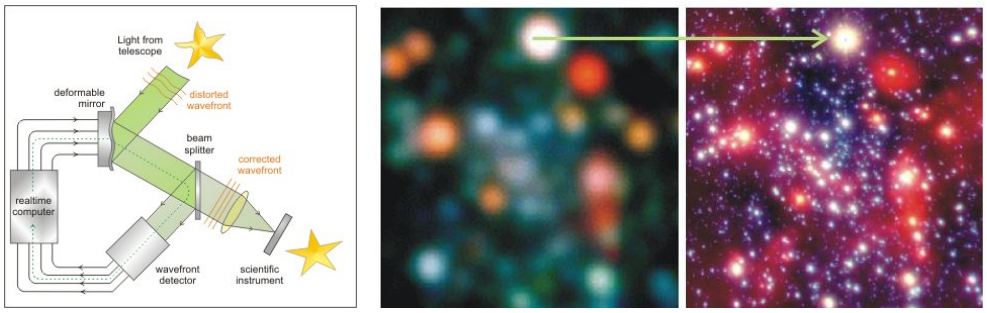

Figure 2.6: *Explanation of adaptive optics. The left panel shows a schematic of AO wave front correction. The middle/ right panel shows an image of the galactic center uncorrected and corrected (NAOS/CONICA, VLT). The resolution of the telescope improves significantly. Credits: MPE*

measures the optical distortions, a computer uses the measurements and calculates the optimal mirror shape to correct the distortions and finally the surface of a deformable mirror is reshaped accordingly (figure 2.6). The whole system cycles a few hundred times per second. The corrected wave front is then directed towards the instrument camera.

Many objects being observed are very faint making it impossible to be used to determine the distortion. Closely located brighter guide stars are required. Only if the light from the target passes approximately the same atmospheric layers as the guide star's light it can be corrected robustly. In some cases no natural guide star can be found close to the target. Then laser beams are used to generate reference sources called laser guide stars.

Chapter 3

The Spiral Galaxy NGC 4414

Figure 3.1: *Galaxy NGC 4414 (Credits by NASA).*

NGC 4414 was found in 1785 from Wilhelm Herschel and such added to his New General Catalogue. NGC 4414 can be classified as an unbarred spiral galaxy of the Type Sc (de Vaucouleurs et. al. 1991). In Sc type galaxies, the mass and luminosity of the bulge are much lower than that of the disk. Thus, the mass modelling is simplified, as the galaxy can be modelled in basically two components: A small bulge component and a thin disk component. NGC 4414 can be found at around 19.2 Mpc distance in the constellation Coma Berenices on the northern edge of the Virgo-Cluster. It is floating in isolation without gravitational influence of other visibe close objects (Vallejo et al. 2002).
Being part of the Hubble Space Telescope Cepheid key project to measure distances based on Cepheids, the distance of NGC 4414 is well-established. Table 3.1 (taken from Vallejo et al. 2002) lists the basic properties of NGC 4414.

Recent studies (Vallejo et al. 2002) imply that NGC 4414 could host a supermassive black hole in its center. The supermassive black hole leaves signatures in the motion of the stars surrounding it. It is the goal of this thesis to use these signatures to find further evidence for the supermassive black hole and to measure its mass.

Property		Reference
RA_{2000}	$12^h\,26^m\,27.1^s$	NED
DEC_{2000}	$31^\circ\,13'\,24.0''$	NED
Inclination	55°	Vallejo et al.(2002)
Position Angle	157°	Vallejo et al.(2002)
Distance	$19.2 + -2$ Mpc	Turner et al.(1998)
Redshift	0.002388	Rhee et al.(1996)
Systemic Velocity	716 km/s	Braine et al.(1993)
Effective Radius	$0.1'$	Thornley 1996
Velocity Dispersion	110km/s	Hyperleda

Table 3.1: Basic properties of NGC 4414 taken from the literature.

Chapter 4

Parametrisation of the Surface Brightness

4.1 Fundamental Idea

In this chapter the surface brightness profile of NGC 4414 has been studied. In combination with the M/L, the surface brightness provides information about the mass of the stars (or better luminous matter) of the galaxy which has to be considered in the dynamical model of the galaxy.

As the surface brightness is a 2-dimensional quantity it has to be de-projected to deduce the underlying luminosity density. For this purpose, the inclination angle of the galaxy is required. The luminosity density can then be translated into the mass density of the luminous matter by using the M/L.

4.2 Surface brightness profiles

One of the most characteristic features of galaxies is their surface brightness profile. Light emitted from galaxies can be described by their apparent brightness distribution on the night sky defined as intensity $I(x, y)$ at a position (x, y). Since most galaxies are very symmetric, the surface brightness is often described by azimuthal averaged radial profiles I(R) represented by concentric circles or ellipses. The total luminosity can then be derived by an integral over the radial elongation

$$L_{total} = 2\pi \int_0^R dR'\, I(R')R' \tag{4.1}$$

The surface brightness holds a very interesting and useful characteristic. While the brightness of an object decreases with distance, the surface brightness is independent of the distance. This fact can be explained as follows: As mentioned above, the brightness of an object decreases with the square of its distance from the observer. On the other hand, a larger area of the object is covered in the same field-of-view for a larger distance. The two effects combined cancel each other and thus,regardless of its distance, the surface brightness of an object remains the same. Therefore, it is an easy measurable observable to describe intrinsic properties of the galaxy. However, it has to be noted that the surface brightness profile depends strongly on the filter system that is used to observe. This is based on the fact that 1)the galaxy emits a different amount of light at different wavelengths depending on the internal physical processes, 2)dust between the galaxy and the observer can scatter light which is also

wavelength dependent.
The analysis of the surface brightness reveals a lot of information of the galaxy. For instance, one can determine the size of a galaxy and study how the light distribution evolves with radius. The different morphology classifications are also based on the surface brightness. Furthermore, the surface brightness can be studied to derive the underlying luminosity density and construct mass models.

A common way to describe the surface brightness, is to fit a pre-defined model to the galaxy's light profile. Over the last few decades a number of different models have been established (Schneider 2008). In 1948, the de Vaucouleurs profile with radial $\exp(R^{1/4})$ dependency was developed (de Vaucouleurs 1948). The de Vaucouleurs profile describes elliptical galaxies and the bulge component of spiral galaxies quite appropriately. Freeman (1970) found that spiral galaxies have a more complicated component structure. Therefore, they are instead observed to have an exponential disk profile $\propto \exp(R/R_0)$ plus a de Vaucouleur bulge profile. However, these descriptions are very simple. Over the years the quality of photometric data has improved greatly and thus, more and more structures can now be better resolved. Hence, it is feasible to use more sophisticated models. Among these are the Sérsic law (Sérsic 1968) that uses an $\exp(r^{1/n})$ profile, King surface profile for isotropic clusters (King 1966) and the Nuker profile (Lauer 1995) to describe the core of S0 and elliptical galaxies. In fact, the de Vaucouleurs law is a special case of the Sérsic law.
In this thesis I will model the surface brightness profile of NGC 4414 with a Multi Gaussian Expansion (MGE) which has been explained in detail in a later section. The Multi Gaussian Expansion method reproduces the photometry of a galaxy accurately, allowing ellipticity variations and isophotes which are not ellipse-shaped.

4.3 Imaging Dataset

My first task was to get appropriate imaging data to measure the surface brightness of NGC 4414. To obtain optimal results, the data had to fulfil a number of criteria which are as follows:

- A large field-of-view to cover the light of the whole galaxy without omitting the outer regions
- High-resolution data in the very central regions where the central mass is mostly dominating
- Images should not show saturation effects in the center

These goals could be accomplished by combining high-resolution data in the central regions with data having a large field-of-view, but inferior spatial resolution.
In the late 20th century, NGC 4414 was part of the Hubble Space Telescope (HST) Cepheid key project (Turner et al. 1998) with the aim to measure extragalactic distance scales using cepheids. Thus, a number of very deep WFPC/HST observations of NGC 4414 covering different bands are available in the archive.
I retrieved the HST/WFPC2 imaging data from the ESA Hubble Science Archive and the Hubble Legacy Archive, which generate automatically reduced and calibrated data. The prior data calibration process involve the steps of masking bad pixels, performing an analog-to-digital (A/D) correction, correcting bias, dark and shutter shading (WFPC2 Handbook). The HST PC image is very essential to resolve the central regions as it has a large resolution of 0.043 arcsecond pixel scale (compared to the wide field image having 0.1 arcsecond pixel

Optical band	Camera	Obs. date	total exposure time
F555W	WF	Apr. 1999	6400 s (mosaic)
F555W	WF	Apr. 1995	129720 s (mosaic)
F606W	PC	Jul. 2001	160 s

Table 4.1: Overview of HST images that were used within this thesis. Given are Optical band, Camera, Observing date and total observed time.

scale). Except one image, all of the WFPC2 images were saturated in the center. Therefore, it was not possible to remove cosmic rays in the usual way. That is why, I corrected the images for cosmics by determining pixels that had a large count gradient towards their neighbours and masking these before the MGE fitting.
The F555W images are mosaics, and thus, were combined from individual exposures, weighted for background signal and resampled to a pixel scale of 0.1 arcsecs using the multidrizzle algorithm (Fruchter & Hook 1998).

A second source for large field-of-view imaging data was the Sloan Digital Sky Survey (SDSS) database. Screening the sky with the ground-based Apache Point Observatory, SDSS has obtained deep, multi-colour images covering more than a quarter of the sky over eight years of operation. As the scanned areas of the sky overlap partially in the images, it is very convenient to create mosaics with 'arbitrary central points and extent' (as long as being in the observed survey). I used the Montage based online tool 'Image Mosaic Service' provided by NASA and Caltech and created a 0.2×0.2 square degree size mosaic centered around NGC 4414 in the g-, r- and i-band. Image Mosaic Service uses the SDSS observations and overlaps them by preserving the fluxes and astrometry.

4.4 Dust Correction

Dust can be distinguished into intergalactic dust, interstellar dust and interplanetary dust depending on its astronomical location. It consists typically of small, solid dust particles of up to $0.1\,\mu m$ size. The particles can physically interact with light of a studied object (e.g. stars) and therefore significantly alter observations. Knowing about the dust content between the observer and the observed object is very crucial in astrophysics.

Cosmic dust can be roughly imagined like mist on the Earth. When the air or space is filled with particles, light cannot propagate freely anymore, it appears dimmed. The light intensity attenuation can be described by two physical processes. Firstly, some of the photons are absorbed and their energy is converted into heat. This has the effect that the re-emitted light has decreased energy, blue light transforms into red or infrared light. Secondly, the dust particles can scatter photons out of the line-of-sight between star and the observer. This dimming of light is called 'extinction'. Extinction depends on the wavelengths of the light, the amount of dust between star and observer and the dust's chemical composition.

Dust can have a significant effect on the accuracy and reliability of photometric models as it alters the apparent shape of the galaxy and dims the light due to the wavelength dependent extinction. Not only the galaxy's intensity, but also its colour is changed by dust attenuation. Blue light is affected more strongly by absorption and scattering than red light.

Hence, the galaxy or star appears redder than it intrinsically is.
Figure 3.1 indicates large dust and gas patterns located in the disk of NGC 4414. The dust obscures the attained light of the galaxy in the SDSS/r-Band images, such that the actual surface brightness is not observable.
Using a method described in Scott et al. (2013) I corrected the SDSS/r-Band image on these extinction effects to be able to fit the MGE model (next section) to the underlying surface brightness profile. The main assumption of this method is that the dust can be summed up to a light absorbing screen between the observer and galaxy (Carollo et al. 1997, Cappellari et al. 2002b). Due to extinction this screen changes the intrinsic colour of the dust affected galaxy fragments, which are assumed to have the same intrinsic colour as the adjacent regions. Following this, the goal of the dust correction is to find the dust affected pixels and correct these using the Galactic Extinction law (Schlegel et al. 1998).

The correction itself involved a number of steps, which I will explain below. According

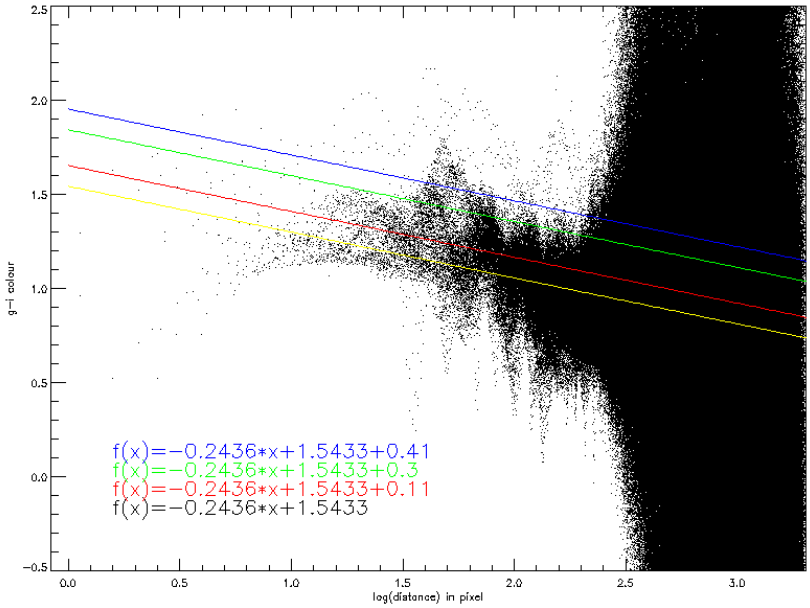

Figure 4.1: *Colour profile of the SDSS g-i map used for the dust correction. The best-fitting linear line obtained by a robust fit is shown in yellow. The other colours show the different thresholds given numerically in the lower edge of the plot. We finally decided that the red line to be the threshold, to assure the same width of the gradient under the line-fit and above. All pixels above the red line and for* $\log(d) < 2.5$ *[pixels] were corrected for extinction.*

to the Galactic Extinction law,

$$A_r = 1.15E(g-i) \tag{4.2}$$

the r-band extinction, A_r, is proportional to the colour excess $E(g-i)$. The colour excess denotes the difference between the intrinsic colour and the colour due to dust. This implies that from knowing the colour excess, for each pixel we have an estimate of the amount of light that is absorbed by dust. At first, I used the SDSS g-band and i-band mosaics to construct a g-i colour map. To make the images comparable, I had to measure the images' PSFs and degrade the better resolved image to the more diffused one. For the colour maps, the measured fluxes within the images had to be transformed to magnitudes. To be able to see the radial dependence of the colour, the position of each pixel was expressed in terms of the corresponding semi-major axis length. Therefore, the average ellipticity and position

angle of the original image was determined with the *find_galaxy.pro* [5] routine by Cappellari. This routine computes the weighted second-moment of the surface brightness above a given level outputting the central coordinates, the ellipticity and the position angle of the galaxy. With this information, I was able to make a colour profile by plotting the g-i colour over the logarithm of the semi-major axis distance.
With the assumption that the intrinsic galaxy colour varies linearly with the logarithm of the radius, I performed a robust linear fit to the colour profile to determine the underlying colour gradient of the galaxy. The robust IDL routine *ladfit* (minimizes the absolute deviation) was chosen to reduce the influence of the dusty regions. It has to be noted, that the linear fit was chosen for simplicity, not for accuracy reasons. Using the linear fit, a first order approximation of the trend of the underlying gradient can be achieved.
Figure 4.1 shows clearly the colour gradient that can generally be observed in spiral galaxies: While their central regions are redder, moving outwards the intrinsic colour is shifted towards blue. Therefore, two physical causes can be deduced.
On the one hand, the gradient results from a metallicity effect, which states the proportion of the galaxy's chemical elements heavier than hydrogen and helium. The amount of metall-rich stars, which appear redder, grows inwards
On the other hand, the colour gradient is a consequence of star formation. Star forming gas is less concentrated in the bulge than in the disk. Hence, the star population in the bulge is generally older and redder than in the disk.

The best fitting colour gradient (a function of radius) is then subtracted from every pixel to determine a E(g-i)-map. Using this knowledge, I determined a threshold above which the pixels were corrected. Looking at the colour profile, one can mark out a region under the line-fit that can be interpreted as part of the colour gradient. In order to continue this symmetrically above the line-fit, the threshold was chosen to be $E(g-i) > 0.11$. All pixels above this threshold are significantly affected by dust extinction and were corrected in the SDSS r-band image using the extinction law. Figure 4.2 shows a comparison of the uncorrected and the corrected r-band image in flux units. One can see that especially in the disk regions the flux is much more homogeneous than before the correction. The largest correction was around 35 per cent of the measured flux.
By measuring the dust we can also estimate the orientation of the galaxy towards us. Most of the dust was corrected on the left of the galaxy center. Accordingly, the left part of NGC 4414 is turned towards us, while the right fraction is facing away.

4.5 Multi-Gaussian Expansion

After correcting the significantly dust-affected parts of the r-image, I used the Multi-Gaussian Expansion (MGE)[6] modelling method which was elaborated by Monnet at al.(1992) and Ensellem et al.(1994). By making use of the MGE IDL implementation developed by Cappellari et al. (2002a) I create a photometric model of my imaging data. The basic idea of the MGE method is to parametrize the surface brightness using two-dimensional Gaussian functions. This simplifies the techniques of convolution and deprojection. Convolution has to be used when the instrumental and atmospheric Point Spread Function (PSF) is taken into account, deprojection when deriving the intrinsic stellar luminosity density from the observed galaxy photometry. In the case of axisymmetric MGE models, the MGE method also makes it easier

[5] www.astro.physics.ox.ac.uk/~mxc/software/
[6] www.astro.physics.ox.ac.uk/~mxc/software/

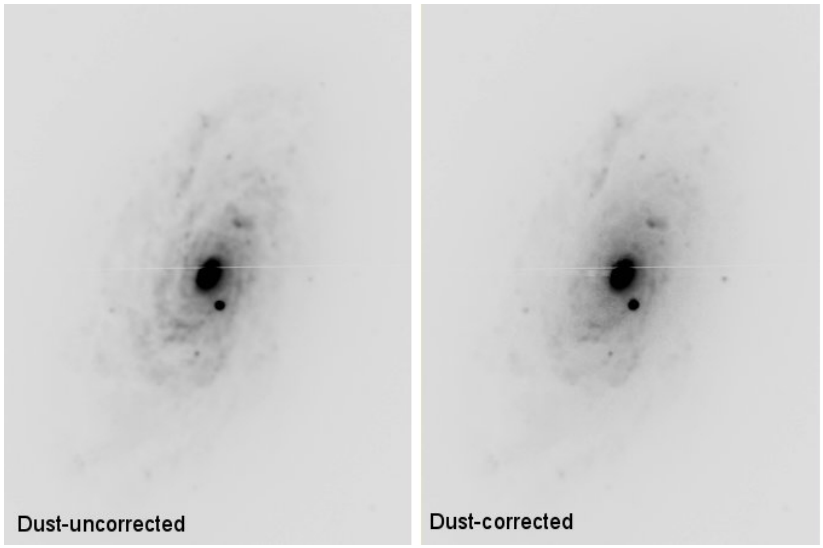

Figure 4.2: *Comparison of the dust-corrected and uncorrected image. Most of the correction was applied on the left part of the galaxy. The image extract covers around* $2' \times 3'$*, respectively. The lines in the center of the pictures are edge artefacts from montaging the single SDSS images.*

to solve the Jeans equations which are reduced to a double integral (Cappellari 2002a).
The following description of the MGE formalism is re-phrased from Cappellari (2002a) and Emsellem et al. (1994). For further studies and more complex models, I would like to refer to their papers.

Stars appear approximately point-shaped in a telescope. Their brightness is measured in magnitude units. However, in extended objects the surface brightness is used to measure the brightness. It indicates the brightness density of a specified area of the galaxy and varies with the radius. The MGE model is an approach to parametrize the variation of the surface brightness.
Given a Cartesian coordinate grid set on the center of the galaxy, the deconvolved surface brightness can be approximated by a sum of N Gaussians and therefore be written as:

$$S_{dec} = \sum_{R,\theta} S(R,\theta) = \sum_{j=1}^{N} \frac{L_j}{2\pi\sigma_j'^2 q_j'} exp\left\{-\frac{1}{2\sigma_j'^2}\left(x_j'^2 + \frac{y_j'^2}{q_j'^2}\right)\right\} \tag{4.3}$$

with the Cartesian coordinates relative to the central coordinates x_0, y_0

$$\begin{cases} x_j = R' sin(\theta' - \psi_j), \\ y_j = R' cos(\theta' - \psi_j), \end{cases} \tag{4.4}$$

where (R, θ) are polar coordinates of the disk plane centered in the galaxy nucleus. The single Gaussian component is described by 4 parameters:

$$\begin{cases} L_j & \text{total luminosity,} \\ \sigma_j' & \text{dispersion along major axis,} \\ q_j' & \text{axial ratio,} \\ \psi_j & \text{position angle (PA) measured counterclockwise between } y'\text{-axis and major axis} \end{cases} \tag{4.5}$$

Before the model can be compared with the observed surface brightness, the instrumental and atmospheric PSF has to be taken into account. If the PSF can approximately be modelled as sum of M circular Gaussians,

$$PSF_{model}(R') = \sum_{k=1}^{M} I_{*k}/(2\,\pi\sigma_k^{*2})\, exp\{-R'^2/(2\,\sigma_k^{*2})\} \tag{4.6}$$

with the relative weights scaled to one $\sum_{k=1}^{M} I_{*k} = 1$, the convolution between the deconvolved surface brightness and the PSF can be written as

$$S_{conv} = S_{dec} \otimes PSF_{model} = \sum_{j=1}^{N} L_j \sum_{k=1}^{M} \frac{I_{*k}}{2\pi\sigma_{jk}^2 q_{jk}} exp\left\{-\frac{1}{2\sigma_{jk}^2}\left(x_j'^2 + \frac{y_j'^2}{q_{jk}^2}\right)\right\} \tag{4.7}$$

The total luminosity of a single Gaussian does not change with convolution, but its shape is broadened. This can be easily seen in the formula above.
The best fitting MGE Model is found by minimizing the χ^2,

$$\chi^2 = \sum_{pixels} \left(\frac{C_{l,m} - S_{dec}(x'_m, y'_l)}{\Delta_{m,l}}\right)^2 \tag{4.8}$$

where $C_{m,l}$ are the pixel counts, S_{dec} the deconvolved surface brightness model and $\Delta_{m,l}$ weight factors, that depend on photometric and systematic errors.
The MGE modelling was significantly simplified for the user with Cappellaris IDL routine. The routine is based on the following concept:

- Locate the galaxy's position and determine its orientation and ellipticity using weighted first and second moments of the intensity distribution
- Measure the photometry along sectors, that are spaced logarithmically in radius and linearly in angle
- Fitting the MGE model to the measured image photometry

Having found a proper MGE parametrisation for the surface brightness profile of a particular galaxy, the total mass density ρ can be described by

$$\rho(R,\theta) = \sum_{j=1}^{N} \frac{(M/L)_j L_j}{(\sqrt{2\pi}\sigma'_j)^3 q'_j} exp\left\{-\frac{1}{2\sigma_j'^2}\left(x_j'^2 + \frac{y_j'^2}{q_j'^2}\right)\right\} \tag{4.9}$$

where $(M/L)_j$ denotes the mass-to-light ratio that can be different for the different components. In the present thesis, the in this section derived total density will be used to describe the stellar gravitational potential of NGC 4414. Hence, I will explain the performed steps to obtain a proper MGE parametrisation.

At first I ran the MGE fit on the dust-corrected and uncorrected SDSS image to check the effectiveness of the dust correction. The MGE fitting revealed that the dust-correction is not essential for the parametrization of the surface brightness of NGC 4414. This can be explained with symmetry reasons. NGC 4414 is inclined in a way, that one side is facing towards us. On this side, more dust obscures the light than on the other side. An asymmetric dust-distribution along the field-of-view is presented. On the other hand, the MGE model measures the photometry of the image symmetrically. Therefore, due to the symmetric

photometry modelling, an indirect dust-correction is performed.

Intending to combine large field-of-view data with high resolution data, the idea was to run the MGE routine on the SDSS and HST image simultaneously. This involved a few prior steps. The first part was the determination of the HST WFPC2/F6060W PSF, that has to be

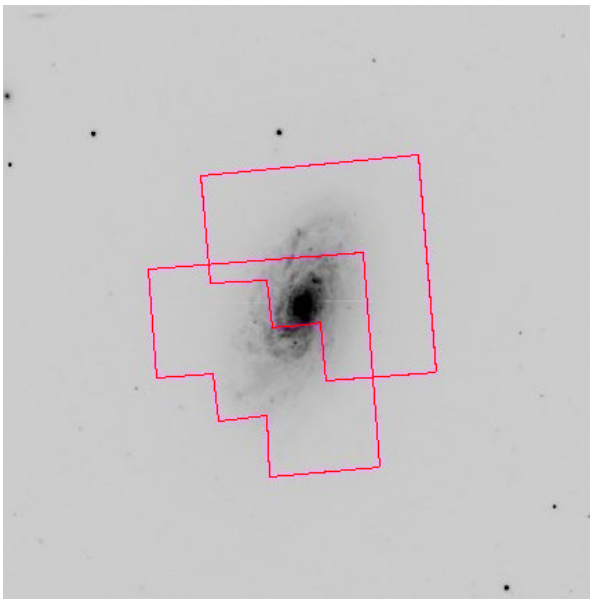

Figure 4.3: *Comparison of SDSS and HST Wide-field Camera. The image shows an extract of the SDSS R-band mosaic. The SDSS mosaic is scaled to* 0.1×0.1 *square degrees. Overplotted are the footprints of the two HST Wide-field and the small Planetary Camera images. The WF images cover a field of view of* $2.5' \times 2.5'$ *in a rotated L-shape.*

convolved with the galaxy model. Therefore, I created a model of the HST WFPC2/F6060W PSF at the coordinates of the center of the galaxy using the Tiny Tim HST PSF Modeling tool (Krist et al. 2001). TinyTim computes instrumental PSFs for an arbitrary place of a chosen HST instrument. Using TinyTim has an advantage over the prior method, as I could compute the PSF directly in the center of my galaxy.
To achieve a parametrization of the PSF, I fitted a circular MGE model of the form

$$PSF_{model}(R') = \sum_{k=1}^{M} I_{*k}/(2\,\pi\sigma_k^{*2})\, exp\{-R'^2/(2\,\sigma_k^{*2})\} \tag{4.10}$$

(Cappellari et al. 2002b), where σ_k^* is the circular dispersion of the PSF and the I_k denote the relative weights of every circle. The relative weights have to be normalized $\sum_{k=1}^{M} I_{*k} = 1$ to ensure the normalization of the PSF. The best-fit is obtained with a non linear least-squares fit by minimizing the residual between the PSF MGE Model and the observed PSF. It turns out that the PSF can be shaped by 5 circular Gaussians with the relative weights and dispersions given in table 4.2 . This PSF has to be convolved with the MGE models, before they can be compared with the real data to select the best-fitting MGE parameters.

During this work, the question developed, whether it would be better to use the HST wide-field camera instead of the SDSS images. Figure 4.3 shows a footprint of the HST images on the SDSS mosaic. In order to compare the coverage of the models of both images, I ran the MGE routine on both images and checked their largest dispersion values. As the dispersion

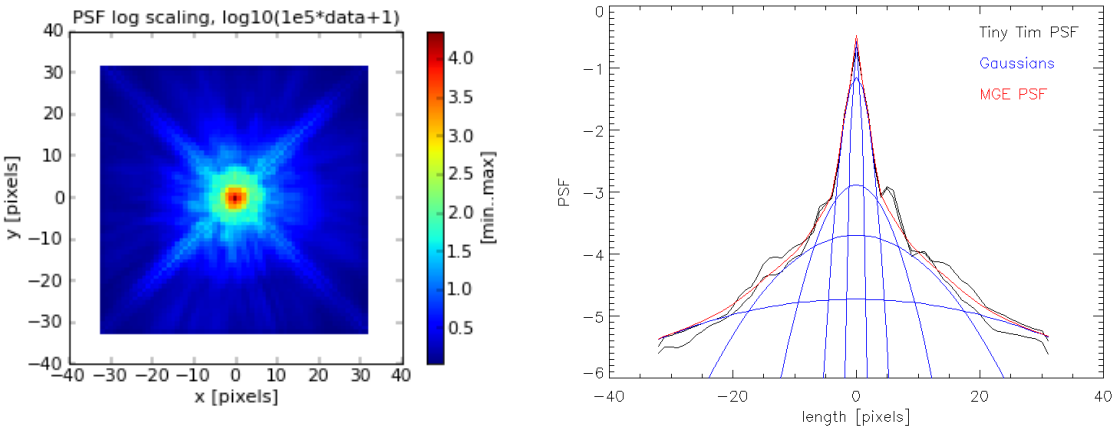

Figure 4.4: *With Tiny Tim tool modelled F606 PC PSF. The right panel shows a cross-section of the PSF. Overplotted is a cross-section of the MGE model and the single Gaussians of the model.*

gives the width of the Gaussians, comparing the dispersions of the furthest Gaussians is an easy and fast check of the model coverage. The test showed that the SDSS Gaussian was slightly more extended. Therefore, I decided to perform the MGE fit simultaneously on the WFPC2/F606W PC1 Chip and the dust-corrected SDSS r-band mosaic, to achieve optimal results at the end.

k	G_k	σ_k^* (arcsec)
1	0.238	0.0173
2	0.569	0.0511
3	0.0842	0.145
4	0.0683	0.334
5	0.0406	0.847

Table 4.2: MGE parameters of the HST/WFPC2/F606PC circular PSF fit

In the next step, the MGE routine was executed on the HST/WFPC2/F606W PC image and the SDSS/r-band image simultaneously to construct the MGE models. Necessarily, the different measured counts had to be normalized. Therefore, I plotted a count profile of both images and aligned the SDSS counts towards the HST counts by comparing the counts in the range of 5 arcsecs (outer part of HST image). The routine works in a way, that for both images the photometry is measured. Afterwards, for the central part the HST photometry and for $R > 5''$ the SDSS photometry is used to fit the MGE model.
The MGE models were constrained by keeping the position angle of the Gaussians constant to produce an axisymmetric MGE model. As described above, this simplifies the JAM modelling technique later.

Figure 4.5 presents the fitting results, the MGE parameters are given in table 4.3.

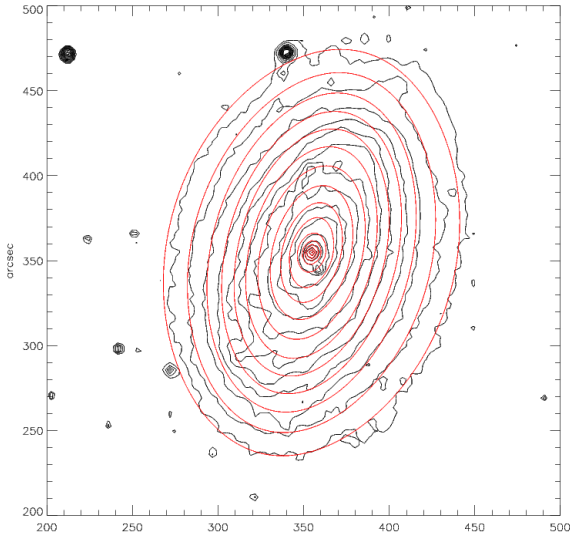

Figure 4.5: *Contour map of the SDSS r-band image of NGC 4414. Overplotted are the elliptical contours of the intrinsic MGE surface brightness convolved with the HST PSF.*

4.6 Photometric results

Table 4.3 shows the parameters that describe the 12 best-fitting Gaussians: N, σ'_j, q'_j. The parameters that are given by the MGE routine have to be converted into physical parameters, before they can be used for dynamical models. The total counts measured for each Gaussian refer to the photometry that was measured on HST PC CCD intensities. The SDSS intensities were rescaled to match to HST, before the fitting was done. Likewise, the radial distance measurements were rescaled to the HST scales of 0.0455 arcec/pixels.
Using the MGE equation and inserting $(x, y) = (0, 0)$ for the central coordinates, the corresponding peak surface brightness N_0 can be expressed by

$$N_0 = \frac{N}{2\pi\sigma'_{j,pixels}q'_j} \tag{4.11}$$

With the next step we move from instrumental counts/pixel units to physical mag/arcsec^2. Using 'standard photometry formulas' the peak surface brightness can be converted to a Johnson-Cousins R-band surface brightness (Holtzman et al. 1995)

$$\mu_R = \mu_{R,0} + 0.1 + 5\,log(scale) + 2.5\,log(t_{exp}) - 2.5\log(C_0) \tag{4.12}$$

where $\mu_{R,0}$ is the photometric zeropoint which is 22.084 for the WFPC/F606W filter, 0.1 is 'a correction for infinite apertures which has to be applied for surface brightness measurements' (Cappellari 2002c), and t_{exp} is the exposure time. The surface brightness in magnitude units is related to the surface brightness in physical units of solar luminosity per square arcseconds by using

$$I'_j = \left(\frac{64800}{\pi}\right)^2 10^{0.4\,(M_{\odot,R}-\mu_R)} \tag{4.13}$$

with the absolute magnitude for the sun in R-band $M_{\odot,R} = 4.42$ (Binney & Merrifield 1998). Equation 4.13 is derived by using the assumption of constant specific intensity along a ray. This means that the surface brightness and surface density are independent of distance. The derivation can be found in (Cappellari 2002c). The total luminosity of each Gaussian L_j can

be obtained by multiplying I'_j with $2\pi\sigma'^2_j q'_j$ again.
The results of this conversion for each Gaussian are also presented in table 3.3. The calculated values can be used to deproject the surface density into the intrinsic mass densities.

j	N	σ'_j (Pixels)	I'_j ($L_{\odot,r}pc^{-2}$)	σ'_j (arcsec)	q'_j	L_j ($\times 10^9 L_{\odot,r}$)
1	26109	1.2	312619	0.0562	0.877	0.047
2	41990	3.1	109287	0.143	0.622	0.074
3	150671	6.0	93365	0.273	0.721	0.267
4	276427	14	35598	0.655	0.6	0.489
5	354717	27	8437	1.25	0.894	0.628
6	966905	63	6010	2.88	0.642	1.706
7	587641	91	1252	4.14	0.91	1.041
8	4117050	299	1229	13.6	0.6	7.271
9	10481600	707	560	32.2	0.6	18.573
10	3413980	1220	61	55.5	0.6	6.01
11	3910550	1635	29	74.4	0.797	0.682
12	275890	2485	0.7	113	1.0	0.477

Table 4.3: MGE parameters for the deconvolved combined HST/SDSS surface brightness of NGC 4414: index of Gaussian j, total counts N, surface density I'_j , dispersion σ'_j, axial ratio q'_j and total luminosity L'_j given for each Gaussian

The quality of the MGE method is deteriorated by a two assumption about the HST PSF. First, the HST PSF deviates significantly from a Gaussian shape and can only approximately be re-produced by the Gaussian expansion. Second, the PSF is only computed for the center of the PC chip. Thus, the convolution does not perfectly reproduce the aperture effects for every image point.
However, the MGE model reproduces the galaxy's shape quite well but appears to be smoother. This is due to the fact that the MGE model does not account for the spiral arms. Here, the main difference can be found between model and HST light profile. This aspect is supported by figure 4.6. The figure shows a comparison of my results with the surface brightness profile of NGC 4414 in the WFPC/F439W B-band taken from Vallejo (2001). The model is in the same order of magnitude as the B-band and shows a similar shape. Deviations can be found between the center and a radius of $60''$ where the spiral arms are located. It is also noticeable that the MGE model has a larger surface brightness along the whole profile. This can be explained by the dependence of the surface brightness on the wavelengths. In the B-band another wavelength range of light is observed than in the WFPC2/F6060W filter. However, the comparison between the different datasets shows that my result is consistent with other studies of NGC 4414.

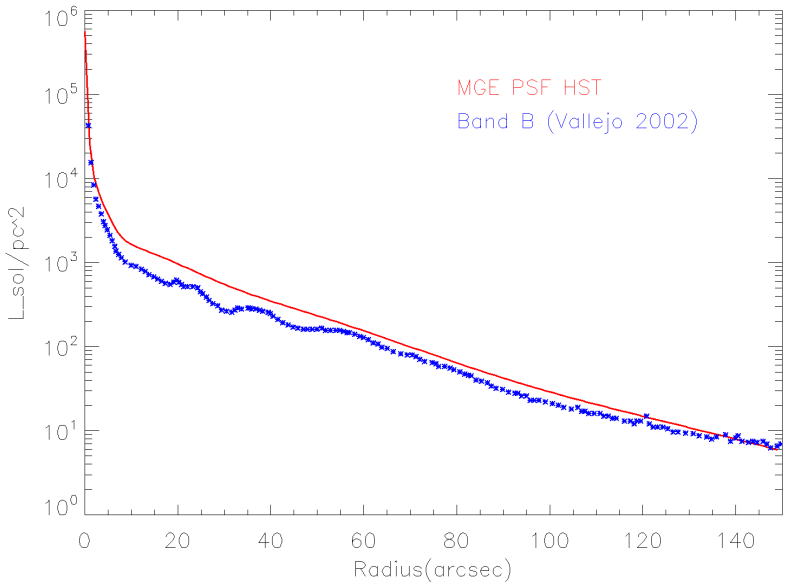

Figure 4.6: *Surface brightness profile of the MGE model compared with the WFPC/F439W B-band HST profile of NGC 4414 which was taken from Vallejo et al.(2002).*

Chapter 5

Extraction of Stellar Kinematics

5.1 Method

In the next part of my thesis kinematical maps of NGC 4414 were extracted from IFS. The stellar kinematic is an important tracer of the SMBH mass as the stars' motion is influenced by the combined gravitational potential affecting them. To explain how the kinematics are derived from stellar light, I will first focus on a single star.
Information about the motion of the star can be obtained from the stellar spectrum in combination with the Doppler shift. When the star moves relative to the observer, the Doppler effect predicts a change in the wavelengths of the light, which is emitted by the star. In a non-relativistic assumption, a projected line-of-sight velocity v_{los} causes a wavelength shift of $\Delta\lambda = \frac{v_{los}}{c}\lambda$. Hence, by measuring the shift of absorption lines with respect to their rest wavelengths, the line-of-sight velocity can be determined.

The spectrum that is observed in a spaxel of the IFS is not produced from the light of one star only, but from the integrated light of all stars which are located along the line-of-sight. The different stars move with different v_{los}. Consequently, the single stellar spectra are shifted with different displacements and the collective spectrum is broadened. Reversed, the widths and center of the absorption lines, which are ideally assumed to be delta-peaked, provide a distribution of stellar velocities along the line-of-sight within a single spaxel. This distribution is known as line-of-sight velocity distribution (LOSVD). By extracting the kinematics from the combined set of spaxels of the IFU, a velocity map of the galaxy can be constructed. Typically, the velocity map shows significant evidence for rotation. When a SMBH is located in the center of the galaxy, we expect to find a rise of the velocity dispersion of the LOSVD towards the center.

In the first approach the LOSVD can be described by a Gaussian. However, the LOSVD is typically not symmetric and is better reproduced by a non-symmetric function. The solution is provided by a Gaussian and a set of Hermite polynomials, commonly referred to as Gauss-Hermite series (van der Marel & Franx 1993; Gerhard et al. 1993). In most cases only the h_3 and h_4 Hermite polynomials are added. The h_3-term models the deviation of the Gaussian from a symmetric form and is called skewness, the h_4 models the pointedness of the Gaussians peak and is called kurtosis. To better visualize the effect of the Hermitian terms on the Gaussian, figure 5.1 shows a grid of different values for h_3 and h_4 and illustrates the Gaussians shape, respectively (Binney & Merrifield 1998)

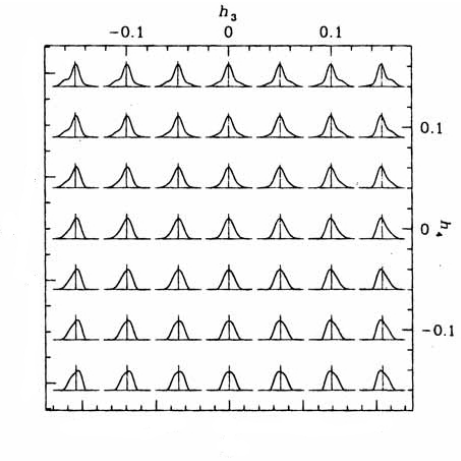

Figure 5.1: *Montage showing the change of the velocity distribution with different Gauss-Hermite parameters h_3 and h_4 (and constant v_{los} and σ_{los}). The central distribution is a pure Gaussian with $h_3 = 0$ and $h_4 = 0$. The figure is taken from Binney & Merrifield: 'Galactic Astronomy'.*

5.2 Spectral Dataset

To extract the kinematics of NGC 4414, I used a set of 23 science frames which were obtained from the NIFS spectrograph on the Gemini Telescope in Hawaii. In order to improve the natural seeing correction, NIFS operates by using adaptive optics with Natural Guide star assisted mode. NIFS operates in the near-infrared K-band with a resolving power of around $R = 5000$ covering a small $3'' \times 3''$ field-of-view. The small NIFS field is directly targeted onto the center of NGC 4414 to obtain a well-resolved view of the motion of the stars which are strongly influenced by the SMBH.

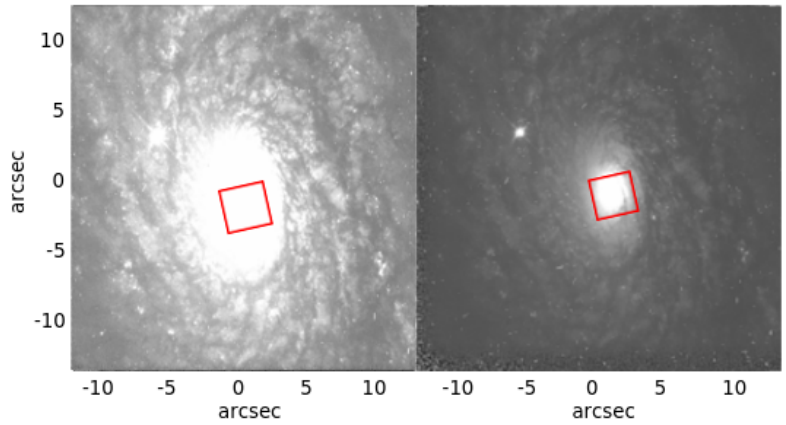

Figure 5.2: *Overplot of the NIFS field-of-view on the WFPC/F606 image. Two grey scales are used to illustrate that the NIFS data only maps the very core of NGC 4414 which is not polluted by dust. The figure is inspired from the NIFS proposal.*

Before one can build the datacubes, the raw files have to be reduced. Image Reduction and Analysis Facility (IRAF) provides the tasks to carry out the reduction and was processed by Davor Krajnović for the NIFS data.

5.3 Merging of NIFS images

For the data analysis, the single science frames are combined into a final data cube to increase the flux of the image and thus increase the Signal-to-Noise (S/N) ratio. The explanation can be connected to direct imaging. Regions of a low S/N can be improved by spatial binning of pixels to catch more signal and enhance the S/N.

The science frame merging was done using a routine in the Interactive Data Language (IDL) that includes re-formatting, re-centering and merging of the science frames. The method was motivated from Krajnović et al.(2009).
Combining the science frames, one has to ensure that they have a common center. This is done by determining the relative shifts of the frames and then re-centering them. For the re-centering, the following steps were performed: at first the single isophotes of the galaxy were plotted and the frame with the best PSF was chosen by eye. The 'best' PSF is determined by a narrow PSF and circular and concentric isophotes in the center. Afterwards, judged by eye, all of the other frames were aligned in respect to this best frame one after another to get the relative shifts. The isophotes could not always be matched perfectly as sometimes the outer isophotes and the inner isophotes were not concentric. This can result from uncertainties in the adaptive optics correction, whereas the inner isophotes are more strongly influenced by the PSF. Otherwise, the outer isophotes contain less flux and are more affected by statistical errors. Therefore, I used a compromise between the geometrically more robust outer isophotes and the more flux significant inner isophotes to deduce the shifts. The accuracy of the shifts is about 1 pixels ($\approx 0.05''$).
Using the determined shifts, all of the frames were re-centered with the IDL routine. Finally, the frames were merged 'with a sigma-clipping pixel reject algorithm 'to create the final data cube. The IDL merging routine first reads in all the re-centered images, 'determines their spatial extent to cover the whole possible field-of-view, defines a new grid of a given pixel size, and interpolates individual frames to this new common grid'(Krajnović et al. 2009). The flux values of the final data cube were obtained as the median value of the single data cubes.

5.4 Voronoi binning of the Spaxels

The higher-order moments of the LOSVD (h_3 & h_4 Gauss-Hermite polynomials) are very sensitive to noise effects. Thus, a high $S/N \geqslant 40$ (van der Marel & Franx 1993, Bender et al. 1994, Statler 1995) is necessary for a reliable measurement of these moments. Whereas the flux is large enough in the central pixels, it drops rapidly towards the outer parts. One possibility to keep a roughly constant high S/N is the Voronnoi adaptive binning technique which was introduced by Cappellari & Copin (2003). Here, adaptive binning refers to the fact that the size of the bins vary according to the local S/N: To maintain a relatively constant signal-to-noise per bin, large spatial bins are created where the S/N is low, while small spatial bins are retained when the S/N is above a critical threshold.
The first bin of the Voronoi binning is obtained by finding the pixel with the largest S/N of the image. From this bin, the S/N centroid is determined and the closest unbinned pixel is selected. With the conditions that the new pixel is adjacent to the bin, the roundness of the bin is conserved and the new S/N is larger than before the addition. The S/N is determined

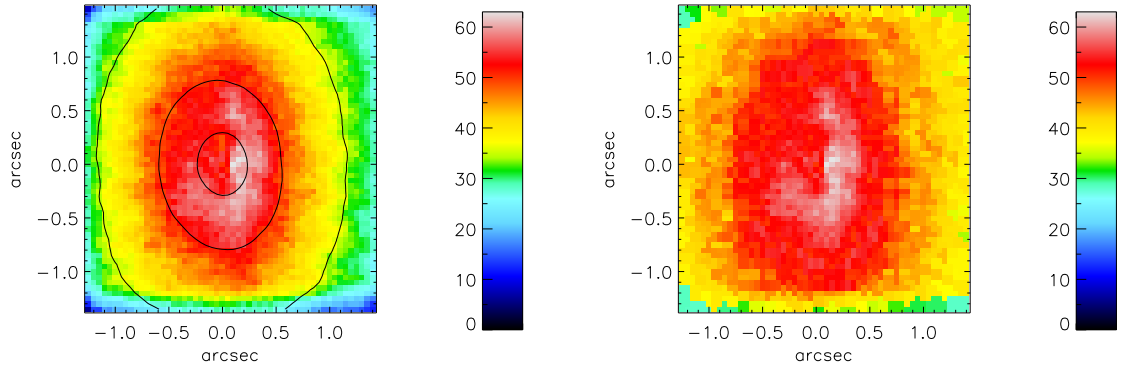

Figure 5.3: *S/N before and after the Voronoi binning.*

using the following:

$$(S/N)_{1+2} = \frac{S_1 + S_2}{\sqrt{N_1^2 + N_2^2}} \tag{5.1}$$

If the new S/N is larger than a fraction of the threshold S/N, the bin is complete and a new bin is started. Otherwise, a new pixel is added to the current bin and the described steps are repeated.

Before performing the Voronoi binning, an initial estimate of the noise of the unbinned spectra is crucial to define the significant S/N threshold. As the data reduction pipeline does not propagate the variance array, I estimated the noise in the following way (Krajnović et al. 2009). Each galaxy spectrum was smoothed over 30 Pixels and then the standard deviation of the residual between the respective galaxy spectrum and the smoothed spectrum is taken. The result can be seen in figure 5.3 . According to this initial S/N estimate, the critical S/N threshold was chosen to be 60 to retain the spatial resolution of the central pixels.
In the following step, using the Voronoi binning method, adjacent pixels were binned together into 1546 bins. Each bin consisted now of a number of spaxels whose single spectra were summed to provide a S/N greater than 60. In a further step, the S/N of every bin was computed again as the standard deviation of the difference between the optimal stellar template and the observed galaxy spectra. In accordance with this, the a posteriori S/N range averaged between 38 and 85. Hence, the Voronoi binning does not provide a $S/N > 60$, resulting into larger uncertainties at the edges of the field-of-view (figure 5.3).

5.5 Penalized Pixel-Fitting

To extract the kinematics from a galaxy's absorption-line spectra I used the Penalized Pixel-fitting (pPXF) method which was developed by Michele Cappellari & Eric Emsellem (2004). pPXF computes the LOSVD in pixelspace and parametrizes the LOSVD with Gauss-Hermite polynomials (Gerhard 1993; Van der Marel & Franx 1993) and an underlying n-th order polynomial continuum. A simplification of the process of 'eliminating the gas emission lines from the fit and taking the continuum matching directly into account'(Bourne 2009) is an advantage of the fitting in pixel space. The breaking idea of the pPXF is to fit the Gauss-Hermite parameters simultaneously, but adding an adjustable penalty term to the χ^2 -Term, 'to bias the solution towards a Gaussian shape, when the higher moments are unconstrained by the

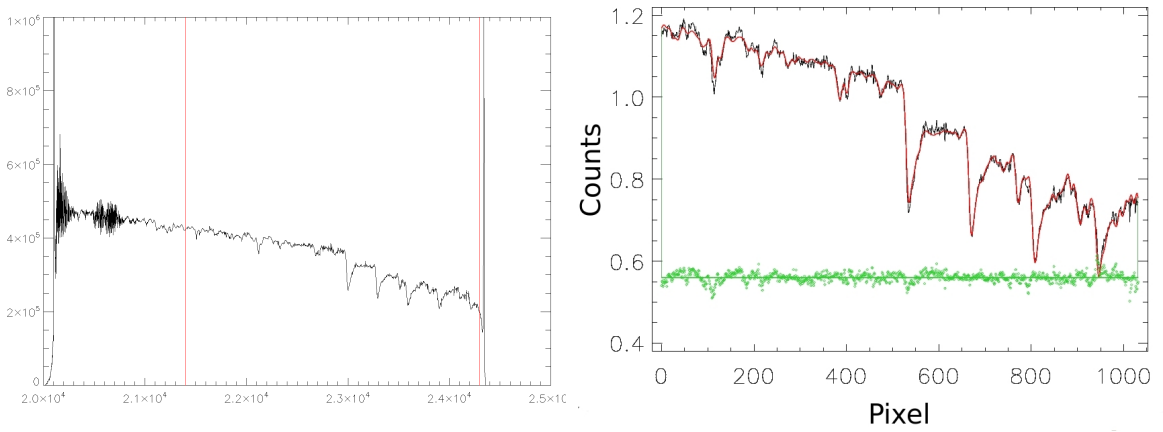

Figure 5.4: *Left panel: Spectrum of the total galaxy. Every spectral bin was created by summing up the single flux values of every spaxel of the given bin. The red lines denote the region that was actually used for the pPXF fitting.Right panel: The four CO lines were used to fit the LOSVD convolved optimal template (red line) to the observed spectrum (black). The residual from the fit is shown in green.*

data' (Cappellari & Emsellem 2004).

The first step of parametrizing the LOSVD in pixel space is to create a model galaxy spectrum $G_{mod}(x)$ and convolve it with a template spectrum T(x) by a parametrized LOSVD. The model galaxy spectrum can be described as:

$$G_{mod}(x) = \sum_{k=1}^{K} w_k [B * T_k](x) + \sum_{l=0}^{L} b_l \mathcal{P}_l(x) \tag{5.2}$$

where T_k is a library of K stellar templates which is colvolved with the broadening function $B(x) = \mathcal{L}(c\,x)$. $\mathcal{L}(v_{los})$ denotes the LOSVD and c is the speed of light. The Legendre polynomials $\mathcal{P}_l$ of the order l provide low frequency differences in the shape between the galaxy and the templates. For each given $\mathcal{L}(v_{los})$ the χ^2 is optimized in a bounded-variables linear least-squares problem of weights $(w_1, ..., w_K; b_0, ..., b_l)$ which can be solved with the BVLS algorithm (Laweson & Hanson 1995). The LOSVD can be expressed by a Gauss-Hermite series (van der Marel & Franx (1993); Gerhard (1993)):

$$\mathcal{L}(v) = \frac{e^{-(1/2)y^2}}{\sigma\sqrt{2\,\pi}} \left[1 + \sum_{m=3}^{M} h_m\, H_m(y) \right] \tag{5.3}$$

where $y = (v - V)/\sigma$ and the H_m are the Hermite polynomials. The optimization of the fit is done by minimizing the penalized χ^2 which is:

$$\chi^2 = \sum_{n=1}^{N} r_n^2 (1 + \lambda^2\, \mathcal{D}^2) \tag{5.4}$$

with the residual

$$r_n = \frac{G_{mod}(x_n) - G(x_n)}{\Delta G(x_n)} \tag{5.5}$$

For further details I would like to refer to Cappellari & Emsellem(2004).

The observed spectrum of a galaxy is the convolution of the integrated spectrum of its stellar population with the instrumental broadening and the LOSVD. Assuming that a galaxy spectrum is a combination of the spectra of single stars, a template was used to fit the significant CO absorption lines of the observed spectrum. The success of the pPXF is strongly dependent on the provision of a good set of template stellar spectra, that match the galaxy spectrum as closely as possible. Therefore, I compared 2 template archives of Winge et al. (2009) with the NGC 4414 galaxy spectrum. One template archive was observed with GNIRS (23 stars), the other with NIFS (31 stars). Both consist of G-, K- and M-stars with spectra centered at 2.2 μm and spectral resolution of around 3.2 $\mathring{A}$. After reducing the data, Winge et al. also corrected the data to rest velocity to make them comparable.

I used pPXF of the single libraries at first and finally combined them to find the best fitting template. For the GNIRS I had to take into account the different FWHMs of the instruments. Therefore, I determined the spectral resolution of my data by fitting 10 characteristic lines of the sky observations and obtained a resolution of 3.2$\mathring{A}$. As GNIRS has a spectral resolution of about 2.9$\mathring{A}$, I had to convolve the GNIRS template with the quadratic difference in resolution to be able to compare it with my data.

With the assumption that the whole galaxy consists of the same stellar population, one can determine an optimal template which will be fitted to each single bin characterizing the stellar population of NGC 4414. To determine this optimal template of a spectrum of the whole galaxy, for every wavelength bin of the spectrum the flux was summed up over all of the spatial pixels. In order to improve the quality of the fit by mitigating the edge effects and avoiding the telluric features, the spectrum was reduced to span a wavelength range between $2.14 \cdot 10^4$ and $2.43 \cdot 10^4$ $\mathring{A}$ focusing on the CO band at 2.29 microns.

To run pPXF robustly, I had to give an initial estimate of the redshift between template and data. The redshift I obtained by measuring the 4 CO spectral lines in my data and in the template spectra and dividing the wavelengths shift by the wavelengths in the stellar template.

$$z = \frac{\Delta\lambda}{\lambda_0} \tag{5.6}$$

Thus, I calculated the redshift between the templates and NGC 4414 to be around $z = 0.0028$, which is consistent with the redshift in the literature $z = 0.0024$ (Rhee et al. 1996).

Spectral line	$NGC4414$ λ (Ang)	$HD108164K2III$ λ (Ang)	$\Delta\lambda$ (Ang)	$Redshift$
CO 1	23001	0.0173	63	.0.00274
CO 2	23295	0.0511	64	0.00276
CO 3	23598	0.145	71	0.00318
CO 4	23900	0.334	65	0.00273

Table 5.1: wavelength, shift and redshift of NGC 4414 NIFS spectrum towards HD108164 K2 III,v2 NIFS spectrum respectively to measure the redshift.

Another step, before running the pPXF, was to create a 'good pixels' mask to cut out the emission lines in the critical wavelength region, as they should not be included in the fit. The emission lines that were taken from Oliva 1990 where they are given at rest-wavelength and multiplied by the estimated redshift of $z = 0.002388$ of NGC 4414 to receive the respective wavelength in the galaxy's rest-frame. It turned out, that there was no critical emission at the predicted spaces, so that I could use pPXF on the whole region between 2.2 and 2.4 μm. The routine found an optimal template to fit the CO spectral lines as combination of the spectra of eight stars. The stars, their spectral type and their relative weights are given in table 5.2.

Name	Spectral Type	Weights	Catalogue
HD 63425B	K7 III	0.291	GNIRS
HD 113538	K8 V	0.24	GNIRS
BD 394208	M3 I ab	0.114	NIFS
HD 339034	K3 I ab	0.101	NIFS
HD 235774	M5 III	0.042	NIFS
HD 64606	G8 V	0.038	GNIRS
BD 59274	M2	0.036	NIFS
HD 30354	M2 III	0.034	NIFS

Table 5.2: Optimal template of the summed spectrum.

The weights determine how dominantly a particular star is affecting the optimal template. The linear combination of the weights and the array of stellar templates results into the optimal template.
It has to be taken into account, that by using one optimal template for the whole galaxy, we are assuming the simplification of having only one stellar population composition in the entire galaxy.
The optimal template is used to fit each spaxel of the data cube in the same wavelength range as for finding the optimal template. Due to the velocity dispersion the single lines are broadened. This is taken into account by convolving the optimal template with the best fitting LOSVD that is computed for each pixel. To the convolution, polynomial terms of the 4th order are added to include the continuum fitting.

5.6 Kinematic maps

Using pPxf with the optimal template on the whole data cube, the rotational velocity, velocity dispersion and the Gauss-Hermite moments could be determined for each bin of the data cube. I also checked every spectra visually for template-mismatch and for the quality of the fitting. During this check I did not find any peculiarities.
The two-dimensional kinematic maps are presented in Figure 5.5 . The first map shows the rotational velocity. The central part of NGC 4414 shows significant and regular rotation. The lower part moves towards us, while the upper part moves away.
The velocity dispersion can be calculated by the width of the spectral lines. In a single bin, two effects make a contribution to the line of sight velocity. Firstly, stars move with different velocities. Secondly, we are only observing the projection of these velocities towards the line of sight. Due to these effects, we measure a variation of velocities distributed around the mean velocity. This variation broadens the spectral lines and is measured in the velocity dispersion. Where the galaxy moves towards and away from us, the dispersion is lowest. At

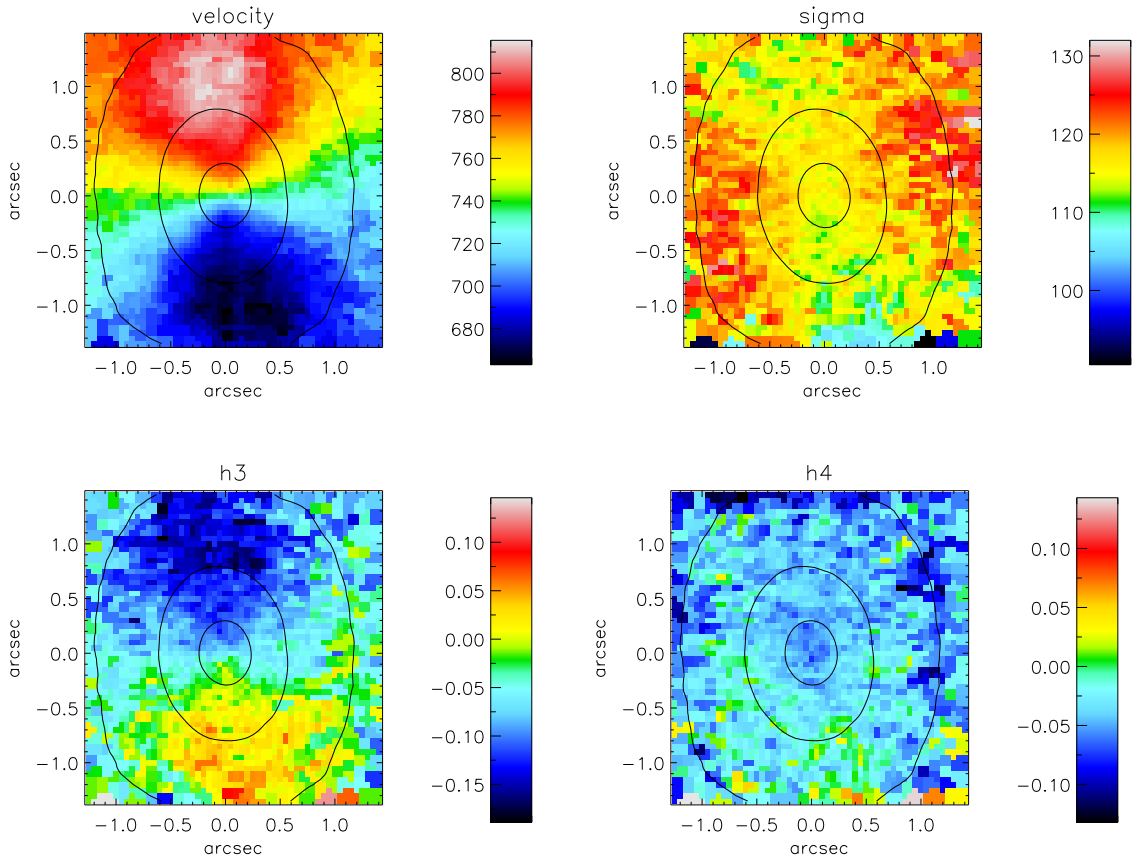

Figure 5.5: *Kinematic maps of NGC 4414 that were extracted from the IR spectra of each bin. From upper left to lower right the rotational velocity, velocity dispersion, h_3 and h_4 Gauss-Hermite polynomials are shown.*

places, where the rotational velocity is orthogonal to the line of sight, the velocity dispersion is the largest.
The third Gauss-Hermite moment h_3, also called skewness, measures the deviation of the Gauss from being symmetric. Is it larger than zero, then the distribution is concentrated on the left, and vice versa. The h_3-map is strongly anti-correlated to the rotational velocity map.
The fourth Gauss-Hermite moment h_4, also called kurtosis, determines in what extend the spectral lines deviate from the Gaussian shape. For $h_4 > 3$, the distribution has a high acuate peak around the mean and broader tails. The h_4-values are generally uniformly distributed over the map and show that for nearly all spaxels the lines deviate in the same way from a Gaussian.

Parameter	Min (km/s)	Max (km/s)
Vel	815.6	663
σ	130.5	68.4
h_3	0.17	-0.19
h_4	0.25	-0.09

Table 5.3: Numerical values for kinematic data

NGC 4414 is kinematically interesting as it does not show a peak in the central v_{rms}. Thus the question evolves whether a BH is present in the center of NGC 4414.

5.7 Determination of Errors

Additional to the kinematic maps, their uncertainties had to be determined. Therefore, Monte-Carlo simulations were used to estimate the errors of the rotational velocity, the velocity dispersion and the hermite coefficients.
The idea is to create modified data sets based on our observed data. All data sets are assumed to be similar to the actual value around which measurements fluctuate. The goal of the simulations is to understand the effect of small variations in the data on the measured parameters. Therefore, small normal distributed noise was generated by taking the standard deviation of the residual from galaxy spectrum and best fitting template. Each pixel of each spectrum was then perturbed by a random fraction between 0 and 1 of the calculate $1\,\sigma$ range. In this way, a new spectrum was created and the kinematics extracted. The method was repeated 100 times for every spaxel and the uncertainty derived from this ensemble of generated measurements. The uncertainty was calculated by taking the standard deviation of the extracted parameters from all 100 simulations for each spaxel.

Figure 5.6 shows the error maps for the different parameters. Typical errors are 3 km/s, 4 km/s, 0.03, 0.03 for V, σ, h_3 and h_4, respectively. The errors are uniformly low, but decrease towards the center. This is natural as the S/N rises towards the center and the noise is assumed to not be systematically. In the lower part of all four panels the noise is large compared to the signal and the uncertainty increased. Therefore, we decided to mask the spaxels having an error in dispersion larger than 10 or an error in central velocity larger than 6 for the construction of the dynamical models.

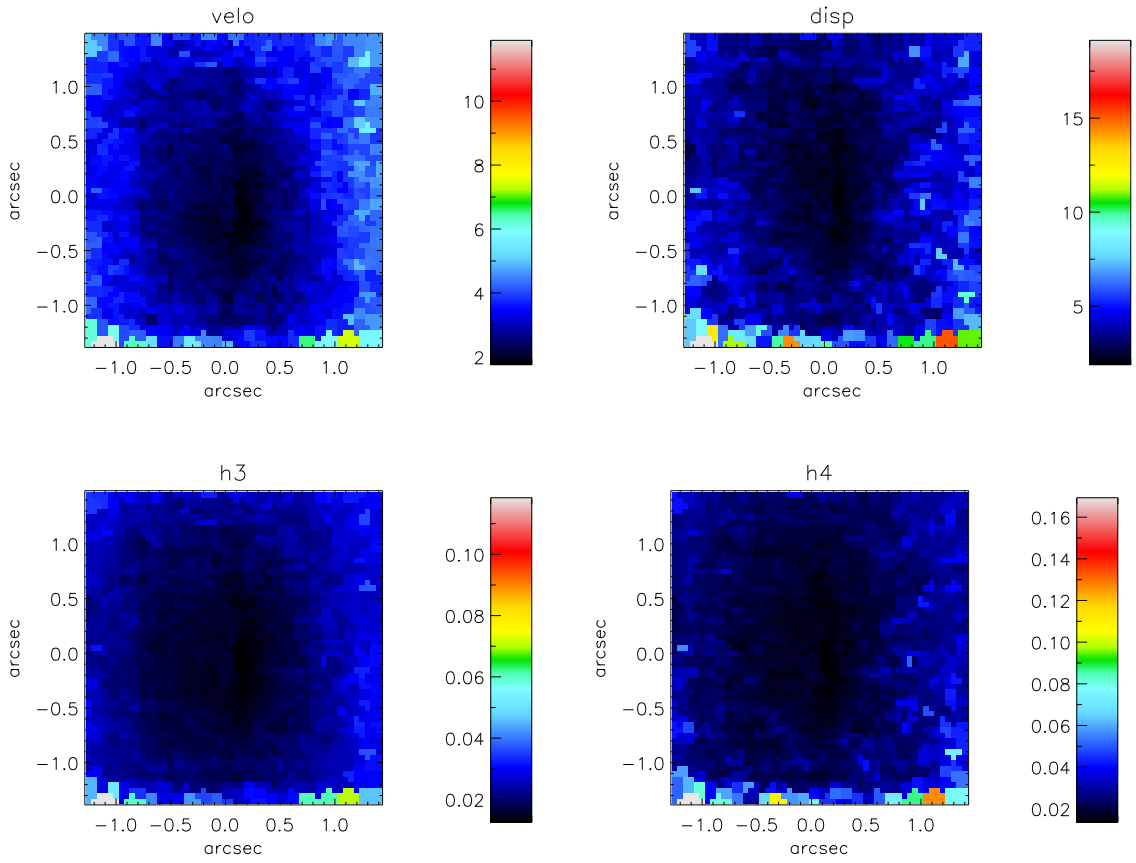

Figure 5.6: *Error maps of NGC 4414 that were generated from the Monte Carlo Simulations. From upper left to lower right the rotational velocity, velocity dispersion, h_3 and h_4 Gauss-Hermite polynomials are shown.*

5.8 Effective spatial resolution

A key parameter to characterize the goodness of the data is the effective spatial resolution of the reconstructed unbinned data cube. A precise measurement is not only important to estimate the seeing conditions during the measurement, which smears the intrinsic light distribution of the galaxy, but also to determine how far the dynamics in the center of the galaxy can be probed. The second is particularly necessary for the construction of the dynamical models.
The spatial resolution of the observations is expressed by the spatial PSF of the reconstructed data frame. It can be determined the PSF by studying the spreading of point sources due to instrumental smearing effects. When no point sources can be found in the field of view, the observed images have to be compared with reference images of better resolution. It is important that the reference image has significantly better resolution to ensure 'that the convoluion kernel dominates the resulting image quality' (Krajnović et al. 2009, Davies 2007). HST is sufficiently qualified, as its instruments provide high-resolution images.

Thus, the intensity profile along the major axis was taken from the reconstructed NIFS

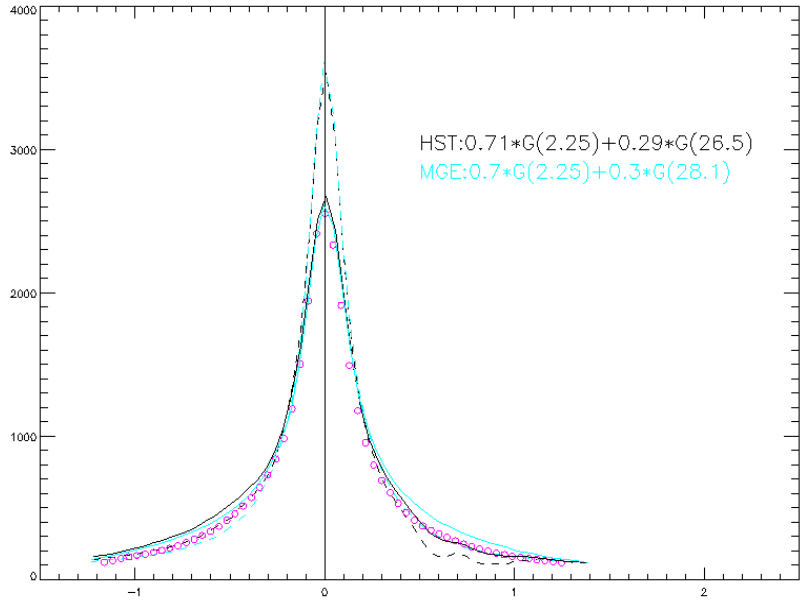

Figure 5.7: *Comparision of the light profils between NIFS and HST images. The profils were determined along the major axis, respectively. The NIFS data is shown as open circles, the HST data is present as direct measurement from the HST image (dashed black line) and the computed MGE model (dashed blue line). Using convolution with appropriate PSFs, the HST and MGE profile were degraded to match the NIFS data. The convolved profils are shown as solid lines.*

image, the HST/WFPC2/F909W PC chip and MGE model. The PSF can be determined by convolving the better-resolved HST profile and degrade it until it matches the NIFS profile. A good description for the PSF can be obtained by a sum of two circular and concentric Gaussians, one having a broad, the other a narrow shape

$$PSF_{NIFS} = w_1 \cdot G(\sigma_1) + w_2 \cdot G(\sigma_2) \tag{5.7}$$

After the convolution, the HST profile was rebinned to the same pixel scale as the NIFS observation. The best fitting PSF parameters are found by minimizing the residual between

the with Gaussians convolved HST image and the NIFS reconstructed image. This procedure was repeated for the MGE profile. The best fitting PSF parameters are presented in table 5.4, respectively.

image	HST	MGE
σ_1	0.11	0.11
σ_2	1.33	1.4
weight$_1$	0.71	0.7

Table 5.4: Parametrisation of the double Gaussian fits to the HST and MGE profil. Given are the dispersions σ of the two Gaussians (in arcseconds) and the relative weight of the first Gaussian.

5.9 Determination of the velocity dispersion σ_e

An approximation for the mass of the SMBH in NGC 4414 can be achieved by inserting the galaxy's bulge velocity dispersion in the $M_{BH} - \sigma$ relation. Measurement for the bulge velocity dispersion can be found in the HyperLeda Catalogue [7]. However, the bulge velocity dispersion can also be extrapolated from the NIFS data. Therefore, it is important to specify how the bulge velocity dispersion is measured. While people used the central velocity dispersion σ_c in the past, Cappellari (2006) defines a proper value for the bulge velocity dispersion as σ_e, the 'luminosity-weighted second moment of the LOSVD within the effective radius R_e'. σ_e has the advantage over σ_c that its dependence on the operated aperture is rather low. In addition, σ_e is only weakly dependent on detailed specifics of the orbital distribution and can thus be used to quantify the $M_{BH} - \sigma$ behaviour of different galaxies.

The NIFS data has the advantage to probe the central regions of NGC 4414 precisely, but unfortunately the limited field of view does not cover the effective radius of NGC 4414 ($R_{e,NGC4414} = 0.1'$ (Thornley 1996)). Consequently, the measured velocity dispersion has to be extrapolated towards σ_e. Cappellari (2006) provides a power-law correction with the form

$$(\sigma_R/\sigma_e) = (R/R_e)^{-0.066\pm0.035} \tag{5.8}$$

where σ_R gives the velocity dispersion at a specific radius.

I measured σ_R from the NIFS data by co-adding all spectra of all spaxels.The resulting spectrum is equals a spectrum that would have been observed with a single aperture of radius $1.5'' \approx 1/4\, R_e$. Using pPXF with the optimal template from section 5.5. (higher Hermite polynoms set to zero) provides $\sigma_{R/4} = 120\,\mathrm{km/s}$. The bulge velocity dispersion can be computed to

$$\sigma_e = \sigma_R \cdot ((\frac{1}{4}R_e/R_e)^{-0.066\pm0.035})^{-1} = 109.5\,\mathrm{km/s} \tag{5.9}$$

This value is in consistent with the velocity dispersion $\sigma_{HL} = 111.4 \pm 3.8$ that can be found in HyperLeda.

[7] atlas.obs-hp/hyperleda/

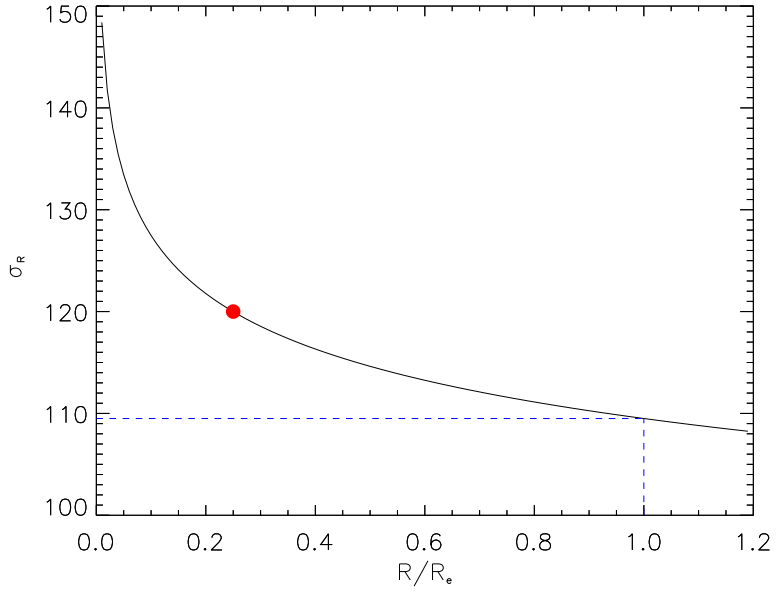

Figure 5.8: *Scheme of the determination of the bulge velocity dispersion at the effective radius R_e by extrapolating the measured velocity dispersion for $R = R_e/4$ (red point). The black line is the power-law relation $\sigma_R \propto R^{-0.066}$ (Cappellari et al. 2006), the dashed lines lead to the value for the bulge velocity dispersion $\sigma_e = 109.5\,km/s$.*

Chapter 6

Application of Stellar Dynamical Models

In this section, the photometric and kinematic results are combined to construct dynamical models to constrain the central potential. In the last 30 years dynamical models of galaxies have expanded from simple spherical models based on the Jeans equations (Binney & Mamon 1982) over axisymmetric Jeans equations towards more general orbit- or particle based numerical techniques with spherical (Richstone & Tremaine 1984),axisymmetric (van der Marel et al. 1998) or triaxial geometry (Van den Bosch et al. 2008). The numerical orbit superposition method (Schwarzschild 1979) is currently the standard for most M_{BH} determinations from stellar kinematics (van der Marel 1998, Gebhardth 2003, Valluri 2005).
While the more general Schwarzschild models are very sensitive to 'numerical implementation details and due to their complexity very difficult to test thoroughly' (Cappellari 2009) the Jeans equations can generally be solved and tested to machine precision' (Cappellari et al. 2009). The best constraints of the central mass can be found by modelling a galaxy with both Jeans and Schwarzschild modelling.
In this chapter, I use the less complex Jeans models to achieve a model for the potential of NGC 4414. Before constructing the model, I will give a theoretical description and derivation of the Jeans equations which are fundamental for the Jeans models.

6.1 Jeans Equations

6.1.1 Collisionless Boltzmann equation

In classical mechanics the trajectory of every individual particle is described by its equations of motion. Using the equation of motion a future state at any later time can be inferred from a given initial state. However, in a multiple particle system like a galaxy it is not possible to track the trajectory of every star. A statistical description of the whole system comes in very handy.

One can find a good analogy to the formalism used in statistical thermodynamics to describe the thermal behaviour of multiple particle systems. Both, in statistical thermodynamics and in statistical mechanics of stellar systems it is common to characterize the multiple particle system by a distribution function (DF)

$$f(\vec{x},\vec{v},t)\,\Delta x\Delta y\Delta z\Delta v_x\Delta v_y\Delta v_z \tag{6.1}$$

which states the number of stars or particles being found in a given infinitesimal volume and velocity element in phase space at a given time. Granted that the DF is known, the number density of stars at the spatial position $\vec{x}$

$$n(\vec{x},t) = \int\int\int dv_x dv_y dv_z \, f(\vec{x},\vec{v},t) \tag{6.2}$$

as well as the average value of the stellar velocities and the stellar velocity dispersion can be calculated from the stochastic velocity moments of the DF.

It is our ambition now to to find a link between changes in the DF and the gravitational potential of the galaxy $\Phi(\vec{x},t)$ that influences the stars' motion namely, the Collisionless Boltzmann equation. Therefore, we will study the motion of stars in an explicit volume of the phase space. The following section outlines the derivation of the Collisionless Boltzmann equation (CBE) extending to the derivation of the Jeans equations presented by Sparke & Gallagher (2007)[8] and Binney & Tremaine (1987)[9] to which I want to refer for a further and more detailed analysis.

Under the assumption that the total number of stars is conserved, which means that they are neither generated nor destroyed, the change in the number of stars within a volume element occurs due to inflow and outflow only.
In the case that stars move only in one direction the translation of the stars in the position

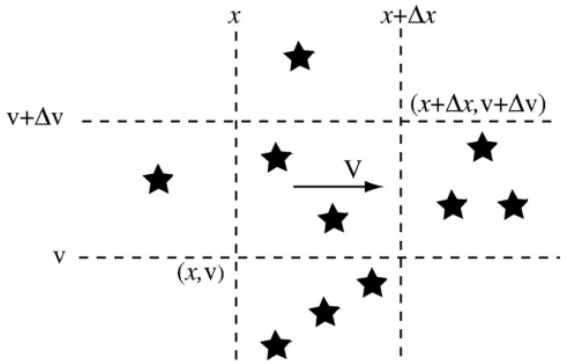

Figure 6.1: *Number conservation of stars in a rectangular volume located in the 2d-phase space. The volume has the physical dimensions of* $[x, x+\Delta x]$ *and* $[y, y+\Delta y]$*. The figure was taken from Sparke & Gallagher: 'Galaxies in the Universe'.*

space can be described by the equation of continuity

$$\frac{\partial n(x,t)}{\partial t} + v(x)\,\frac{\partial n(x,t)}{\partial x} = 0 \tag{6.3}$$

where n(x,t) denotes the number density of the stars which are moving with the speed v(x).

The prior analysis still does not include the gravitational potential Φ. This is where the CBE comes into play. The CBE is very similar to the equation of continuity, but it also considers external forces acting on individual stars, such as the gravitational potential. Before formally introducing the CBE, its most important condition has to be further elaborated; the

[8] L.S. Sparke & J.S. Gallagher, 2007, Galaxies in the Universe (Cambridge University Press), Section 3.4
[9] J. Binney & S. Tremaine, 1987, Galactic Dynamics (Princeton University Press), Section 4.4

system must be 'collisionless' without any significant two-body interactions between bodies.

The time needed to change a body's velocity substantially due to two-body encounters is defined as the relaxation time of the system. As the relaxation time for galaxies is significantly longer than the age of the universe ($T_{relax} \sim 10^{17} yr$), galaxies can be approximated as collisionless systems (Binney & Tremaine 1987). This means that the age of the universe is too short for stars to become aware of each other. In conclusion, the acceleration of each star depends only on the combined gravitational potential of all the other stars.

$$\frac{d\vec{v}}{dt} = -\nabla\Phi(\vec{x}, t) \tag{6.4}$$

Indeed, collisional systems also exist in astronomical scales. For instance, globular clusters are collisional over the lifespan of the universe.

Now let us return to the phase space to derive the CBE. Figure 6.1 is a visualization of a volume element of the phase space in 2 dimensions. Our center of consideration is the number of stars in the central rectangle which lie between $[x, x + \Delta x]$ and move with speeds between $[v, v + \Delta v]$. It has to be noted that speed and position are independent variables. In this case the number of stars can change for two reasons:

- the inflowing or outflowing movement of the stars $\frac{\partial f(x,v,t)}{\partial t} = -v \frac{\partial f(x,v,t)}{\partial x}$
- the acceleration of the movement of the stars $\frac{\partial f(x,v,t)}{\partial t} = -\frac{dv}{dt} \frac{\partial f(x,v,t)}{\partial v}$

Thus, the one-dimensional collisionless Boltzmann equation provides the link between the DF $f(x, v, t)$ and the gravitational potential $\Phi(x, t)$

$$\frac{\partial f}{\partial t} + v\frac{\partial f}{\partial x} + \underbrace{\frac{dv}{dt}}_{-\partial\Phi(x,t)/\partial x} \frac{\partial f}{\partial v} = 0 \tag{6.5}$$

In 3 dimensions the CBE holds the form

$$\frac{\partial f(\vec{x}, \vec{v}, t)}{\partial t} + \vec{v} \cdot \nabla f(\vec{x}, \vec{v}, t) - \nabla\Phi(\vec{x}, t)\frac{f(\vec{x}, \vec{v}, t)}{\partial \vec{v}} = 0 \tag{6.6}$$

and is called the 'fundamental equation of stellar dynamics'. As mentioned above, the CBE can only be applied to systems where stars neither develop nor vanish. The change in position or velocity has to happen adaptive to the smooth potential. In the case of close 2-body encounters this smoothness is disturbed and an extra collisional term has to be added to the equation.

$\Phi(\vec{x}, t)$ is associated with the total mass density ρ via the Possion equation

$$\nabla^2\Phi(\vec{x}, t) = 4\pi G\rho(\vec{x}, t) \tag{6.7}$$

Within the total mass density the integrated mass of every gravitational system is combined. These are stellar mass, SMBH mass and DM mass.

Retrospective, it was shown that a stellar system can be described like a fluid. However, while a conventional fluid is determined by two-body interactions, stellar dynamics are governed by the interaction between single stars and the combined gravitational potential of the other stars within the galaxy.

6.1.2 Orbits of stars in galaxies

Stellar trajectories are commonly referred to as orbits. Stellar orbits in galaxies differ from Keplerian orbits, such as planetary orbits in the solar system, in being very complex, 3-dimensional and usually not closed paths. Even if the galaxy is in equilibrium, the orbits can be highly chaotic. Stellar orbits are influenced by the potential in which they are inbedded. Simple potentials can be generated by varying their axial symmetries. In the following, a, b and c denote the lengths of the principal axes that are perpendicular to each other.

- The simplest case is the stellar orbit in a spherical potential (a=b=c). The star stays in a rosette-shaped open orbit perpendicular to the angular momentum vector of the star.

- The axisymmetric potential (a = b ≠ c) has cylindrical symmetry like a disk galaxy. The stellar orbit lies in a plane that precesses about the axis of symmetry.

- The third and most complex case is the triaxial potential(a ≠ b ≠ c). Triaxial stellar orbits have the tendency to tumble about one axis which can lead to very chaotic motions.

6.1.3 Jeans equations

In section 6.1.1 an expression for the CBE was given. However, the CBE is a partial differential equation with the DF being a function of 6 variables. As the solution for the DF is very ambiguous, it's evaluation is difficult to handle. For the purpose of a practical application of the CBE, further assumptions and simplifications have to be adopted.

Yet another problem to determine the DF arises from the observations. In most cases it is very challenging if not impossible to obtain the distribution of stars for all six coordinates in phase space, in particular for the velocities. While the velocity component along the line of sight is generally measurable by spectroscopically determining the Doppler shift, the transverse velocity components cannot directly be resolved. On the other hand, the spatial components are only measurable as projected plane in the sky.
Therefore, it is more appropriate to use quantities that are inferred from the DF instead; namely the stellar number density n, the mean velocities $\langle v_{los} \rangle$ along the line of sight and the second moment of velocity. These are the 0., 1. and 2.velocity moments of the DF.

- 0.velocity moment: number density of stars

$$n(\vec{x}) = \int\int\int dv_x dv_y dv_z \, f(\vec{x}, \vec{v}) \tag{6.8}$$

- 1.velocity moment: mean stellar velocity

$$\langle v_i(\vec{x}) \rangle = \frac{1}{n} \int\int\int dv_x dv_y dv_z \, v_i \, f(\vec{x}, \vec{v}), \quad i = 1, 2, 3 \tag{6.9}$$

- 2.velocity moment

$$\langle \, v_i(\vec{x}) v_j(\vec{x}) \rangle = \frac{1}{n} \int\int\int dv_x dv_y dv_z \, v_i v_j \, f(\vec{x}, \vec{v}), \quad j = 1, 2, 3 \tag{6.10}$$

The stellar number density n can be obtained from the observed intensity of light and described, for instance, by the MGE parametrization (chapter 3). The intrinsic luminosity density (in 3d) can be derived by deprojection, which is, unfortunately, ambiguous unless the axisymmetric galaxy is orientated edge-on. The mean velocities and the velocity dispersion are achieved spectroscopically along the line of sight (chapter 4). They can be considered a good approximation for the first two velocity moments (Cappellari et al. 2008).
Hence, as observations provide the number density, the mean velocities and the velocity dispersion of stars it is more convenient to calculate quantities that involve the velocity moments from the DF. The theoretical calculated quantities can then directly be compared with the observations.

The appropriate formalism which relates the number densities, mean velocities, velocity dispersions and the gravitational potential is described by the so called Jeans equations (JE) (Jeans 1915). The JE are derived by taking the velocity moments of the CBE. For instance, to derive the first JE, the CBE is inserted in the 0th velocity moment.

$$\int \left(\frac{\partial f}{\partial t} + \vec{v} \nabla f - \nabla \Phi \frac{\partial f}{\partial \vec{v}} \right) d^3\vec{v} = 0 \tag{6.11}$$

Looking complicated at the first view, the single terms can be simplified as the integration is performed over all positions and velocities. Using Gauss's theorem, the third term transforms to a surface integral and becomes 0. The second term can be integrated with integrations by parts and the first JE stands there. The second JE can be derived from the first velocity moment of the CBE.

1. Jeans equation (continuity equation)

$$\frac{\partial n}{\partial t} + \nabla \cdot (n \langle v \rangle) = 0 \tag{6.12}$$

2. Jeans equation ($\approx$ Euler equation)

$$\frac{\partial (n \langle v_i \rangle)}{\partial t} + \sum_{j=1}^{3} \frac{\partial}{\partial x_j} (n \langle v_i v_j \rangle) = -\frac{\partial \Phi}{\partial x_i} n \tag{6.13}$$

3. Jeans equation

$$n \frac{\partial \langle v_i \rangle}{\partial t} + n \sum_{j=1}^{3} \langle v_j \rangle \frac{\partial \langle v_i \rangle}{\partial x_j} = -n \frac{\partial \Phi}{\partial x_i} - \sum_{j=1}^{3} \frac{\partial}{\partial x_j} (n \sigma_{ij}^2) \tag{6.14}$$

with the tensor velocity dispersion $\sigma_{ij}^2 = \langle v_i \, v_j \rangle - \langle v_i \rangle \langle v_j \rangle$ that denotes the spread of the velocities in all directions, the indices i and j are components of the velocity. The velocity moments are present in the notation

$$n \langle v_i v_j \rangle \equiv \int dv_x dv_y dv_z v_k v_j f \tag{6.15}$$

The third JE is an alternative expression for the second JE. The analogy between stellar dynamics and fluid dynamics is also present in the Jeans equations.

Additional assumptions for the JE can be made to further simpliy the equations. When the potential does not vary with time, the system is in a steady state and the first term

becomes zero $\partial/\partial t = 0$. Further simplifications can be applied due to the system's geometry. For the majority of early type galaxies axisymmetry seems to be an adequate assumption, while for a minority of early type galaxies triaxial shape is more appropriate (Krajnovic et al. 2011). Conversions and evaluations for different potentials can be found in Binney & Tremaine (1987).
Additional assumptions are the alignment of the velocity dispersion ellipsoid with the cylindrical coordinate system (R, z, θ) and constance of anisotropy (Cappellari et al. 2007, Cappellari 2008).

6.2 The anisotropy parameter β

One approach to solve the combination of Jeans equations and Poisson equation uniquely is to assume anisotropy in the velocities. The velocity anisotropy is linked to the velocity ellipsoid. The three axes of the velocity ellipsoid are matched with the velocity dispersions in three independent directions. Axisymmetric galaxies can be described with cylindrical coordinates (σ_R,σ_z, σ_ϕ for velocity dispersions). In oblate systems like NGC 4414 $\sigma_R = \sigma_\phi$ is applied, leaving only two independent axes of the velocity ellipsoid. The ratio of the two independent axes is described by the anisotropy parameter β.

β is defined as the ratio between the axis of the velocity ellipsoid in the radial and vertical directions, which can be related to the motions of stars in radial and tangential orbits:

$$\beta = 1 - \frac{\langle v_z^2 \rangle}{\langle v_R^2 \rangle} \tag{6.16}$$

The anisotropy parameter can be plugged into the Jeans equation to further reduce and constrain it.

Three orbit states are generally distinguised by the anisotropy parameter. Predominantly radial and tangential orbits are sketched in figure 6.2.

- Isotropic ($\langle v_z^2 \rangle = \langle v_R^2 \rangle$) $\quad \Rightarrow \quad \beta = 0$
- Tangential anisotropic ($\langle v_z^2 \rangle > \langle v_R^2 \rangle$) $\quad \Rightarrow \quad \beta < 0$
- Radial anisotropic ($\langle v_z^2 \rangle < \langle v_R^2 \rangle$) $\quad \Rightarrow \quad 1 > \beta > 0$

It is worth noting, that the anisotropy parameter characterizes the net motion of an ensemble of orbits. In the case where all orbits are not only eccentric but also spatially in phase, the spread in radial motion becomes negligible ($\langle v_R^2 \rangle \approx 0$) and thus the anisotropy parameter becomes very small. When all orbits proceed essentially in the same direction, the system is said to be 'rotationally supported'. This generally accounts for disk galaxies. In contrast stands 'pressure supported' for elliptical galaxies. At each spatial point, orbits deviate in all tangential directions. The internal dynamics becomes interesting for ellipses as they appear to be similar shaped, but their kinematics can range from random to systematic stellar motion. The kinematics can be traced back to the dynamical history of the galaxy's stars.

The ratio of tangential orbits and radial orbits affects the observed LOSVD of the stellar component. For predominantly pressure supported systems the LOSVD is flattened, while predominantly rotational supported orbits generate rather peaked LOSVDs. Hence, the

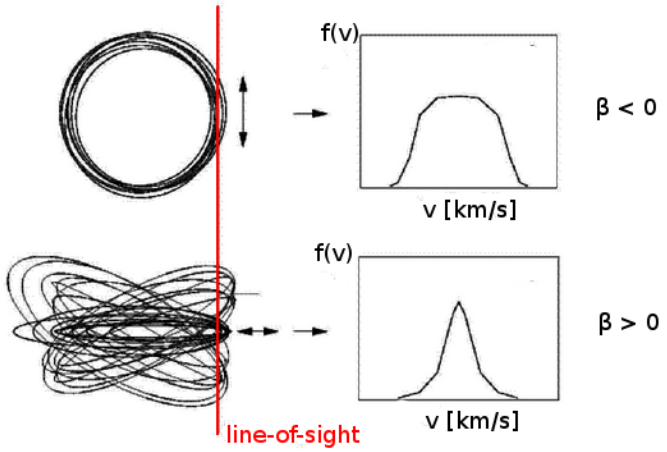

Figure 6.2: *Influence of dominantly radial or tangential orbits on the LOSVD of galaxies. For predominantly tangential orbits (e.g. circles), the LOSVD is flattened ($\beta < 0$), while predominantly radial orbits generate rather peaked LOSVDs ($\beta > 0$). Image is adapted from a lecture from M. Whittle.*

anisotropy parameter is defined by the distribution of stellar velocities within the galaxy. As the different orbits are not easily distinguishable by eye, the anisotropy parameter β is one free parameter in the JAM routine, which predicts the kinematics for the desired galaxy. JAM is further explained in the next section.

6.3 Jeans Anisotropic MGE Modelling (JAM)

To obtain an estimate of the central M_{BH} by constructing a model of the inner dynamics of NGC 4414, I used the Jeans Anisotropic MGE (JAM) package[10] developed by Cappellari. 'JAM allows to compute the predicted second moments, projected onto the 2d-sky plane, for a model with a variable anisotropy profile' (Cappellari 2009).
Spiral galaxies like NGC 4414 do not change their appearance when they are rotated around one of their major axes: They are axial symmetric. Therefore, I used the axisymmetric version of JAM which is based on the formalism given in Cappellari 2008. While I would suggest his paper for a detailed study of JAM, I have outlined a short summary here.
Under the assumption of axial symmetry, which gives $\partial\Phi/\partial\phi = \partial f/\partial\phi = 0$, the JE written in standard cylindrical coordinates (R, z, ϕ) can be modified to

$$\frac{n\langle v_R^2\rangle - n\langle v_\phi^2\rangle}{R} + \frac{\partial n\langle v_R^2\rangle}{\partial R} + \frac{\partial n\langle v_R v_z\rangle}{\partial z} = -n\frac{\partial\Phi}{\partial R} \tag{6.17}$$

$$\frac{n\langle v_R v_z\rangle}{R} + \frac{\partial(n\langle v_z^2\rangle)}{\partial z} + \frac{\partial(n\langle v_R v_z\rangle)}{\partial R} = -n\frac{\partial\Phi}{\partial z} \tag{6.18}$$

These equations can be further reduced by orienting the velocity ellipsoid within the cylindrical coordinate system and a constant anisotropy within the system. The gravitational potential Φ stays on the right side of the equation. As mentioned before, Φ is related to the deprojected surface brightness profile by the Poisson equation. Using the MGE density 4.9 obtained in chapter 4, the gravitational potential is given by the integral (Emsellem et al.

[10] http://www-astro.physics.ox.ac.uk/ mxc/software/

1994)

$$\Phi(R,\theta) = -\sqrt{2/\pi}\, G \int_0^1 \sum_{j=1}^{N} \frac{(M/L)_j L_j H_j(u)}{\sigma_j} du \tag{6.19}$$

where G is the gravitational constant and H_j is expressed as

$$H_j(u) = \frac{exp\left(-\frac{u^2}{2\sigma_j^2}\left[R^2 - \frac{z^2}{1-(1-q_j^2)u^2}\right]\right)}{\sqrt{1-(1-q_j^2)u^2}} \tag{6.20}$$

The equation as it is at the moment only includes the stellar contribution to the potential. However, a black hole central component can simply be included by adding a narrow Gaussian without a visible counterpart in the light distribution to equation 6.17 and 6.18. (Emsellem 1994). The Gaussian is endowed with the mass $M_j = M_{BH}$, the axial ratio $q_j = 1$, the width $3\,\sigma_j < r_{min}$, where r_{min} is the smallest distance from the BH which should be modelled precisely, and with infinite mass-to-light ratio (Cappellari 2008, Emsellem 1994). Hence, we have gotten a description of the left side of equation 1.7, the total central potential of NGC 4414. As mentioned before, the DM component can be neglected. To paraphrase the right-hand side, the kinematics of the stellar tracer, the JE have to be examined more closely. Substituting the MGE description of the luminosity density and the BH into the axisymmetric JE, the integral can be calculated analytically.

Thus, JAM provides a model for the observed galaxy. However, the model is of no avail unless its quantities can be compared with observations. An integration of the second velocity moment along the line-of-sight projects the model kinematics on the solely observable axis. The elaborated final expression of the line-of-sight integral over all of the Gaussian components $\langle v_{los}^2 \rangle$ results in equation (30) of Cappellari (2008). It can be well constrained by the anisotropy parameter β. The calculated second velocity moment along the line of sight shows a good approximation to the observable quantity

$$V_{rms} = \sqrt{V^2 + \sigma^2} \tag{6.21}$$

where V is the stellar mean velocity and σ the velocity which parametrise the LOSVD. These are the quantities that are achieved in the kinematical analysis in chapter 4. The simplicity of the model is noticeable at this point as the LOSVD is not described by Gauss-Hermite polynomials.

Based on the computed MGE surface brightness I constructed several axisymmetric models. The models have three free parameters which are: (1) the anisotropy parameter β, (2) the mass of the SMBH M_{BH} and (3) the dynamical mass-to-light ratio M/L. For my dynamical models I assumed a constant mass-to-light ratio, which is a good approximation in the central regions of NGC 4414, where dark matter is expected to contribute only a small fraction of the mass (Vallejo 2002).
Before identifying the remaining parameters of the best fitting model, I had to set limits for the parameters. The anisotropy parameter β can take a value between $[-\infty, 1]$. For instance, in Capellari (2010) β is constrained to be around [0.05,0.2]. A reasonable value for the mass of the BH can be obtained from the $M_{BH} - \sigma$ correlation which was described in chapter 1.1.3. Inserting the measured velocity dispersion at the effective radius from chapter 5.9 into equation 1.4 yields an approximated value of $M_{BH} = 7.2 \times 10^6 M_\odot$. Hence, I created a 2-dimensional parameter grid with the given parameter ranges, ran JAM on these parameters

and tested the goodness of the different models. As additional quantity, I had to provide the JAM script with the distance to NGC 4414, which has already been used before.

The JAM script now works as follows. For each Voronoi bin of the observation the model prediction for $\langle v_{los}^2 \rangle^2$ based on the given parameter set is calculated. The best fitting mass-to-light ratio can be obtained from a scaling relation $M/L \propto \langle v_{los}^2 \rangle$ as a linear least-square fit, respectively (Cappellari 2008).

Chapter 7

Results and Discussion

7.1 Dynamical Results

The Jeans Models were simultaneously fitted to the NIFS kinematics obtained in chapter 5 and the mass distribution obtained by the MGE models in chapter 4. By varying the mass of the black hole M_{BH} and the anisotropy parameter β, I constructed 90 models. Not every individual model is presented in this thesis, instead a representative selection of my set is shown in figure 7.1. The best fitting model could be determined to be $M_{BH} = 0\,M_{\odot}$ and $\beta = 0.27$. Accordingly, the β parameters in the given selection were chosen to be the one of the best fitting model $\beta_{bm} = 0.27$ and $\beta = \beta_{bm} \pm 0.05$. For the BH mass, I have shown the mass of the best fitting model $M_{BH} = 0\,M_{\odot}$, a mass just outside of the $3\,\sigma$ confidence interval (which can be obtained from figure 7.2) and a mass around the expected mass based on the computed velocity dispersion of NGC 4414. In the bottom panel of figure 7.1 the bi-symmetrized $V_{rms} = \sqrt{V^2 + \sigma^2}$ observed with NIFS is shown.
As mentioned in chapter 6.3 the observable V_{rms} is generally a good approximation for the second velocity moment along the line of sight which was calculated in the JAM model. Therefore, the JAM models were compared with the observed V_{rms}. By eye, the best fitting model is not distinguishable as neither of the JAM models reproduce the observations very well. While the observations show a steep drop in the center of the V_{rms}, it cannot qualitatively be reproduced by the JAM model. Visible in figure 7.1 is that larger SMBH masses fail more distinctly to model the drop in the V_{rms} than lower masses. Hence, provided that NGC 4414 harbours a SMBH, its mass is apparently very small.

Figure 7.2 illustrates the determination of the best fitting model parameters by applying a χ^2 criteria between model and observation. The models are aligned along a $\beta - M_{BH}$ grid and plotted as black symbols. While the anisotropy parameters β are horizontally distributed and parallel to the abscissa, the plotted BH model masses follow a diagonal distribution. This is due to the fact, that the galaxy M/L is determined individually for every model. Referring back to equation 1.7 the change in the M/L ratio changes the stellar mass distribution and thus the mass of the model BH. Therefore, different BH masses are determined for the different models. Overplotted on the model grid are the contours of $\Delta\chi^2 = \chi^2 - \chi^2_{min}$ which describes the agreement between the JAM models and the kinematical NIFS observations. The χ^2 is calculated by

$$\chi^2 = \sum_{array} ((V_{rms} - V_{rms,model})/Error_{rms})^2 \tag{7.1}$$

and represents the deviation between the kinematic data and the model. $Error_{rms}$ denotes the combined errors of rotational velocity V and velocity dispersion σ which were determined

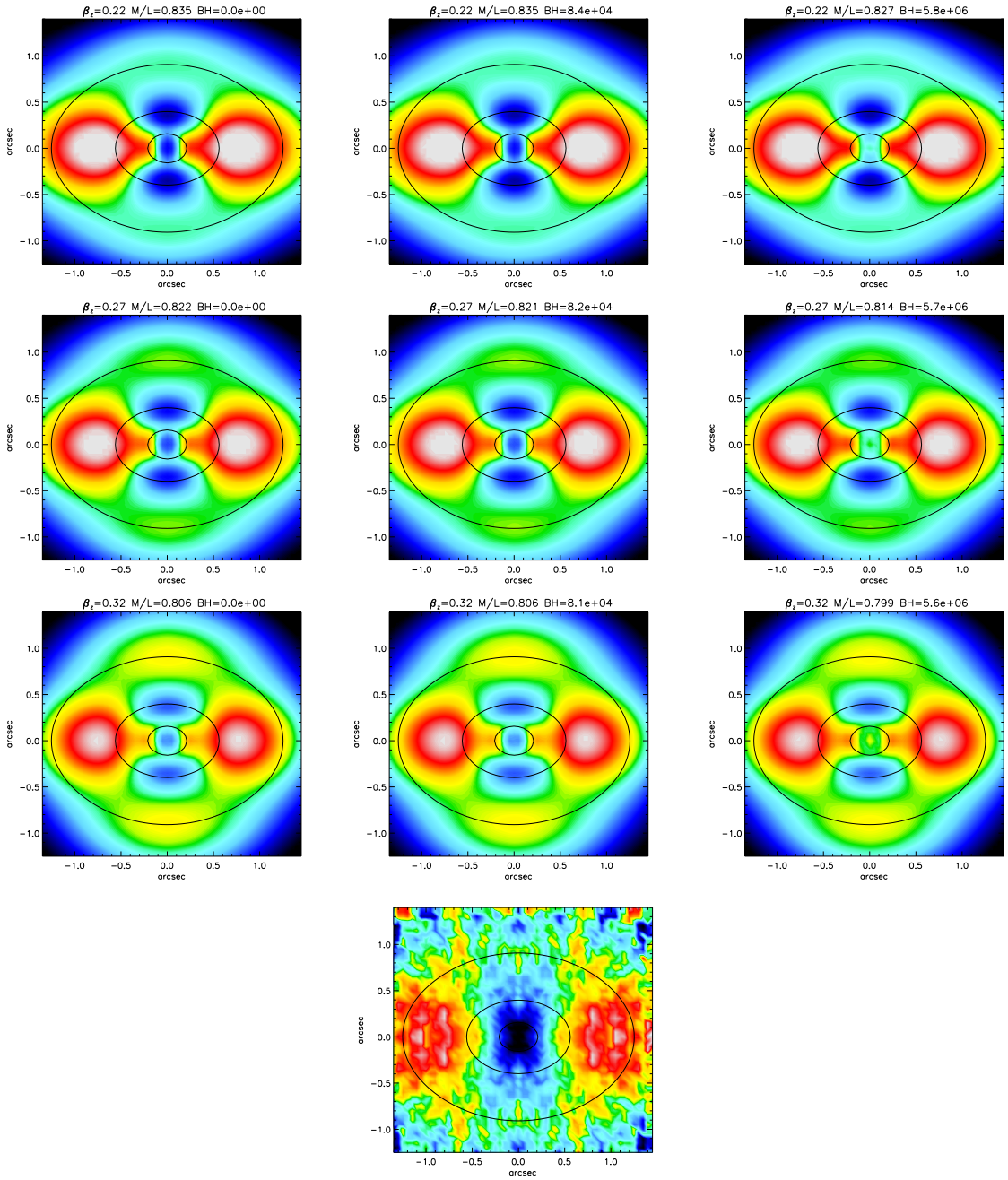

Figure 7.1: Visual comparison between the kinematic data and JAM models for different parameters sets of the mass of the central SMBH M_{BH} and the anisotropy parameter β. The anisotropy parameters are chosen to be 0.22, 0.27 & 0.32, the BH masses $0\,M_\odot$, $10^5\,M_\odot$ & $7 \cdot 10^6\,M_\odot$, whereas each is multiplied with the M/L. The bottom panel shows the bi-symmetrized $V_{rms} = \sqrt{V^2 + \sigma^2}$ observed with NIFS. The best fit model is for $\beta = 0.27$ and $M_{BH} = 0\,M_\odot$. The models do not reproduce the NIFS data well.

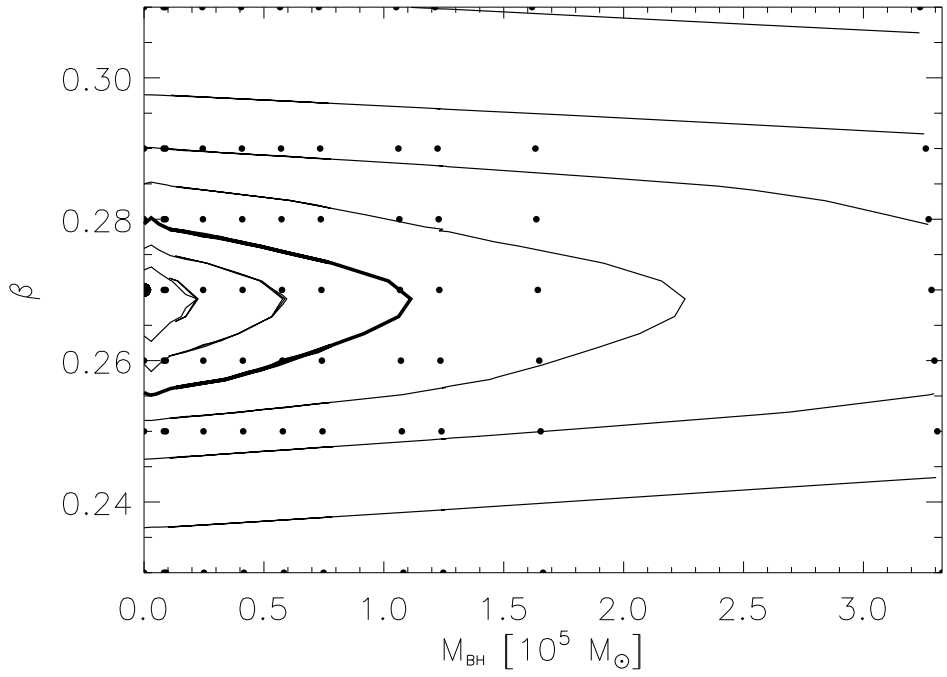

Figure 7.2: Contour plot of χ^2 to compare the agreement between JAM model and V_{rms} data. In the different JAM models, the anisotropy parameter β and the mass of the SMBH M_{BH} are varied. Each black dot denotes a constructed model. The $\Delta\chi^2 = \chi^2 - \chi^2_{min}$ contours were interpolated with a thin-plate spline between these models and smoothed. The three lowest contours correspond to the 1, 2 and 3 σ confidence levels. Further contours are shown by a factor of 2. The best fitting model could be found for $M_{BH} = 0$ and $\beta = 0.27$.

in chapter 5.7. The best JAM model was determined by finding the model with the smallest χ^2 and thus, the largest agreement between model and observation.
$\chi^2_{min} \neq 0$ accounts for the calculated χ^2 of the best fitting model and is subtracted from the other models χ^2 to obtain the $\Delta\chi^2$ contours. In order to smoothen the contours they were interpolated with a thin-plate spline. The three bold lined curves towards the center of figure 7.2 indicate the 1 σ (68.5%), 2 σ (90 %) and 3 σ (99 %) confidence levels. It can be seen that the lower limit of the SMBH is not constrained resulting in an upper limit measurement. For the upper limit I used the M_{BH} value of the 3 σ confidence interval which is

$$M_{BH,NGC4414} = 1.1 \times 10^5 M_{sun} \tag{7.2}$$

This value is significantly smaller than $M_{BH} \approx 7.2 \times 10^6 M_{sun}$ which was determined from the MBH_σ correlation in chapter 6.3. This will be further discussed in section 7.2.

In the case that the inclination angle of a galaxy is not well constrained, the uncertainty of the M_{BH} measurement can increase significantly (Schulze 2011). Therefore, I tested the JAM model dependence on the inclination of NGC 4414. NGC 4414 is inclined to the line-of-sight at an angle of $i = 55°$ (Vallejo et al. 2002). However, it is interesting to investigate how the models would change with a larger inclination. Therefore, I ran models on a 2-d grid of (M_{BH}, β) values for its known inclination first, then I changed the inclination towards 89°. It turned out that no change of the determined $M_{BH,NGC4414}$ could be recognized for the different inclinations. Hence, the JAM model prediction is independent of the galaxy's orientation towards the line-of-sight leading to the assumption that the center of NGC 4414 can be considered as spherical symmetric.

Having found an upper limit for NGC 4414, a question evolves in our minds. Why are we unable to further constrain the BH? Reasons can be found promptly. Firstly, a trained eye can already tell from the kinematics that the BH is very small as the velocity dispersion does not rise significantly in the center of the galaxy. The radius of influence does not exceed 0.04 pc as can be calculated from the determined upper limit and $r_{inf} = \frac{G M_{BH}}{\sigma_e^2}$. Hence, the NIFS spectrograph cannot resolve the radius of influence resulting only in an upper limit (chapter 7.3).
Secondly, the M/L and the anisotropy parameter could not be constrained well enough by the small NIFS field of view of $3x3''$. Thirdly, due to their simplicity, using only the v_{rms}, the models do not reproduce the kinematics well.

7.2 Updated $M_{BH} - \sigma$ relation

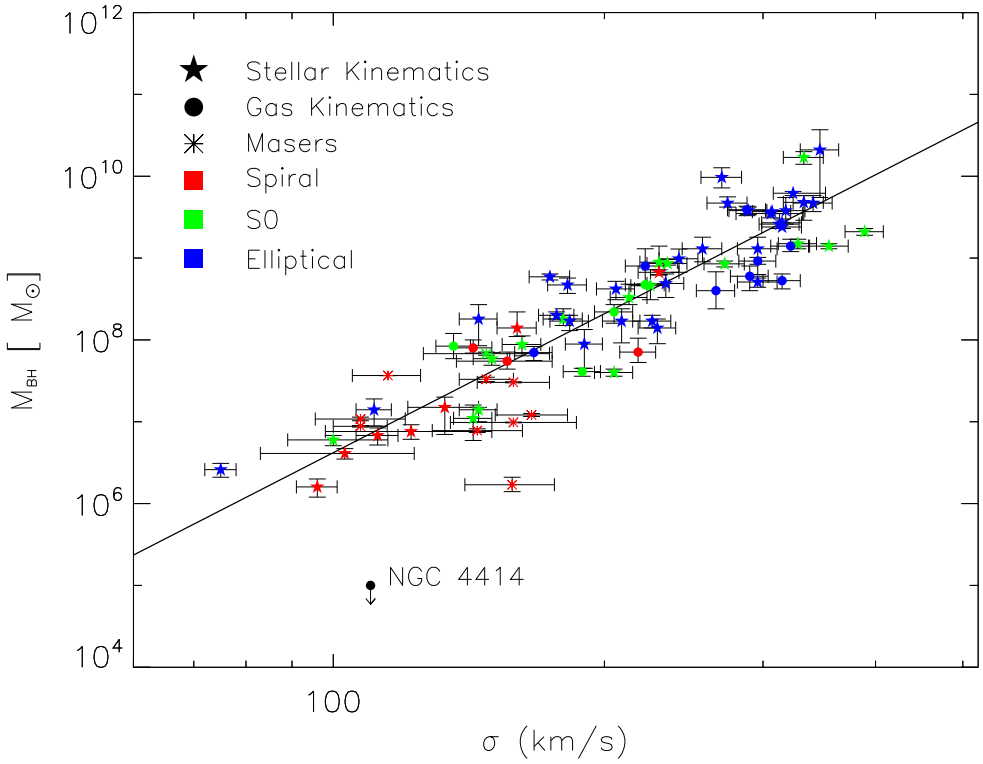

Figure 7.3: *$M_{BH} - \sigma$-relation taken from McConnell & Ma (2013) catalogue. The symbols show the method of BH mass measurement: stellar dynamics (stars), gas dynamics (circles), masers (asterisks). Errors are indicated by error bars. The different colours indicate the Hubble type. The best fit relation is $M_{BH} = 10^{8.12} M_{sun} (\sigma / 200 kms^{-1})^{4.24}$. The NGC 4414 measurement is overplotted with a black point having an upper limit.*

After determining M_{BH} for NGC 4414, it is important to evaluate the measurement in contrast to other galaxy's M_{BH}. A proper comparison is feasible based on the SMBH-host scaling relations which were discussed in chapter 1.3. As both the mass of the BH and the velocity dispersion of the effective radius were determined in this thesis, updating of the $M_{BH} - \sigma$ relation is reasonably straight-forward. Hence, figure 7.3 illustrates how the NIFS measurement in the central region of NGC 4414 affects the galaxy's location in the $M_{BH} - \sigma$ relation.
Figure 7.3 is essentially the same figure as 1.1 where the different galaxy types (spiral, S0 and elliptical galaxies) are colour-coded. The different symbols mark the different methods for estimating the SMBH mass, based on stellar kinematics, gas kinematics and maser dynamics.
The NIFS data provides $\sigma_{e,NGC4414} = 109.5$ km/s which is consistent with earlier measurements being found in HyperLeda. Regarding the mass of the SMBH an upper limit of $M_{BH,NGC4414} = 1.1 \times 10^5 M_{sun}$ was found in the previous section. Both measurements are overplotted in the $M_{BH} - \sigma$ relation as black dot having an upper limit.

Based on the updated $M_{BH} - \sigma$ relation it is evident that the NGC 4414 measurements

do not follow the general trend. Instead, the mass of the SMBH was measured to be significantly smaller than predicted from the scaling relations. Further studies have to be conducted to further constrain the M_{BH} and ascertain the presence of the SMBH. Given that NGC4414 does not have a M_{BH} as predicted from the $M_{BH} - \sigma$ relation suggests that the evolution of NGC4414 is different from other similar galaxies.
Gebhardt et al.(2001) show that BHs do not correlate with the properties of the galaxy's disk. Instead, it appears that the main requirement for the formation of a SMBH is that a galaxy contains some form of central bulge. The central bulge is a tightly packed accumulation of stars located within the center of spiral galaxies. The gravitational field of the bulge is essential to form instabilities to drive the developing SMBH towards the center of the galaxy and grow by accreting matter(chapter 1.3.4). However, latest studies suggest that the formation of SMBHs is independent of the presence of a bulge, as galaxies harbouring SMBHs without an accompanying bulge have been observed recently (McAlpine et al. 2011, Secrest et al. 2013).

However, NGC 4414 is not the only case with a SMBH that is less massive that expected based on the scaling relation. Other galaxies like the spiral galaxies NGC 6503 and NGC 3198 were hypothesised to not contain SMBHs (Ferrarese & Ford 2002).

7.3 Discussion of Accuracy

The carried out method of stellar kinematics to determine the central SMBH's mass is highly dependent of the spatial resolution of the kinematics data. Large uncertainties on the constraints of the measured mass occur based on the inability to resolve the sphere of influence of the BH. When the kinematic data is unable to resolve the sphere of influence of the BH, spurious results can occur.
In chapter 7.1, the M_{BH} of NGC 4414 has been qualified up to the upper limit of around $M_{BH,NGC4414} = 1.1 \times 10^5 M_{sun}$. Combining the M_{BH} with the velocity dispersion at the effective radius $\sigma_{e,NGC4414} = 109.5$ km/s by using $r_{inf} = \frac{G M_{BH}}{\sigma_e^2}$ the effective radius of NGC 4414 has an upper limit of 0.04 pc. As NGC 4414 is located at 19.1 Mpc distance, the sphere of influence has a size of around $5 \times 10^{-4}\,''$ in the sky.
On the other hand, NIFS is able to able to achieve spatially resolved spectroscopy at $0.1''$[11] scales by using AO. Hence, the sphere of influence is significantly smaller than NIFS's resolution and therefore not directly detectable. However, Kormendy & Ho (2013) point out that lower resolution spectroscopy does generally not provide unrealistic M_{BH} measurement, although the error bars grow due to the loss in constraints. This statement is confirmed by the history of M32 SMBH measurements which was discussed in chapter 2.2.2. Within 15 years, the SMBH in M32 was determined several times. Even though the first measurements were conducted with a very poor resolution, the M_{BH} was determined to be relatively close to the present accepted SMBH mass. The poor resolution (and different determination techniques) resulted into an insignificant overestimation of the M_{BH}. Hence, it has to be noted that the inability to properly resolve the sphere of influence leads to larger errors and a potential overestimation of the M_{BH}. Both aspects are negligible for NGC 4414, as this study only provides upper limits.

[11] http://www.gemini.edu/sciops/instruments/nifs/

Chapter 8

Conclusion

8.1 Summary

In this work, I have presented the determination of the M_{BH} of the spiral galaxy NGC 4414, which is located in the local universe, by using the method of stellar kinematics. The main assumption of this method is that the gravitational potential which describes the stellar kinematics is composed of the collective stellar potential and the potential of the SMBH $\Phi_{grav} = L_{star} \times M/L + \Phi_{BH}$. Dark matter and a gas compound contribute only a few percentage (Vallejo et al. 2003) and are thus have been neglected. Hence, the method consists of three major steps: 1)parametrise the surface brightness with Multi Gaussian Expansion models to obtain a stellar mass model, 2)extract the stellar kinematics from integral field spectroscopic data and 3)construct Jeans models based on 1) an 2).

The study used a combination of HST/SDSS images and NIFS integral field spectra. In the first step, the galaxy's surface brightness was parametrised using the MGE modelling method in order to measure the stellar mass fraction of the galaxy. Combined with an M/L, the MGE model could be transformed into a stellar mass model. However, before modelling the surface brightness, a dust correction for galactic extinction based on Scott et al. (2013) & Schlegel et al. (1998) was applied. It turned out that the dust correction did not change the MGE model significantly as the modelling works axialsymmetric on the galaxy. It was also tested if the MGE model would better fit the combination of HST (center) and SDSS (large-scale) images. The combination works slightly better as both the center of the galaxy and the edges of the surface brightness profile can be better reproduced.

In the second step, the central kinematics from NGC 4414 was extracted from the NIFS data. The NIFS data maps the core region of the galaxy. At first, several data sets had to be merged to improve the S/N and then they were transformed into a 3-dimensional datacube (x,y,λ). Although the data has good S/N in the center of the galaxy, it suffers from having a small S/N towards the edge of the field-of-view. From spaxels having an insufficient S/N it is impossible to extract the kinematics. However, by binning different spaxels the signal could be enhanced in such a way that spectra are distinguishable from the background noise. I used the adaptive Voronoi binning method, which bins the spaxels adaptively according to their S/N. No spaxels were binned in the center of the data, while the bins become larger towards the edge of the field-of-view. Then, from the binned datacube, the kinematics were extracted by using the penalized Pixel Fitting (pPXF) method. The kinematics are described by a velocity distribution within one bin which is measured along the line-of-sight (LOSVD). The LOSVD is approximately Gaussian shaped, but can be more accurately described by

additional Gauss-Hermite polynomials. Ppxf convolves a pre-defined stellar template with a corresponding LOSVD and fits it to the spectrum of a bin. By applying pPxf on the entire data cube, kinematic maps for the rotational velocity, velocity dispersion and the Gauss-Hermite polynomials h_3 and h_4 were created. The rotational velocity map indicates a fairly symmetric rotation of the galaxy along the x-axis of the 3.0" x 3.0" NIFS image field. The velocity dispersion map does not show a steep peak in the center which is expected for the presence of a SMBH.
In order to get an idea about the uncertainties of the kinematic maps, Monte Carlo simulations were performed to create replica of the datasets by applying small perturbations related to random noise on the spectra. pPXF was run on the simulations to obtain error maps. Typical errors are 3 km/s, 4 km/s, 0.03, 0.03 for V, σ, h_3 and h_4, respectively.

Both the photometric MGE model and the Kinematic maps were then simultaneously fitted to construct a dynamical Jeans model by using the Jeans Anisotropic MGE (JAM) script. The dynamical model has the following three free parameters: The mass of the BH M_{BH}, the anisotropy parameter β (chapter 6.2) and the mass-to-light ratio M/L. Based on the free parameters, I constructed 90 Jeans models on a $M_{BH} - \beta$ parameter grid. The Jeans models were compared to the observational second $V_{rms} = \sqrt{V^2 + \sigma^2}$ velocity map which was obtained from the kinematic maps and the χ^2, defined as deviation between Jeans model and observation, was calculated. The best model was achieved by minimizing the χ^2 and has the parameters $\beta = 0.27$ and $M_{BH} \leqslant 1.1 \times 10^5 M_{sun}$. Hence, I was unable to constrain the SMBH mass with the used Jeans models and even the presence of a SMBH in the center of NGC 4414 is not evident. Possible causes are suspected to be found in the small size of the SMBH and the inability to properly resolve it, inaccuracy of the M/L and too simple assumptions of the dynamical modelling method. Therefore, further approaches have to be conducted in the future. This includes studies of the M_{BH} with the more complex Schwarzschild method and combination of the NIFS kinematic with large-scale GMOS kinematics which better constrain the M/L.
The determined M_{BH} of NGC 4414 was also compared with other galaxies based on the well-established $M_{BH} - \sigma$ scaling relation. According to this relation, many galaxies show a correlation between their SMBH mass and bulge properties of their host galaxies. However, the determined mass for NGC 4414 lies significantly below the general trendline. This gives evidence that NGC 4414 may have a different evolution history than other similar galaxies.

8.2 Future Prospects

By using the methods of this study, I was unable to constrain the SMBH mass M_{BH} of NGC 4414. Several factors contribute to make the determination of the SMBH mass challenging. Firstly, the M_{BH} is so small (or maybe not present) that its sphere of influence cannot be resolved with the NIFS instrument. The small size can be confirmed by the fact that the velocity dispersion map does not show a rise towards the center of the galaxy as it is expected for the presence of a SMBH. Other factors causing larger uncertainties arise from an inaccuracy in the determination of the M/L and in the simplicity of the dynamical models. At least for the last mentioned factors further investigations can be conducted.
NIFS is not the only instrument which provides kinematics data for NGC 4414. Indeed, kinematics data was taken with the GMOS spectrograph which spans a larger field-of-view of $5.5' \times 5.5'$ and then analysed by Martin Bourne (Bourne 2009). However, due to its even lower spatial resolution, the GMOS data is not able to resolve the SMBH. However, its large-scale spatial coverage provides a crucial constraint on the M/L. As the mass of the BH depends on

the M/L, larger uncertainties in the M/L increase the uncertainties in the mass measurement. Including the GMOS data might halfen the mass uncertainty(Krajnović et al. 2009). Thus, the analysis can be improved further by combining the NIFS and GMOS kinematics for the Schwarzschild models.
Another step would be to construct more complex Schwarzschild's three integral axisymmetric models and compare the results with the ones obtained with JAM. As the Schwarzschild's method is more general and has different modelling assumptions, the obtained upper limits can be better constrained.

Bibliography

Batcheldor, D. & Koekemoer, A.M. 2009, PASP, 121, 1245

Becerra, F. 2013, 'The black hole mass vs bulge velocity dispersion relation', https://www.cfa.harvard.edu/~fbecerra/files/Ay202a_TermPaper.pdf

Begelmann, M.C & Volonteri, M. & Rees, M.J. 2006 , Monthly Notices of the RAS 370, 289

Beifiori, A.& Courteau, S. & Corsini, E.M. et al., 2012, Monthly Notices of the RAS, 419, 2497B

Bender R. & Saglia R. P. & Gerhard O. E., 1994, Monthly Notices of the RAS, 269, 785

Binney, J. & Mamon, G.A., 1982, Monthly Notices of the RAS, 200, 361

Binney, J. & Tremaine, S. 1987, 'Galactic Dynamics', Princeton University Press

Binney, J. & Davies, R.L. & Illingworth, G.D. 1990, The Astrophysical Journal, 361, 78

Binney, J. & Merrifield, M., 1998, 'Galactic Astronomy', Princeton University Press

Blandford, R.D. & McKee, C.F. 1982, The Astrophysical Journal 255, 419

van den Bosch, R.C.E. & de Zeeuw, P.T. 2010, Monthly Notices of the RAS, 401, 1770

Bourne, M. 2009, 'Galaxy kinematics for NGC 4414', http://www.astro.le.ac.uk/~mab83/Martin_Bourne_Site/Reports_&_Presentations_files/NGC4414Report.pdf

Bower, G. & Falcke, H. & Herrnstein, R.M. et al. 2004, Science, 304, 704

Braatz, J.A. & Wilson, A.S. & Henkel, C. 1994, The Astrophysical Journal, 437, L99

Braatz, J.A. & Wilson, A.S. & Henkel, C. 1996, The Astrophysical Journal, 106, 51

Braine,J.& Combes, F. & Van Driel, W. 1993, Astronomy and Astrophysics, 280, 451

Bromm, V. & Larson, R.B. 2004, Annual Review of Astronomy & Astrophysics, 42, 79

Cappellari, M. 2002, Monthly Notices of the RAS, 333, 400 (a)

Cappellari, M. & Verolme, E.K. & Van der Marel, R.P. et al., 2002, Astrophysical Journal, 578, 787 (b)

Cappellari, M. 2002, MGE fit Readme (c)

Cappellari, M. & Copin, Y. 2003, Monthly Notices of the RAS, 342, 345 (a)

Cappellari, M. & Emsellem, E. 2004, The Publications of the Astronomical Society of the Pacific, 116, 138

Cappellari, M. & Bacon, R. 2006, Monthly Notices of the RAS, 266, 1126

Cappellari, M. 2008, Monthly Notices of the RAS, 390, 71

Cappellari, M. & Neumayer, N. & Reunanen, J. 2009, Monthly Notices of the RAS, 394, 660

Carollo, C. M. & Franx, M. & Illingworth, G.D. & Forbes, D.A. 1997, The Astrophysical Journal, 481, 710

Carroll, S.M. 2004, 'Spacetime and Geometry', Addison Wesley

Davies R., 2007, 'AO Assisted Spectroscopy with SINFONI: PSF, Background, and Interpolation', invited contribution to the 2007 ESO Instrument Calibration Workshop

Davis, T.A. & Bureau, M. & Cappellari, M. et al. 2013, Nature, 494, 328

de Grijs, R. 2011, 'An Introduction to Distance Measurement in Astronomy', Wiley

de Vaucouleurs, G. 1948, Annales d'Astrophysique, 11, 247

de Vaucouleurs, G., de Vaucouleurs, A. Corwin, J.R. et al. 1991, in Third reference catalogue of bright galaxies (1991)

Devecchi B. & Volonteri, M. 2009, Astrophysical Journal,694, 302

Doelemann, S. S. & Shen, Z.-Q. & Rogers, A. E. E. et al. 2001, Astronomical Journal, 121, 2610

Emsellem, E. & Monnet, G. & Bacon, R. 1994, Astronomy and Astrophysics, 285, 723

Faber, S.M. & Jackson, R.E. 1976, Astrophysical Journal, 204, 668

Ferrarese, L. 2002, Astrophysical Journal, 578, 90

Ferrarese, L. & Ford, H. 2005, Space Science Reviews, 116, 523

Ferrarese, L. & Merritt, D. 2000, Astrophysical Journal, 470, 444

Freeman, K.C. 1970, Astrophysical Journal 160, 183.

Fruchter, A.S. & Hook, R.N. 1998, PASP, 114, 144

Gebhardt, K. & Bender, R. & Bower, G. et al. 2000, Astrophysical Journal, 539, L13

Gebhardt, K. & Lauer, T.R. & Kormendy, J. et al. 2001, The Astrophysical Journal, 122, 2469

Gebhardt K. & Richstone D. & Tremaine S., et al., 2003, The Astrophysical Journal, 583, 92

Genzel, R. & Eisenhauer, F. & Gillessen, S. 2010, Reviews of Modern Physics, 82, 3121

Gerhard O. E., 1993, Monthly Notices of the RAS, 265, 213

Graham, A. W. & Erwin et al. 2001, Astrophysical Journal, 563, L11

Greenhill, L.J. & Herrnstein, J.R. & Moran, J.M., et al. 1997, The Astrophysical Journal, 486, L15-L18

Greenhill, L.J. & Ellingsen, S.P. & Norris, R.P., et al. 2002, The Astrophysical Journal, 565, 836

G ültekin, K., Richstone, D. O., Gebhardt, K., et al. 2009, The Astrophysical Journal, 698, 198

Hawking, S.W. & Ellis, G.F.R. 1973, 'The large scale structure o space-time', Cambridge University Press

Herrnstein, J.R. & Moran, J.M. et al. 1999, Nature, 400, 539

Herrnstein, J.R. & Moran,J.M. & Greenhill, L.J. et al. 2005, Astrophysical Journal, 629, 719

Ho, L.C. 1999, 'Observational Evidence for the Black Holes in the Universe', Conference held in Calcutta, January 11-17th, 1998, p. 157

Holtzman et al. 1995, PASP, 107, 1065

Hosokawa, T. & Omukai, K. & Yoshida, N. 2011, Science 334, 1250

Hoyle, F. & Fowler, W.A. 1963, Monthly Notices of the RAS, 125, 169

Howley, K. & Guhathakurta, P. & van der Marel, R. 2012, arXiv eprint, 1202, 2897

Jahnke, K. & Macciò, A.V. 2011, The Astrophysical Journal, 734, 92

Jeans, J.H. 1915, Monthly Notices of the RAS, 76, 70

Jeans, J.H. 1922, Monthly Notices of the RAS, 82, 122

Johnson, J.L. & Whalen, D.J. & Fryer, C.L. 2012, Astrophysical Journal, 750, 66

King, I. R. 1966, AJ, 71, 64

King, A. 2003, Astrophysical Journal, 596, L27

Kondratko, P. T., Greenhill, L. J., & Moran, J. M., 2004, Proceedings of IAU Symposium, 2004, 325

Kormendy, J. & Richstone, D. 1995, Annual Review of Astronomy & Astrophysics, 33, 581

Kormendy, J., & Gebhardt, K. 2001, in American Institute of Physics Conference Series, Vol. 586, 20th Texas Symposium on relativistic astrophysics, ed. J. C. Wheeler & H. Martel, 363381

Kormendy, J. & Bender, R. & Cornell, M. E. 2011, Nature, 469, 374

Kormendy, J. & Ho, L.C. 2013, Annual Review of Astronomy & Astrophysics, 51, 511-653

Krajnović, D. & McDermid, R. & Cappellari, M. 2009, Monthly Notices of the RAS, 399, 1839

Krist, J. & Hook, R. 2001, 'The Tiny Tim User's Manual'

Lauer, T. R.& Ajhar, E. A. & Byun, Y.-I 1995, Astrophysical Journal, 110, 2622

Lawson, C. & Hanson, R., 'Solving Least Squares Problems', SIAM, 1995

Magorrian, J., Tremaine, S., Richstone D. et al. 1998, Astronomical Journal, 115, 2285

Maoz, E. 1998, Astrophysical Journal, 494, L181

Marconi, A., & Hunt, L. K. 2003, The Astrophysical Journal, 589, L21

McAlpine, W. & Satyapal, S. & Gliozzi, M. 2011, Astrophysical Journal, 728, 25M

McConnell, N. J. & Ma, C.-P., & Gebhardt, K., et al. 2011, Nature, 480, 215

McConnell, N. J. & Ma, C. 2013, Astrophysical Journal, 764, 184

Menou, K. & Quataert, E. & Narayan, R. 1999, in 'Proc. of the 8th Marcel Grossmann Meeting on General Relativity' (Jerusalem), p.204

Monnet G. & Bacon R. & Emsellem E., 1992, Astronomy & Astrophysics, 253, 366

Müller, A. 2007, 'Experimental Evidence of Black Holes', Proceedings contribution to invited seminar talk given at the School on Particle Physics, Gravity and Cosmology, 2006

Narayan, R. & Mahadevan, R. & Grindlay, J.E. 1998, Astrophysical Journal, 492, 554

Neufeld, D. A. & Maloney, P. R. & Conger, S. 1994, Astrophysical Journal, 436, 127

Michell, J. 1784, Philosophical Transactions of the Royal Society of London, 74, 35

Oliva, E. & Moorwood, A. & Danziger, I. 1990, Astronomy and Astrophysics, 240, 453

Peebles, J. 1972, The Astrophysical Journal, 178, 371

Peng, C.Y. 2007, The Astrophysical Journal, 671, 1098

Peterson, B.M 2001, 'Variability of Active Galactic Nuclei', Advanced Lectures on the Starburst-AGN Connection, Proceedings of a conference held in Tonantzintla, Puebla, Mexico, 26-30 June, 2000, p.3

Peterson, B.M. & Horne, K. 2004, Astronomische Nachrichten, 325, 248

Press, W.H. & Teukolsky, S. A. & Vetterling, W. T. et al. 1992, Numerical Recipes in C, 2nd Edition

Reid, M. J. & Menten, K. M. & Genzel, R. et al. 2003, The Astrophysical Journal, 587, 208

Rhee, M.-H. & Van Albada, T.S. 1996, Astronomy and Astrophysics, 115,407

Richstone D.O., Tremaine S., 1984, ApJ, 286, 27

Salpeter, E.E. 1964, The Astrophysical Journal, 140, 796

Schlegel, D. J.& Finkbeiner, D. P. & Davis, M. 1998, The Astrophysical Journal, 500, 525

Schneider, P. 2008, 'Einführung in die extragalaktische Astronomie und Kosmologie', Korrigierter Nachdruck

Schulze, A. 2011, Dissertation 'Demographics of supermassive black holes '

Schwarzschild, K. 1916, Sitzungsberichte der Königlich Preussischen Akademie der Wissenschaften, 189

Schwarzschild M., 1979, The Astrophysical Journal, 232, 236

Scott, N. & Cappellari, M. & Davies, L., et al. 2013, Monthly Notices of the RAS, 432, 1894

Secrest, N.J & Satyapal, S. & Moran, S.M. et al. 2013, Astrophysical Journal, 777, 139

Sérsic, J.L. 1968, 'Atlas de galaxias australes'

Sparke, L. S. & Gallagher, J. S. 2007, 'Galaxies in the Universe', Cambride University Press

Spitzer, L. 1987, 'Dynamical Evolution of Globular Clusters', Princeton University Press

Statler T., 1995, The Astrophysical Journal, 109, 1371

Sutherland, W., 2012, 'Chapter 2: Stellar Dynamics in Galaxies', The Galaxy, London, Lecture

Thorne, K.S. 1994, 'Black Holes and Time Warps', Norton, W.W. & Company, Inc.

Thornley, M. D. 1996, Astrophysical Journal, 469, 45T

Titarchuk, L. & Zannias, T. 1998, Astrophysical Journal, 493, 863

Tonry, J.L. 1984, The Astrophysical Journal, 283, L27

Tremaine, S., Gebhardt, K., Bender, R., et al. 2002, The Astrophysical Journal, 574, 740

Tremaine, S. 2014, 'The odd couple: quasars and black holes' in "From Atoms to the Stars", a special issue of Daedalus (Fall 2014, vol. 143, no. 4)

Turner, A. & Ferrarese, L. & Saha, A., et al. 1998, Astrophysical Journal, 505, 207T

Vallejo, O. & Braine, J. & Baudry, A. 2002, Astronomy and Astrophysics,

Vallejo, O. & Braine, J. & Baudry, A. 2003, 'The Evolution of Galaxies', Springer Netherlands, pages 421-424

Valluri M. & Ferrarese L. & Merritt D. et al., 2005, The Astrophysical Journal, 628, 137

van den Bosch, R.C.E. & van de Ven, G. & Verolme, E.K., et al. 2008, Monthly Notices of the RAS, 385, 647

van der Marel, R. & Franx, M. 1993, Astrophysical Journal, 407, 525

van der Marel, R. & Evans, N.W. & Rix, H.-W., et al. 1994, Monthly Notices of the RAS, 271, 99

van der Marel, R.P.& Cretton, N. & de Zeeuw, P.T., et al. 1998, ApJ, 493, 613

Volonteri, M. 2012, Science, 337, 544V

Walsh, J. L. & Barth, A. J. & Sarzi, M. 2010, Astrophysical Journal, 721, 762

Winge, C. & Riffel, R. & Storchi-Bergmann, T. 2009, Astrophysical Journal, 185, 186

Zeldovich, Y. B. & Novikov, I. D. 1964, Sov. Phys. Dokl., 158, 811

Accronyms and Abbreviations

AGN: Active Galactic Nucleus

AO: Adaptive Optics

BH: Black Hole

BLR: Broad Line Region

CBE: Collisionless Boltzmann equation

CCD: Charge-Coupled Device (Camera)

DF: Distribution Function

DM: Dark Matter

HST: Hubbles Space Telescope

IDL: Interactive Data Language

IFU: Integral Field Unit

JAM: Jeans Anisotropic MGE

JE: Jeans Equation

LOSVD: Line-Of-Sight Velocity Distribution

MGE: Multi Gaussian Expansion

NLR: Narrow Line Region

pPXF: penalized Pixel-Fitting

PSF: Point Spread Function

RM: Reverberation Mapping

SMBH: SuperMassive Black Hole

WFPC: Wide Field and Planetary Camera

List of Figures

Deutsche Zusammenfassung

In der vorliegenden Arbeit präsentiere ich den Versuch der Massenbestimmung des supermassiven Schwarzen Loches der Spiralgalaxie NGC 4414 mit der Methode der Stellaren Kinematik. Die zentrale Annahme dieser Methode ist, dass das Gravitationspotential, welches die Sternenbewegungen beschreibt, zusammengesetzt ist aus dem gesamten stellaren Potential und dem Schwerefeld des supermassiven Schwarzen Loches (SMBH). Schwarze Materie und zusätzliche Gaskomponenten steuern nur einen geringen prozentualen Anteil bei und können daher vernachlässigt werden. Ausgehend von dieser zentralen Annahme sind drei wesentliche Schritte abzuarbeiten: 1) die Parametrisierung der Oberflächenhelligkeit mit Hilfe einer Multi Gaussian Entwicklung (MGE), um ein stellares Massenmodel zu finden, 2) die Extrahierung der stellaren Kinematik aus integralfeldspektroskopischen Daten und 3) die Erstellung eines Jeans-Models basierend auf 1) und 2).

Die Untersuchung wurde auf Basis von hochaufgelöster NIFS-Integralfeldspektroskopie der zentralen Galaxienregionen und HST-/SDSS-Aufnahmen betrieben. Im ersten Schritt wurde die Oberflächenhelligkeit der Galaxie durch ein MGE-Modell beschrieben, um den stellaren Massenanteil zu erhalten. Kombiniert mit dem zu ermittelnden intrinsischen Masse-Licht-Verhältnis M/L konnte das MGE-Modell in ein stellares Massenmodel gewandelt werden. Vor der Modellierung wurden die SDSS Aufnahmen der Galaxie um galaktische Extinktion durch Staub korrigiert. Die Staubkorrektur veränderte das MGE-Modell jedoch nicht signifikant, da die MGE-Methode axisymmetrisch arbeitet. Außerdem wurde getestet, ob eine Kombination aus hochaufgelöster HST-Aufnahme und groflächiger SDSS-Aufnahme ein besseres MGE-Modell erzeugen würde. Die Untersuchung kam zu dem Zwischenergebnis, dass die Kombination ein besseres Ergebnis lieferte, da sowohl das Galaxienzentrum als auch der Rand des Oberflächenhelligkeitsprofils besser nachgebildet werden konnten.

Im zweiten Schritt wurde die zentrale Sternenkinematik der Galaxie NGC 4414 von den NIFS-Daten abgeleitet. Die NIFS-Daten bilden lediglich die Kernregionen der Galaxie ab. Zunächst mussten mehrere Datensätze kombiniert, um das Signal-Rausch-Verhältnis S/N zu verbessern, und dann in einen 3-dimensionalen Datenkubus (x, y, λ) umgewandelt werden. Problematisch an den Datensätzen war, dass zwar ein gutes S/N im Zentral bereich der Galaxie, aber nur ein geringes S/N in den Randbereichen des Sichtfeldes erreicht wurde. Von Spektren mit ungenügendem S/N ist es unmöglich, die Kinematik abzuleiten. Hilfreich war das 'Binnen' mehrerer Spaxel, um das Signal zu verstärken und die spektralen Merkmale vom Hintergrundrauschen zu trennen. Hierfür benutzte ich die adaptive 'Voronoi-binning'-Methode, die Spaxels entsprechend ihres S/N verbindet. Keine Spaxel wurden im Zentralbereich der Daten zusammengefasst, während die Bins in Richtung des Bildrandes immer größer wurden. Vom gebinnten Datenkubus wurde schlielich die Kinematik mit Hilfe der 'penalized Pixel Fitting (pPXF)'-Methode abstrahiert. Die Kinematik wird durch eine Geschwingigkeitsverteilung der Sterne eines Bins entlang der Sichtlinie (LOSVD)

beschrieben. Die LOSVD ist im Allgemeinen Gauß-förmig, kann jedoch mit zusätzlichen Gauß-Hermite-Polynomen noch präziser beschrieben werden. pPXF faltet eine vorgegebene Überlagerung von Sternenspektrum mit einer entsprechenden LOSVD und passt die gefaltete Funktion an das Spektrum eines Bins an. Durch die Anwendung von pPXF auf den ganzen Datenkubus konnten kinematische Karten von der Rotationsgeschwindigkeit V, der Geschwindigkeitsdispersion σ und der Gauß-Hermite-Polynome erstellt werden. Die Rotationsgeschwindig keitskarte zeigt eine recht symmetrische Rotation entlang der x-Achse des NIFS Bildfeldes. In der Geschwindigkeitsdispersionskarte erkennt man jedoch keine signifikante Erhöhung im Zentrum wie in der Anwesenheit eines SMBH erwartet wird. Um eine Vorstellung der Unsicherheit der kinematischen Karten zu erhalten, wurden Monte-Carlo-Simulationen durchgeführt und Abbilder des Datensatzes durch kleinste zufällige Rauschstö rungen geschaffen. pPXF wurde auf diese Abbilder angewandt und Fehlerkarten erzeugt. Typische Fehler liegen im Bereich 3 km/s, 4 km/s, $0.03, 0.03$ entsprechend für V, σ, h_3, h_4.

Sowohl das photometrische MGE-Modell als auch die kinematischen Karten wurden schließlich simultan gefittet, um dynamische Jeans-Modelle mit dem Jeans Anisotropic MGE (JAM)-Skript zu erstellen. Das dynamische Modell hat drei freie Parameter: Die Masse des SMBH M_{BH}, der sogenannte Anisotropie-Parameter β und der M/L. Bezogen auf diese freien Parameter, konstruierte ich 90 Jeans-Modelle auf einem $M_{BH} - \beta$-Gitter. Die Jeans-Modelle wurden dann mit dem beobachteten zweiten Geschwindigkeitsmoment $V_{rms} = \sqrt{V^2 + \sigma^2}$ verglichen und ein sogenannter χ^2-Wert, der die Abweichung zwischen Jeans-Modell und Beobachtung wiedergibt, berechnet. Das beste Modell ergab sich aus der Minimierung des χ^2-Wertes und hat die Parameter $\beta = 0.27$ und $M_{BH} \leqslant 1.1 \times 10^5 M_\odot$. Folglich war es mir nicht möglich, die SMBH Masse mit Hilfe der Jeans-Modellierung genau einzugrenzen, sodass die Anwesenheit eines SMBH im Kern der Galaxie NGC 4414 weiterhin ungeklärt bleibt. Gründe hierfür liegen unter anderem an der geringen Größe des SMBH und damit der Nichtauflösbarkeit mit NIFS, Ungenauigkeit im M/L und der zu stark vereinfachenden Annahmen des Jeans-Modells. Weitere Methoden müssen in der Zukunft durchgeführt werden, um die Masse näher zu bestimmen.
Ferner wurde die bestimmte M_{BH} mit anderen Galaxienmassen aufgrund der empirischen $M_{BH} - \sigma$-Beziehung verglichen. Entsprechend dieser Beziehung zeigen viele Galaxien eine Korrelation zwischen ihrer SMBH Masse und verschiedenen 'Bulge'-Eigenschaften ihrer Hostgalaxie. Die von mir ermittelte SMBH Masse für NGC 4414 liegt jedoch signifikant unterhalb des generellen Trends. Dies gibt Aufschluss darüber, dass NGC 4414 eine andere Entstehungsgeschichte haben könnte als andere ähnliche Galaxien.

Die gesamte Arbeit basiert auf Skripten, die von Michelle Cappellari geschrieben wurden.

Danksagung

Diese Arbeit wäre nicht ohne meine beiden Betreuer Davor Kranović und Lutz Wisotzki möglich gewesen. Lutz Wisotzki hat mir die Möglichkeit gegeben, meine Abschlussarbeit in der extragalaktischen Astrophysik anzufertig, Davor Kranović hat mir stets mit Rat und Tat zur Seite gestanden. Durch beider Hilfe habe ich das Thema der stellaren Kinematik zur Massenbestimmung schwarzer Löcher kennengelernt und konnte mein Wissen immer weiter vertiefen. Davor Krajnović möchte ich insbesondere danken, dass er auch bei meiner Spontanität doch immer Zeit für mich gefunden hat. Hilfreich waren auch die Diplomanden- und Masterandentreffen, die wir alle zwei Wochen abgehalten haben. Hier konnten wir uns gegenseitig austauschen, die eigenen Themen festigen und weitere Themenfelder kennenlernen. Daher danke ich auch Justus Neumann, Maria Haupt und Josie Kerutt, für interessante Fragen zur Weiterführung meiner Arbeit. Außerdem möchte ich mich bei Christian Herenz bedanken, der mich in Computerfragen unterstützt und mir die Integralfeldspektroskopie sehr gut erklärt hat. Ganz besonders möchte ich mich auch bei dem IT-Bereich des AIP bedanken, sowie bei Karl-Heinz Boehning, der alle Hardware-angelegenheiten für mich geklärt hat.

Des weiteren möchte ich mich gerne bei Thomas Schmidt und Pratham Raj Yoshi bedanken, dass sie meine Arbeit durchgelesen und so viele Englischfehler wie möglich ausgemerzt haben. Durch euch ist meine Arbeit erst so lesbar und verständlich geworden wie sie jetzt ist.

Ein ganz besonderer Dank gilt meiner Familie, die mich während meines gesamten Studiums unterstützt hat. Ohne euch wäre es mir niemals möglich gewesen, meinen Traum zu erfüllen und Physik zu studieren. Meinem Freund möchte ich unglaublich danken für seine Unterstützung, seine ermutigenden und aufbauenden Worte und dass er auch in schweren und stressigen Zeiten immer für mich da war.

Eidesstattliche Erklärung

Hiermit versichere ich, dass ich die vorliegende Diplomarbeit selbstständig und ohne fremde Hilfe verfasst habe. Alle verwendeten Quellen und Materialien sind in der Literaturliste aufgeführt, weitere wurden nicht benutzt. Wortwörtlich und inhaltlich entnommene Stellen sind als solche kenntlich gemacht. Die Diplomarbeit hat keiner anderen Prüfungsbehörde vorgelegen.

Potsdam, den

Sabine Thater